EXTERNAL WAVELENGTH STABILIZATION OF GRATING COUPLED SURFACE EMITTING LASERS AND APPLICATIONS

by

Yigit Ozan Yilmaz

A dissertation submitted to the faculty of
The University of North Carolina at Charlotte
In partial fulfillment of the requirements
for the degree of Doctor of Philosophy in
Optical Science and Engineering

Charlotte

2012

Approved by:

_____
Dr. Eric G. Johnson

_____
Dr. Faramarz Farahi

_____
Dr. Yong Zhang

_____
Dr. Tsing-Hua Her

_____
Dr. Oleg V. Smolski

ABSTRACT

YIGIT OZAN YILMAZ. External wavelength stabilization of grating coupled surface emitting lasers and applications. (Under the direction of Dr. ERIC G. JOHNSON)

In this research, external wavelength stabilization of broad area grating coupled surface emitting lasers (GCSELs) by an external feedback grating are investigated. One-dimensional (1D) and two-dimensional (2D) external cavity GCSEL arrays were fabricated and tested. This dual grating external cavity surface emitting laser (DGECSEL) is combination of a GCSEL device and an external grating operating under Littrow condition. The gratings were fabricated on silicon wafers using projection lithography, which enabled the positioning of different period gratings on the silicon wafer to match with the GCSEL device spacing on the laser bar.

The monolithic approach for wavelength stabilization of GCSELs with internal dual grating reflectors (DGR) are also investigated for multi-wavelength 1-D vertical stack array fabrication.

Furthermore, blue light generation using GCSEL based devices were experimentally investigated. Single wavelength and multi-wavelength blue light generation efficacy is measured using single DGECSEL and GCSEL/ DGR devices as well as 1-D DGECSEL and 1-D vertically stacked GCSEL/DGR devices.

DEDICATION

To my family,

ACKNOWLEDGEMENTS

I would like to thank my advisor, Dr. Eric G. Johnson for giving me the opportunity to work on this and several different projects, for his guidance, and patience throughout my Ph.D. I would like to thank him for his never ending support, optimism, and his hard work for providing funding and excellent facilities without which this work would not have been possible. I am extremely proud to have studied under him. I would also like thank Dr. Oleg V. Smolski for his massive contributions into this work. It was a pleasure to work with him. I also like to thank the committee members, Dr. Faramarz Farahi, Dr. Yong Zhang, and Dr. Tsing-Hua Her for their useful comments and suggestions.

I would like to thank all Microphotonics Laboratory members and alumni; it was a true pleasure to be part of these great minds. I would like to thank Dr. Pradeep Srinivasan for teaching me the fabrication techniques in the cleanroom and his support throughout this work. I would like to thank Viktor Smolski, for his contributions during the laser diode fabrication. I also like to thank Dr. Menelaos Poutous for his time and sharing his expertise in microfabrication.

I would like to thank my parents and my sister for their endless support and their love.

This work was supported by the Office of Naval Research under Grant ONR N00014-09-1-0498.

TABLE OF CONTENTS

CHAPTER 1: INTRODUCTION

The first stimulated emission, from semiconductor material was demonstrated by research groups at General Electric and IBM T.J. Watson research centers [1,2] just after the successful operation of a solid-state ruby laser by Maiman [3]. Since then with the advancement of the material growth and fabrication technologies, semiconductor lasers found numerous applications in: telecommunications, industrial material processing, pumping of solid-state lasers for high power applications, various measuring instruments such as range finding, printing industry, CD, DVD, Blue-ray technologies and medical applications. Various types of semiconductor lasers have been specifically developed for these applications.

In this dissertation, we explore a semiconductor optical device configuration based on non-resonant diffraction grating coupler. These devices are coupled with monolithic and external wavelength selection elements to form the resonant cavity lasing at ~980nm. Different configurations of these external and monolithic lasers in one-dimensional (1-D) and two-dimensional (2-D) array were fabricated and experimentally studied under quasi- continuous wave (QCW) and pulsed pump current conditions. The lasers are also utilized in blue light generation through nonlinear second harmonic generation (SHG). Diffractive micro-optical beam shaping optics were designed and fabricated for a compact multi-wavelength high peak power blue light source.

In this chapter basic principles and characteristics of semiconductor lasers will be covered first. Then different emission and wavelength stabilization configurations will be

overviewed with main focus on the surface-emitting and external cavity lasers. Lastly, laser sources emitting at blue wavelength region will be reviewed since the laser devices fabricated in this thesis were utilized in blue light generation.

1.1 Basic Principles of Semiconductor Lasers

The first semiconductor laser is a forward-biased GaAs p-n junction [1]. This type of laser is called homostructure lasers. By introducing one semiconductor layer between the two cladding layers of another semiconductor with a relatively wider energy band gap the device performance was improved multiple orders of magnitude compared to homostructure lasers [4, 5]. This heterostructure type lasers are classified into single- or double-heterostructure lasers depending on whether the active region is surrounded by one or two cladding layers. Figure 1.1 shows the structure of a double-heterostructure semiconductor laser.

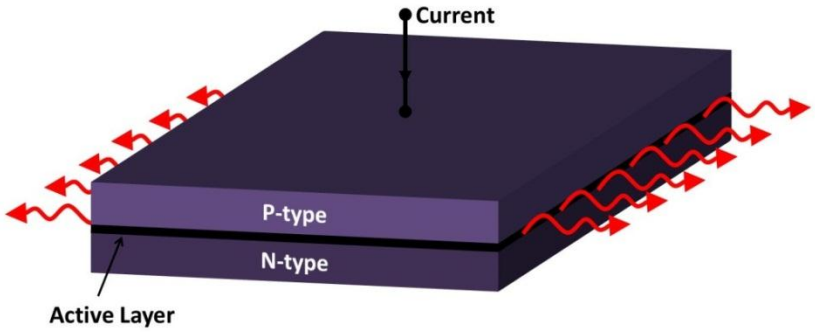

Figure 1:1 Double-heterostructure laser. The semiconductor material in the active region has slightly lower band gap energy than the surrounding cladding layers.

The band gap difference between the active layer and the cladding layer confine electrons and holes to the active layer, for more effective recombination. Also the

cladding layers with high band gap energy have lower refractive index compared to the active region. This refractive index difference confines the optical mode very close to the active layer; this in return introduces more optical gain, with the reduction of the internal losses [8,9]. The schematic of the charge carrier and the optical mode confinement in the active region is shown in Figure 1.2

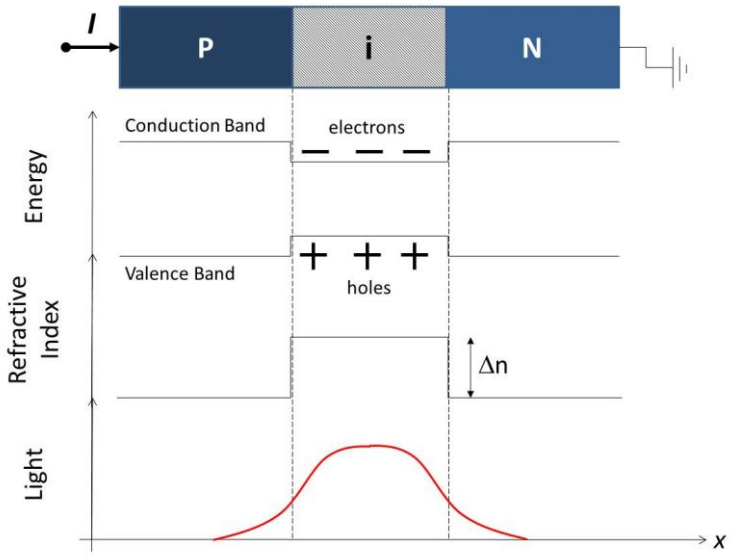

Figure 1:2 Schematic illustration of the double heterostructure carrier and optical mode confinement. From top to bottom : material structure , energy diagram, refractive index profile and the optical mode profile.

The carrier-confinement in the double-heterostructure is very important in semiconductor diode lasers. The transverse carrier and photon confinement for today's semiconductor lasers are more complex. Thinner quantum-well carrier-confining active region and surrounding intermediate band gap separate confinement region (SCH) to confine the optical mode [8,9]. The cladding materials can also be progressively doped so that the band gap of the cladding is reduced gradually to meet the band gap of the smaller band gap material. This type of SCHs is called Graded Index SCH (GRINSCH). Figure

1.3 shows the transverse band structure for abrupt standard SCH and GRINSCH. The devices in this thesis are based on GRINSCH design.

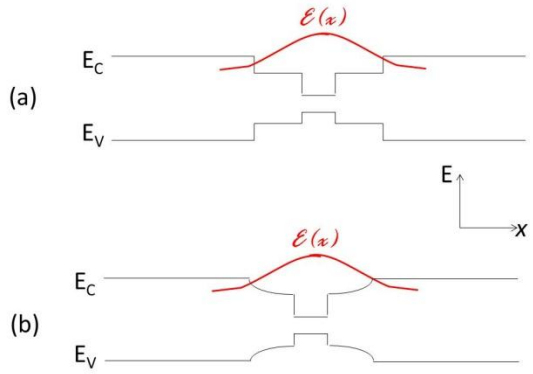

Figure 1:3 Band structures for (a) separate-confinement heterostructure (SCH); (b) graded-index SCH (GRINSCH). The confined optical field is also shown in red line.

The choice of the material for heterostructure lasers is extremely critical for efficient laser operation. The fundamental requirement for the neighboring materials forming the heterojunction interface is that they should have the same crystal structure and typically have a lattice constant match better than 0.1%. Recent advances in the epitaxial material growth techniques permits up to few percent lattice mismatch, lasers made from are called strained-layer lasers and have a superior performance. Elements from third and fifth column of the periodic tables are the choice of materials for lasers emitting from 700nm to 1600nm wavelength range[6]. Most of the III-V materials used for semiconductor lasers have a direct band gap energy, in which the minimum and the maximum of the conduction and valence bands, respectively, are aligned in the same wave number. For lasers emitting in the blue region of the wavelength II-VI materials are used.

Most efficient 980-nm lasers are based on the ternary AlGaAs and InGaAs alloys[7]. The excellent index contrast, lattice match, and thermal conductivity of AlGaAs is very important in optimizing the laser structure, while single InGaAs quantum well active region produces enough gain and good carrier confinement leading to low-threshold current and high quantum efficiency. The table below shows the layers of an example of GRINSCH type gain medium with single InGaAs quantum well (SQW), which is also the laser gain medium design used in this research.

Table 0-1 GRINSCH-SQW well structure made from AlGaAs/InGaAs

Material	Description	~Thickness(nm)
GaAs	p-contact	200
$Al_yGa_{1-y}As$	p- Cladding	750
InGaP	etch stop	20
$Al_yGa_{1-y}As$	p- Cladding	260
$Al_yGa_{1-y}As \rightarrow Al_xGa_{1-x}As$ (graded)	Waveguide	200
GaAs	Buffer Layer	10
$In_{1-x}Ga_xAs$	QW	8
GaAs	Buffer Layer	10
$Al_yGa_{1-y}As \rightarrow Al_xGa_{1-x}As$ (graded)	Waveguide	200
$Al_yGa_{1-y}As$	n- Cladding	1200
GaAs	Buffer Layer	200
n-GaAs	Substrate	

When the current flowing through a semiconductor laser is increased, electrons and holes are injected into the thin active region, where they recombine through radiative or nonradiative mechanisms. During the radiative recombination the energy released by the electron hole is a photon whose frequency (or wavelength) is $\nu = E_g / h = c / \lambda$, where ν, E_g, h, c, and λ are frequency, bandgap energy, Planck's constant, speed of light

in vacuum, and wavelength , respectively. The radiative mechanisms are spontaneous and stimulated emission. During the spontaneous emission there is no phase relationship between the emitted photons. Stimulated emission is initiated by an existing photon, and the emitted photon has the same direction and wavelength with the initial stimulating photon. For nonradiative recombination processes charge carriers recombine without releasing photons. Instead a phonon is released. This unwanted process lowers the light generation efficiency of the lasers[8,9].

For a semiconductor laser to emit coherent light, the injected current has to reach a certain critical value. Stimulated emission has to compete against the absorption processes during which an electron-hole pair is generated. Since the electron population in the valence band generally far exceeds that of the conduction band, absorption dominates. At a certain value of external current, a sufficient number of electrons are present in the conduction band to make the semiconductor optically transparent. With a further increase in the current, the active region of the semiconductor laser exhibits optical gain and can amplify the electromagnetic radiation passing through it. Spontaneously emitted photons serve as the noise input for the amplification process [8,9].

However, optical gain alone is not enough to operate a laser. The other necessary ingredient is optical feedback[8,9]. In semiconductor lasers it is provided by the cleaved facets that form an FP cavity. The role of the FP cavity is twofold. First, it provides a direction selectivity for the process of stimulated emission, since only photons traveling along its axis are reflected back and forth. Second, it provides a wavelength selectivity

since the feedback is strongest for wavelengths corresponding to the longitudinal modes of the FP cavity [8,9].

Because of the optical feedback, the number of photons traveling perpendicular to the facets increases when the current is large enough to satisfy the condition of the net stimulated emission. However, some photons are lost through the partially transmitting facets and some get scattered or absorbed inside the cavity. If the loss exceeds the gain, stimulated emission cannot sustain a steady supply of photons. This is precisely what happens below threshold, when the laser output consists of mainly spontaneously emitted photons. At threshold, gain equals loss and stimulated emission begins to dominate. In the above threshold regime, laser output increases almost linearly with the current. Almost all electrons and holes injected into the active region now recombine through stimulated emission [8,9].

Threshold condition for a specific type of diode laser depends on various internal and external parameters. To understand the threshold conditions for a laser within a reasonable accuracy is essential. Even though the lasing modes are not plane waves, we can approximate the optical field as

$$E = \vec{x}E_0 e^{i\tilde{\beta}z} \tag{1.1}$$

where the complex propagation constant is defined as

$$\tilde{\beta} = \mu k_0 + i\alpha/2 \tag{1.2}$$

where μ is the refractive index of the medium, and α is the power-absorption coefficient. The net absorption coefficient can be written as [8,9] :

$$\alpha = -\Gamma g + \alpha_{int} \tag{1.3}$$

In the above equation Γ is known as the confinement factor of the optical mode inside the active region and α_{int} is the total internal losses inside the cavity. For a given cavity the oscillating field needs to replicate itself after each round-trip. The equation for a simple cavity as shown in Figure 1.4 can be written as

$$\sqrt{R_1 R_2} e^{-\alpha_p L_{p1}} e^{(\Gamma g_{th} L_a - \alpha_a L_a)} e^{-\alpha_p L_{p2}} = 1 \qquad (1.4)$$

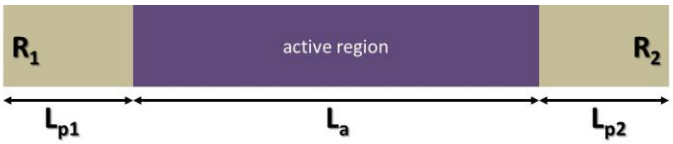

Figure 1:4Schematic illustration of a simple cavity with passive regions

In these equations losses are lumped into the mirror reflectivities. From the above equation the threshold gain can be written as

$$g_{th} = \Gamma^{-1}\left(\alpha_a + \frac{1}{L_a} ln\left(\frac{1}{\sqrt{R_1 R_2}}\right)\right) \qquad (1.5)$$

In the case of an external cavity with a strong external dispersive feedback element,see Figure 1.5, where $R_3 > R_2$, the cavity can be simplified as a coupled-cavity configuration by replacing the diode laser output facet reflectivity r_2 by a complex-valued effective amplitude reflection coefficient r_{eff}, which takes into accounts of both r_2 and $r_3(\lambda)$ [10]. This effective amplitude reflection coefficient $r_{eff}(\lambda)$ can be written as

$$r_{eff}(\lambda) = \frac{r_2 + r_3(\lambda) e^{-i2\pi(\frac{c}{\lambda})\tau_e}}{1 + r_2 r_3(\lambda) e^{-i2\pi(\frac{c}{\lambda})\tau_e}} \qquad (1.6)$$

Figure 1:5 Schematic illustration of external cavity with a external dispersive feedback element. The reflectivity of the filter is peaked at a specific wavelength.

where τ_e is the round trip time of photons inside the external cavity. Again in the above equations losses occuring inside the external cavity are assumed to be lumped in r_3. The threshold gain condition can be found using the similar steps as in the simple cavity.

$$\sqrt{R_1 R_{eff}(\lambda)}e^{-\alpha_p L_{p1}}e^{(\Gamma g_{th}L_a-\alpha_a L_a)}e^{-\alpha_p L_{p2}} = 1 \qquad (1.7)$$

rearranging this equation for g_{th}, and putting all the loss parameters into single parameter α_{int} we get

$$g_{th} = \Gamma^{-1}\left(\alpha_{int} + \frac{1}{L}\ln\left(\frac{1}{\sqrt{R_1 R_{eff}(\lambda)}}\right)\right) \qquad (1.8)$$

where L is the total length of the cavity.

The threshold current density J_{th} can then be written as [11]

$$J_{th} = e^{\left(\frac{g_{th}}{g_0}\right)}(J_{tr} + J_s) - J_s \qquad (1.9)$$

where g_0, J_{tr}, and J_s are net gain, transparency current density, and current density offset ,respectively. Without further going into detail using the well-known equations [12] the optical power exiting the device can be approximated by

$$P = \eta_i \frac{\frac{1}{L}\ln\left(\frac{1}{\sqrt{R_1 R_{eff}(\lambda)}}\right).(I-I_{th})}{\left(\alpha_{int}+\frac{1}{L}\ln\left(\frac{1}{\sqrt{R_1 R_{eff}(\lambda)}}\right)\right)}\frac{h\nu}{q} \qquad (1.10)$$

The change rate of the power with applied bias current is called the slope efficiency, which is

$$\frac{dP}{dI} = \eta_i \frac{\frac{1}{L}\ln\left(\frac{1}{\sqrt{R_1 R_{eff}(\lambda)}}\right)}{\left(\alpha_{int}+\frac{1}{L}\ln\left(\frac{1}{\sqrt{R_1 R_{eff}(\lambda)}}\right)\right)} \frac{h\upsilon}{q} \qquad (1.11)$$

then the differential quantum efficiency , η_d is

$$\eta_d = \eta_i \frac{\frac{1}{L}\ln\left(\frac{1}{\sqrt{R_1 R_{eff}(\lambda)}}\right)}{\left(\alpha_{int}+\frac{1}{L}\ln\left(\frac{1}{\sqrt{R_1 R_{eff}(\lambda)}}\right)\right)} \qquad (1.12)$$

1.2 Grating Coupled Surface Emitting Lasers (GCSELs)

There are two main emission configurations for semiconductor lasers: edge-emitting and surface-emitting configuration. In edge-emitting laser structures, shown in Figure 1.6a-c, the emission of the lasing radiation is parallel to the plane of the active layer. In Figure 1.6a, basic Fabry-Perot type cavity is shown. In this type of cavity the facets of the chip form the two mirrors and provide the feedback. The mirrors are broadband and either the laser functions at multiple longitudinal modes simultaneously or jump between longitudinal modes above threshold. To overcome this longitudinal mode hoping problem and stabilize the emission wavelength, the broadband mirrors can be replaced by distributed Bragg reflector (DBR) type mirrors on both sides of the cavity, see Figure 1.6b. The DBR style mirrors are usually formed along the waveguide by periodically altering the waveguide structure forming a grating section [13,14]. By

changing the depth, length and size of the gratings the reflectivity can be altered. The period of the gratings define the wavelength of emission. Another approach is to have a design where the active region of the device is periodically structured as a Bragg grating (see Figure 1.6c). The structure builds a one dimensional interference grating (Bragg scattering) and the grating provides optical feedback for the laser. This design is called distributed feedback (DFB) style laser and are have a more stable single-mode lasing compared to traditional DBR type lasers[15].

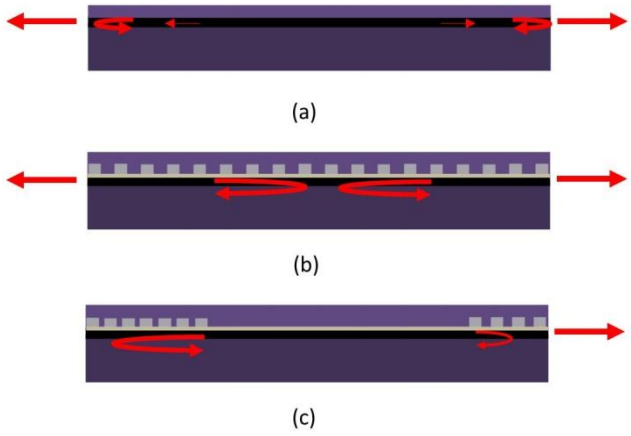

Figure 1:6 Schematics of edge-emitting semiconductor lasers (a) Fabry-Perot resonator, (b) Distributed feedback resonator , and (c) Distributed Bragg Reflector resonator

Surface emitting lasers, shown in Figure 1.7 and Figure 1.8 are distinguished from edge emitting lasers by emission of light normal to the substrate plane. This type surface emission configuration provides wafer-level testing without any cleaving and dicing, as well as higher output powers with the possibility of increased emission area. Another advantage of the surface emitting configuration is the scalability, 1D and 2D laser arrays can be easily fabricated in this surface emitting laser geometry.

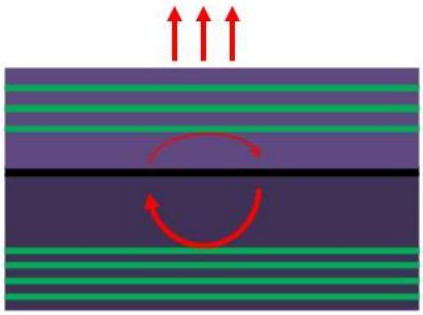

Figure 1:7 Vertical cavity surface emitting laser (VCSEL) , with bottom and top bragg reflector mirrors

The VCSEL design is unique in a way that the Bragg reflectors are formed during the material growth from top to bottom. VCSELs traditionally have circular apertures and emit in the fundamental mode which eases the coupling into single-mode fiber optics which is a great advantage over edge emitting lasers which usually have an elliptical output beam[16,17].

Another surface emitting configuration type is so called grating coupled surface emitting lasers (GCSELs). These types of lasers have grating out-couplers on each end of the cavity. The gratings are fabricated close proximity to the active region and to perturb the waveguide structure to couple out the light into a radiating mode. There are several different GCSEL configurations depending on the periodicity of the out-coupler gratings [18,19,20]. The gratings can be fabricated in 2^{nd} order Bragg condition to provide both wavelength stabilization and surface emission (see Figure 1.8a).

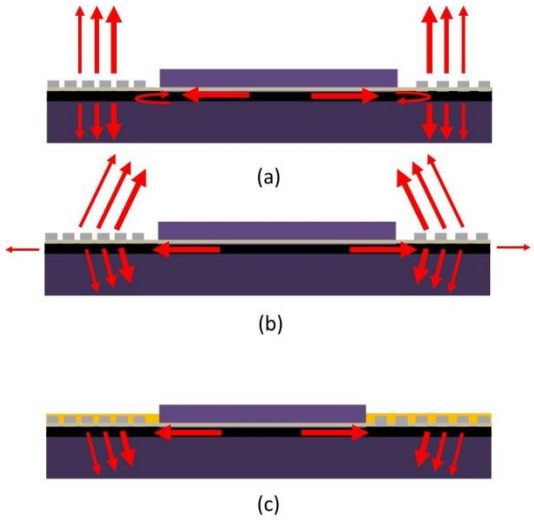

Figure 1:8 Grating coupled surface emitting laser with different emission configurations (a) gratings detuned from the 2nd order Bragg condition ,(b) gratings operaring at the 2nd order Bragg condition, and (c) gratings detuned from the 2nd order Bragg condition wit

In this configuration the device emits both into the substrate and into the air. The gratings can be detuned from the 2nd order Bragg condition in order to suppress the reflectivity back into the cavity and all the light will couple out (see Figure 1.8b) In both configurations the light is emitted from both directions. To eliminate this problem and enhance the directionality of the devices, several approaches have been proposed[21,22]. One of the approaches is to fabricate a high-reflection coating on top of the grating to enhance directionality into the n-substrate [23] as shown in Figure 1.8c.

As stated previously, the wavelengths stabilization of GCSEL type devices can be done by using 2nd order Bragg reflector type gratings. Another approach that was developed in Micro-Photonics Laboratory is based on an integrated wavelength stabilization scheme named the dual grating reflector (DGR) [24]. The DGR consisting of a grating coupler detuned from the Bragg condition on the p-side of the device combined

with a feedback grating operating in the Littrow condition on the n-side surface of the semiconductor laser, see Figure 1.9. This approach is a fully integrated wavelength stabilization technology that forms integrated cavity outside of the active section of the semiconductor laser. The DGR p-side grating coupler period is chose small enough to enable the first diffraction order to exist in the substrate only. This enhances the directionality of grating coupler and eliminates the need of a high-reflection coating. The light incident on the grating coupler is diffracted into the substrate and propagates to the n-side feedback grating. This n-side grating serves to diffract the angularly dispersed light back into the substrate, but for a specific wavelength, that is defined by the Littrow grating period. The light will retro reflects back into the substrate to the p-side grating coupler. The p-side grating coupler couples the light back into the active region.

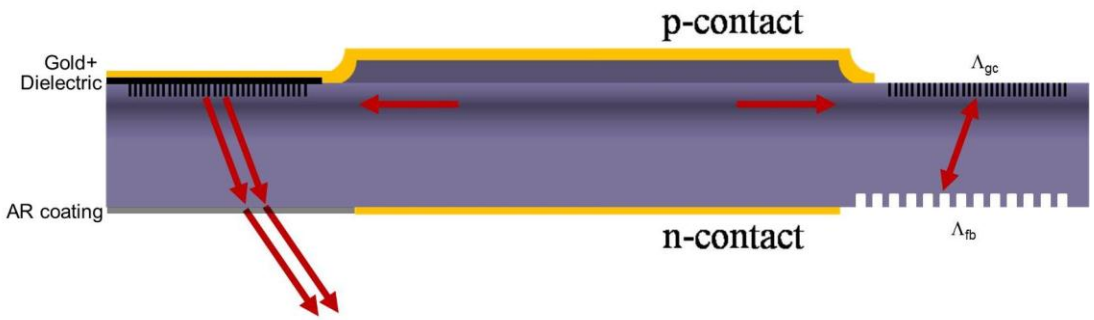

Figure 1:9 Schematic of GCSEL-DGR device

A mathematical expression can be derived for the stabilization wavelength using grating equations. The light incident on first-order grating coupler , with a period of Λ_{gc} will be diffracted at an angle θ into the substrate of refractive index n_s. Given the incident angleϕ, and the effective index of the grating coupler region, n_{eff}, the expression takes the form [18]

$$n_s^2 sin^2\theta = n_{eff}^2 + \frac{\lambda^2}{\Lambda_{gc}^2} - 2n_{eff}\frac{\lambda}{\Lambda_{gc}} cos\phi \quad (1.13)$$

Assuming $\phi = 90^{\circ}$, normal incidence, the grating equation becomes

$$n_s sin\theta = \frac{\lambda}{\Lambda_{gc}} - n_{eff} \quad (1.14)$$

The equation for the feedback grating operating in the Littrow condition can be derived in a similar fashion

$$(n_s sin\theta + n_s sin\theta_t) cos\phi_2 = \frac{\lambda}{\Lambda_{fb}} \quad (1.15)$$

Assuming that $\phi_2 = 0^{\circ}$ and the Littrow condition $\theta = \theta_t$, the equation becomes

$$n_s sin\theta = \frac{\lambda}{2\Lambda_{fb}} \quad (1.16)$$

Plugging the equation Eq. 1.14 into Eq. 1.16 the expression for the stabilization wavelength can be found as

$$\lambda_{sw} = \frac{2\Lambda_{gc}\Lambda_{fb}}{2\Lambda_{fb} - \Lambda_{gc}} n_{eff} \quad (1.17)$$

1.3 External Cavity Semiconductor Lasers

An alternative to monolithic semiconductor diode laser is external cavity diode laser systems. The semiconductor lasers with monolithic wavelength stabilization schemes uses limited portion of the gain spectrum, since the wavelength tuning is very limited after fabrication. The external cavity semiconductor lasers have this flexibility since the wavelength stabilization is done outside the diode. The external cavity diode laser systems primarily consists of a semiconductor diode laser with or without

antireflection coating on one or two facets, collimator for coupling the output of the diode laser, and an external mode-selection filter. Depending on the length of the external cavity, feedback strength, optical power and diode laser parameters the characteristics of the external cavity diode laser system can be varied. Figure 1.10 shows schematic of a very basic external cavity diode laser system[24].

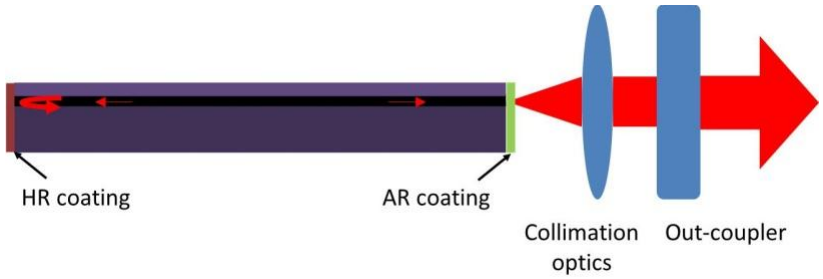

Figure 1:10 Schematics of a simple external cavity diode laser system with out-coupler mirror

The other typical external cavity configurations are Littman-Metcalf and Littrow cavity configurations[25,26], see Figure 1.11. These types of external cavity configurations have broad wavelength tunability. Although they are are widely used, the size of the cavity and scalability is an important bottleneck for these type of external cavity configurations. Several research groups proposed various external cavity configurations to minize the cavity size. One of the external cavity types that attracted quite an attention is the so called Novalux Extended Cavity Surface Emitting Laser (NECSEL). The device is an electrically pumped gallium indium arsenide (GaInAs) surface-emitting semiconductor lasers with extended cavities to control both wavelength and optical mode [27] .

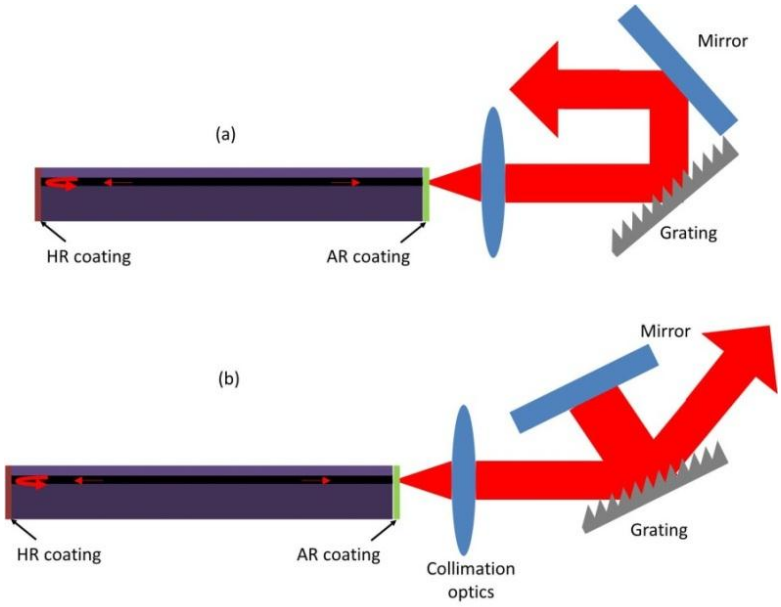

Figure1:11 External cavity laser on (a) Littrow configuration , and (b) Littman-Metcalf configuration

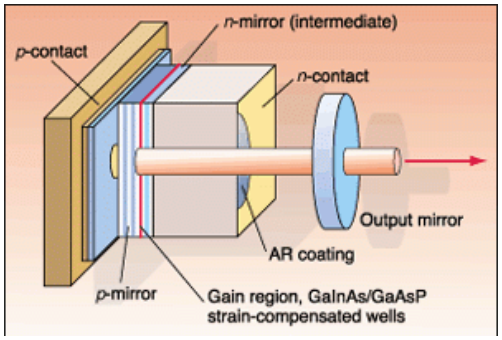

Figure 1:12 Schematics of NECSEL cavity

A key performance feature of the NECSEL is the ability to provide output powers on the order of a watt in single-mode operation and several watts multimode, with beam diameters on the order of hundreds of microns, an order-of-magnitude larger than traditional VCSEL designs [27,28]

These types of tunable cavities are extremely useful for certain applications, an alternative way to cover the gain spectrum is to use Laser arrays, where each laser in the array operates at a particular wavelength.These arrays may incorporate a combiner element, which makes it possible to couple the output to a single fiber. If each laser in the array can be tuned by an amount exceeding achieved. Development of high power light sources based on one- and two-dimensional (2D) laser diode arrays are still in strong demand for efficient pumping of solid-state and fiber lasers. There has been significant efforts in designing novel 2D laser diode arrays such as stair-step stacked multiple single emitters [29] and surface emitters with TIR beam deflectors [30]. One disadvantage of the 2D stacks based on edge-emitter devices is the complex alignment of the collimation optics in the fast- axis; however, vertical cavity surface emitting (VCSEL) 2D arrays [31]offer an attractive alternative to traditional laser diode stacks by providing high output power density and simplified integration with external optical components. Although VCSELs provide numerous advantages, their power conversion efficiency is relatively low when compared to edge emitters [32]. Grating coupled surface emitting lasers (GCSELs) with broad stripes have a large emitting area, competitive conversion efficiencies, and scalable for 2D array configurations

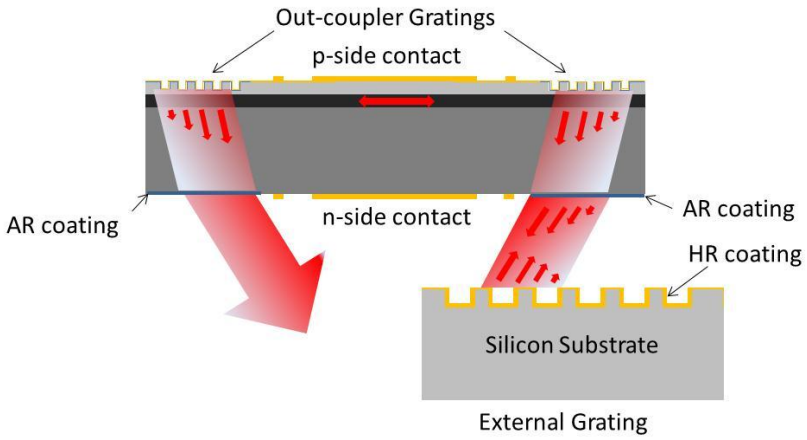

Figure 1:13 Schematics of dual grating external cavity surface emitting laser (DGECSEL) configuration

Similar mathematical expression can be derived for the stabilization wavelength using grating equations for the DGECSEL configuration.

$$\lambda_{sw} = \frac{2\Lambda_{out}\Lambda_{fb}}{2\Lambda_{fb}-\Lambda_{out}} n_{eff} \qquad (1.18)$$

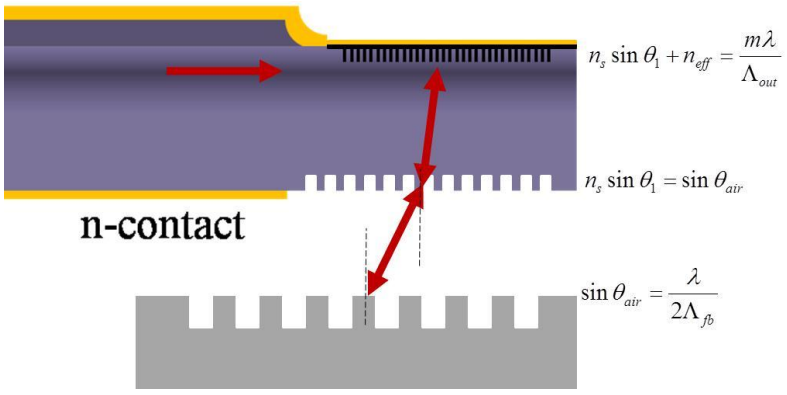

Figure 1:14 Schematics of the external cavity side of the GECSEL device

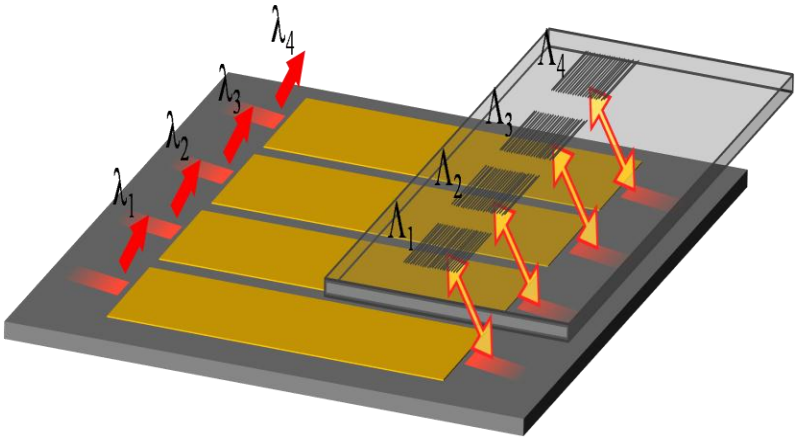

Figure 1:15 Schematics of a multi-wavelength DGECSEL array

1.4 Blue light sources based on nonlinear frequency doubling of semiconductor diode lasers

Laser sources in the blue region are desirable for applications such as color display, optical disk storage, under water optical signal transmission and etc. Recent advances in the design, growth and fabrication of wide band-gap semiconductors led to the realization of compact laser diodes covering the part of the UV spectral region and part of the blue spectral region [33]. Although these laser diodes have relatively high average output power, they have limited spectral range and possess poor spectral quality with multiple lasing lines in the output spectrum. Another alternative for the generation of blue wavelengths is nonlinear conversion of near-infrared (IR) laser diodes.

The nonlinear frequency conversion process is called second harmonic generation (SHG). In SHG a single IR laser with frequency ω is passed through a nonlinear crystal and light emerges with twice the energy, and therefore twice the frequency 2ω and half the wavelength of the initial photons. These "second order" nonlinear effects are

relatively weak but still can be used to generate usable levels of power for certain applications.

In a nonlinear material the relationship between the generated polarization and the applied electric field is nonlinear. The polarization response to an applied sinusoidal filed is not a pure sinusoid. This distorted generated polarization signal have frequency components other than the applied electric field frequency. The mathematical relationship between the polarization *P(t)* and the applied electric field $E_a(t)$ is given by power series expansion as [34]

$$P(t) = \epsilon_0\chi^{(1)}E_a(t) + \epsilon_0\chi^{(2)}[E_a(t)]^2 + \epsilon_0\chi^{(3)}[E_a(t)]^3 + \cdots \qquad (1.19)$$

The second-order term with the squared of the applied electric field gives rise to nonlinear effects. These effects are SHG, sum frequency generation, difference frequency generation, parametric fluorescence, and optical rectification. Figure 1.16 shows the relation between the applied electric field and the induced polarization.

The $\chi^{(2)}$ nonlinear susceptibility term is a tensor, and it is a function of frequency. In technical literature nonlinear coefficient "d" is used rather than $\chi^{(2)}$. The d tensor is 3 by 6 matrix, and components of the this tensor have different values for different nonlinear crystal in three axis [35].

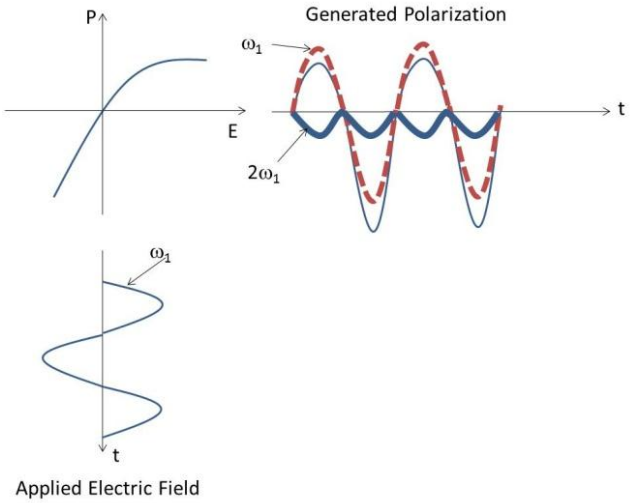

Figure 1:16 Nonlinear medium in which the induced polarization is a nonlinear function of the applied electric field

The second harmonic light that is generated can be calculated using the Maxwell's equations. When the applied monochromatic light wave field to the nonlinear material is

$$E_a(z,t) = A_1 \cos(\omega_1 t - k_1 z) \qquad \text{Eq. 1.20}$$

$$P(z,t) = \epsilon_0 \chi^{(1)} A_1 \cos(\omega_1 t - k_1 z) + \frac{\epsilon_0 \chi^{(2)}}{2} {A_1}^2 [1 + \cos(2\omega_1 t - 2k_1 z) + \cdots \qquad \text{Eq. 1.21}$$

taking the Fourier transform of Equation 1.21 and focusing on the second harmonic term

$$\tilde{P}_{NL}^{(2\omega_1)}(z) = 2\epsilon_0 d(2\omega_1) \tilde{E}_1^{(\omega_1)^2} \qquad \text{Eq. 1.22}$$

using the slowly varying envelope approximation the wave equation at 2ω can be written as

$$\frac{\partial \tilde{E}(2\omega_1)}{\partial z} = -\frac{i\omega_1}{n_{2\omega_1} c} d\tilde{E}^2(\omega_1) e^{i\Delta k z} \qquad \text{Eq. 1.23}$$

where

$$\Delta k = k(2\omega_1) - 2k(\omega_1) \qquad \text{Eq. 1.24}$$

which can be written as

$$\Delta k = \frac{2\pi}{\lambda}\left(\frac{n_{\omega_1} - n_{2\omega_1}}{n_{\omega_1} n_{2\omega_1}}\right) \qquad \text{Eq. 1.25}$$

for low conversion efficiencies $\tilde{E}(\omega_1)$ >> $\tilde{E}(2\omega_1)$, the generated second harmonic field $\tilde{E}(2\omega_1)$ after a distance of *l* inside the nonlinear crystal is

$$\tilde{E}(2\omega_1, l) = \frac{i\omega_1}{n_{2\omega_1} c} d\tilde{E}^2(\omega_1) \int_0^l e^{i\Delta k z}\, dz \qquad \text{Eq. 1.26}$$

the field intensity $I(2\omega_1, l)$ is then

$$I(2\omega_1, l) = \frac{2{\omega_1}^2 d^2 l^2}{n_{2\omega_1} n_{\omega_1} c^3 \epsilon_0}\left[\frac{\sin\left(\frac{\Delta k l}{2}\right)}{\frac{\Delta k l}{2}}\right]^2 I^2(\omega) \qquad \text{Eq. 1.27}$$

The Δk term determines the magnitude of the intensity and intensity is maximized when $\Delta k = 0$. From equation x.x we see that, in order for this phase matching condition to hold n_{ω_1} must be equal to $n_{2\omega_1}$. This is very important for efficient second harmonic generation. Satisfying $n_{\omega_1} = n_{2\omega_1}$ is not possible since the nonlinear optical materials have normal dispersion meaning $n_{2\omega_1} > n_{\omega_1}$. To overcome this problem the most popular approaches are birefringent phasematching and quasi-phase matching. The birefringent phasematching approach the polarization dependence of the refractive index difference is employed to compensate for the refractive index difference between the fundamental and second harmonic field. The direction of the propagation inside the crystal and, the nonlinear crystal temperature can be changed to increase the wavelength bandwidth of

the nonlinear crystal. Although this technique was widely used, due to its tight alignment tolerances, other techniques have been explored. The most widely used phase matching technique alternative to the birefringent phase matching technique is quasi-phase matching (QPM) technique [36,37].

Phasematching in QPM is achieved by artificially structuring the nonlinear material. The nonlinear crystal does not need to have a birefringence. Thus, with QPM we have wide choice of materials. As we can understand from equation x.x the second harmonic intensity oscillates as $\sin\left(\frac{\Delta k l}{2}\right)$. For the maximum intensity $\sin\left(\frac{\Delta k l}{2}\right) = 1$ and this results in $l = l_c = \lambda/4(n_{2\omega 1} - n_{\omega 1})$. This distance is called the coherence length. The direction of power flow between the fundamental and harmonic depends on the relative phase of the forced and free waves, and hence changes sign every coherence length. By changing the sign of the nonlinear susceptibility every coherence length, the phase of the polarization wave is shifted by π, effectively rephasing the interaction and leading to monotonic power flow into the harmonic wave [36], see figure 1.17.

In principle the π-phase change can be done by changing the sign of the nonlinear coefficient "d" from + to –. The most popular way to make this type of crystals with periodic polarization change at every coherence length can be done by technique so called domain inversion. The widely used materials for second harmonic generation are lithium niobate (LN) and potassium titanyl phosphate (KTP) [38,39]. These materials are ferroelectric materials. By applying relatively high electric fields through the crystals, domain inversion can be achieved. The crystal thickness is limited by dielectric breakdown of the material.

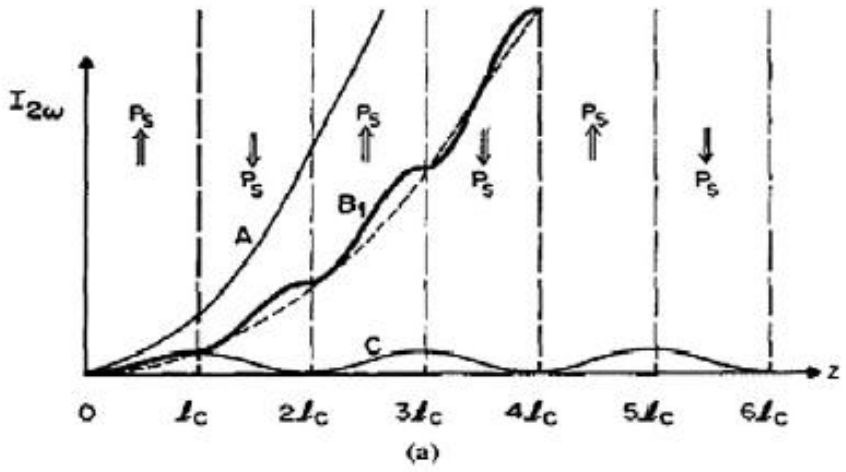

Figure 1:17 Effect of phase matching on the growth of second harmonic intensity with distance in a nonlinear crystal. A: perfect phasematching in a uniformly poled crystal; C: non-phasematched interaction; B: first-order QPM by flipping the sign of the spontaneous polarization every coherence length of the interaction of curve [35].

In this research, we investigated the QPM-SHG technique is used to convert the IR light emission from the nanosecond pulsed GCSEL based devices to generate high peak power blue light sources. Materials of choices were periodically poled (domain inverted) KTP and LN crystals.

As mentioned earlier, BALs are multi-moded in transverse direction. This is one of the drawbacks of the BALs for using as a fundamental source for SHG. Several research groups used various clever ways to decrease the number of transverse modes. Recently Jechow et. al. demonstrated an external cavity BAL with nearly Gaussian transnverse emission profile [40,41]. This type of mode filtering improves the beam quality, thus increases the second harmonic conversion efficiency. In this work a different type of external cavity is formed for the GCSEL devices. Our devices were multi-moded in one transverse direction. The aim in this work was to show multi-wavelength blue light

sources, so more research can be done in terms of improving the output beam quality to increase the second harmonic conversion efficiency.

1.5 Conclusion

This section provides a brief summary of the semiconductor diode lasers, and the characteristics of the semiconductor diode lasers for simple Fabry-perot cavity and external reflector cavity. Next, the different emission and wavelength stabilization configurations are summarized along with the basic operation of the GCSEL lasers. Then GCSEL-DGR and GECSEL wavelength stabilization approaches are briefly explained. Lastly, the background for the nonlinear frequency conversion using QPM second harmonic generation is explained, since this technique is investigated to generate high peak power blue light sourced based on GCSEL-DGR and GECSEL devices.

CHAPTER 2: RESEARCH OVERVIEW

The research in this work is mainly based on the external wavelength stabilization of GCSEL devices. This type of cavity is named as dual grating external cavity surface emitting laser (DGECSEL). The device consists of a GCSEL device with output couplers on the p-side and wavelength selective external feedback mirror. This work is an alternative approach to the monolithic wavelength stabilization of GCSEL devices (GCSEL-DGR) that was developed by O'Daniel et. al. [18].

Another part of the work was employing the GCSEL based devices as the fundamental light source for high peak power blue light generation through second harmonic generation. In this part of the work the GCSEL-DGR and DGECSEL type single, 1D-array, and 2-D array devices were driven under the ns-pulse condition and used as the fundamental light source. Micro-optics is designed and fabricated to focus the fundamental light into the nonlinear crystal. Different nonlinear configurations are also explored for multi-wavelength blue light generation.

The research goals during this work can be summarized as follows: 1^{st}) to demonstrate a stable external cavity GCSEL device, in which the emission wavelength can be selected by the external grating period. 2^{nd}) To demonstrate this DGECSEL approach in 1-D array configuration, by individually stabilizing each device in the array. 3^{rd}) The DGECSEL configuration is used as a fundamental source for blue light generation through second harmonic generation. 4^{th}) The monolithic GCSEL-DGR devices are also researched as the fundamental source for blue light generation. 5^{th}) A

Master oscillator Power amplifier (MOPA) configuration consisting of a GCSEL-DGR device and a grating coupled amplifier is researched for generation of high peak blue light.6th) The performance of a novel vertically stacked 1-D GCSEL-DGR configuration is explored and this configuration is utilized for blue light generation. 7th) A novel vertically stacked 2D- DEGCSEL array is fabricated and tested.

2.1 External cavity wavelength stabilized GCSEL

The first goal of this research was to be able to fabricate an external dispersion element to stabilize the emission wavelength of the broad area GCSELs. This type of cavity configuration is named as dual grating external cavity surface emitting laser (DGECSEL) (see Figure 2.1). These gratings are operating under Littrow condition to retro-reflect the light with a specific wavelength back into the active medium. The reflectivity of the Littrow grating is numerically modeled to optimize the grating duty cycle, depth, and the effect of the high reflection coating to maximize the retro-reflected light.

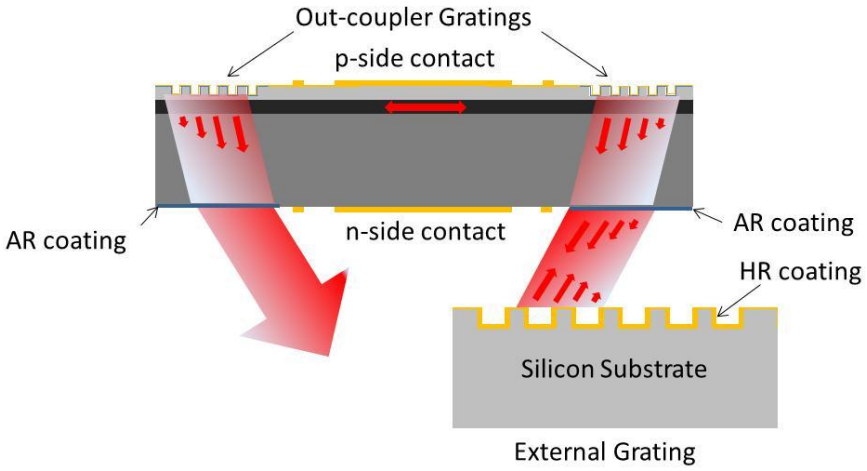

Figure 2:1 Schematics of dual grating external cavity surface emitting laser (DGECSEL) configuration

2.2 Single Wavelength and Multi-Wavelength DGECSEL array

The second goal of the research was to go one step further and use the external wavelength stabilization idea and fabricate gratings with same and different periodicities on one silicon die to integrate on to the GCSEL array chip. Figure 2.2(top) and (bottom) shows the schematics for the single wavelength and multi-wavelength DEGCSEL array. The main idea for the multi-wavelength DEGCSEL array was to be able to investigate the possibility of the accuracy of the wavelength selection of each device in the array prior to the integration of the gratings.

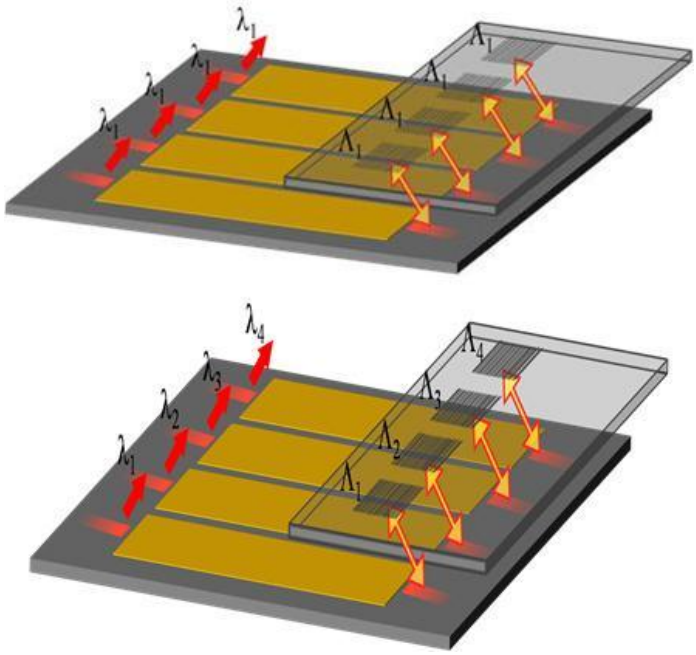

Figure 2:2 Schematics of single wavelength (top) and multi-wavelength(bottom) 1-D DGECSEL array

2.3 Blue light source based on single wavelength and multi-wavelength DGECSELs

Thirdly, the DGECSEL configuration is utilized as a fundamental source for high peak power blue light generation through QPM-SHG. The nonlinear conversion efficiencies for single DGECSEL, 1-D single wavelength and multi-wavelength DGECSEL array is investigated (see Figure 2.3).

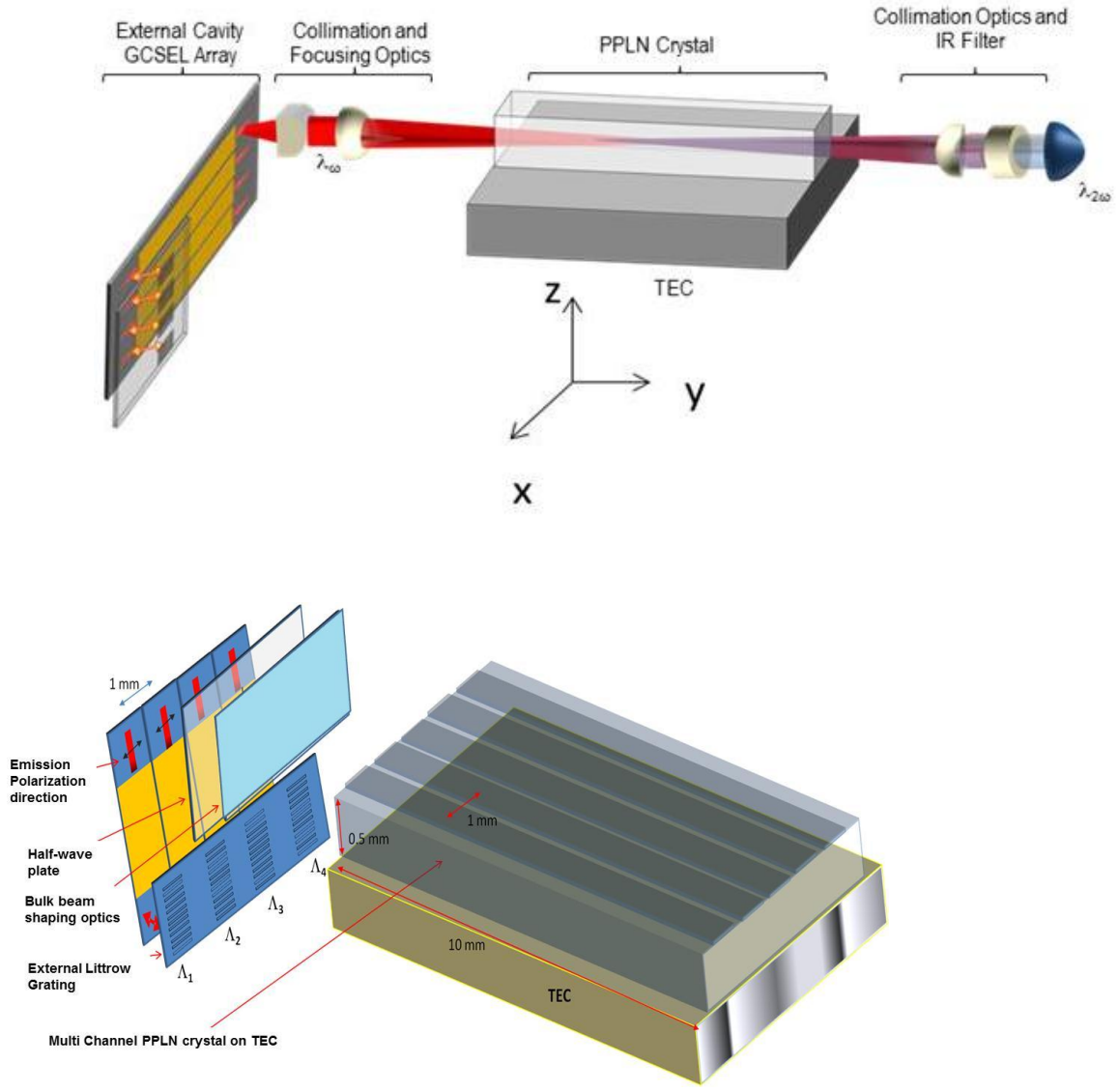

Figure 2.:3 Schematics of (a) Single wavelength and (b) Multi-wavelength QPM-SHG setup based on 1-D DGECSEL array

2.4 Single Wavelength GCSEL-DGR based blue light source

One of the approaches pursued in this research was to use GCSEL-DGR based devices as the fundamental source for high peak power blue light generation. Again, QPM- SHG technique is employed to convert the near-IR GCSEL-DGR wavelength into its second harmonic (see Figure 2.4). The efficiency of the nonlinear conversion is characterized.

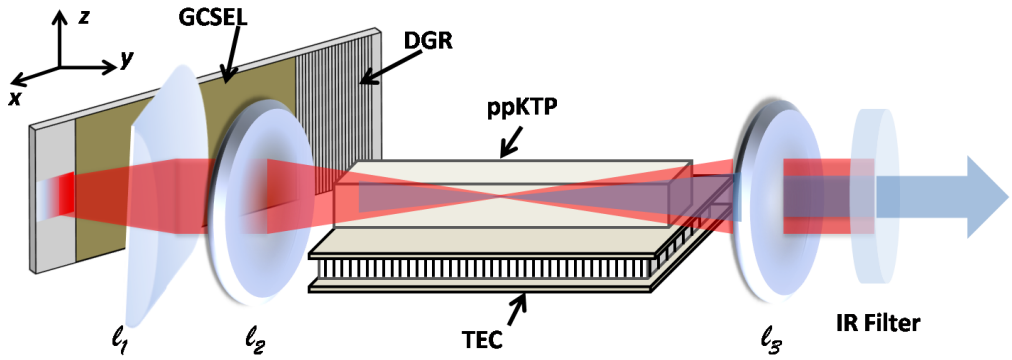

Figure 2:4 Schematics of GCSEL/DGR Laser Diode and SHG setup

2.5 Single Wavelength MOPA based blue light source

In this part of the work a grating coupled power amplifier configuration is coupled with the GCSEL-DGR device to increase the input fundamental peak power for QPM-SHG (see Figure 2.5). Same SHG setup is used to compare this approach with a single GCSEL-DGR fundamental source.

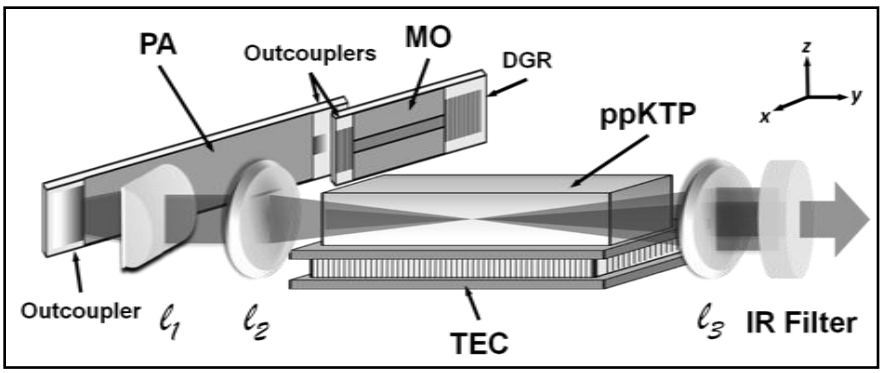

Figure 2:5 Schematics of MOPA and SHG setup

2.6 Multi-Wavelength vertically stacked GCSEL-DGR array based blue light source

One of the main goals of this research was to be able to design a compact GCSEL-DGR based multi-wavelength blue light source. In this part of the research, four GCSEL-DGR devices with different emission wavelengths were stacked on top of each other without blocking the emission facets of the individual devices. A beam shaping micro-optics is designed and fabricated using a additive lithography technique. A multi-grating nonlinear periodically poled lithium niobate (PPLN) crystal with different channels were designed to form a compact QPM-SHG setup (see Figure 2.6). The efficacy of this compact cavity is explored.

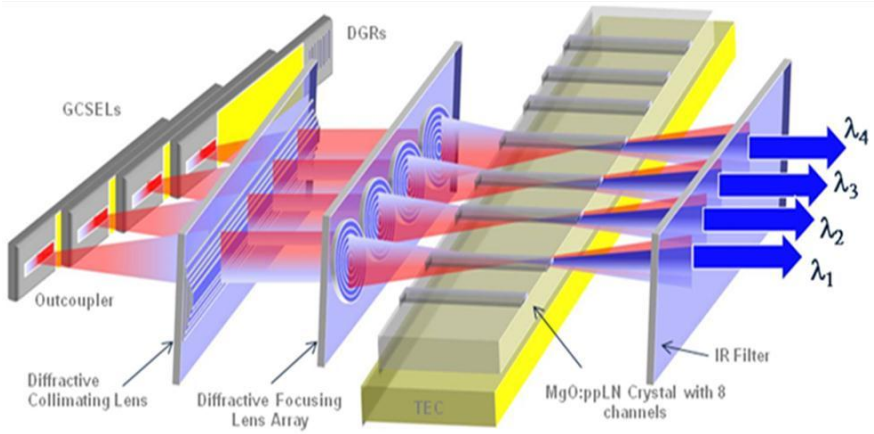

Figure 2:6 Schematics of GCSEL/DGR Laser Diode stack and SHG setup

2.7 2-D vertically stacked multi-wavelength DEGCSEL device

Lastly, DEGCSEL idea is carried to the 2-D configuration by vertically stacking the GCSEL arrays and the external gratings on silicon dies (see Figure 2.7). This multi-wavelength 2-D vertically stacked multi-wavelength device is tested under QCW and 20-ns pulse condition. The light output and spectral characteristics were investigated.

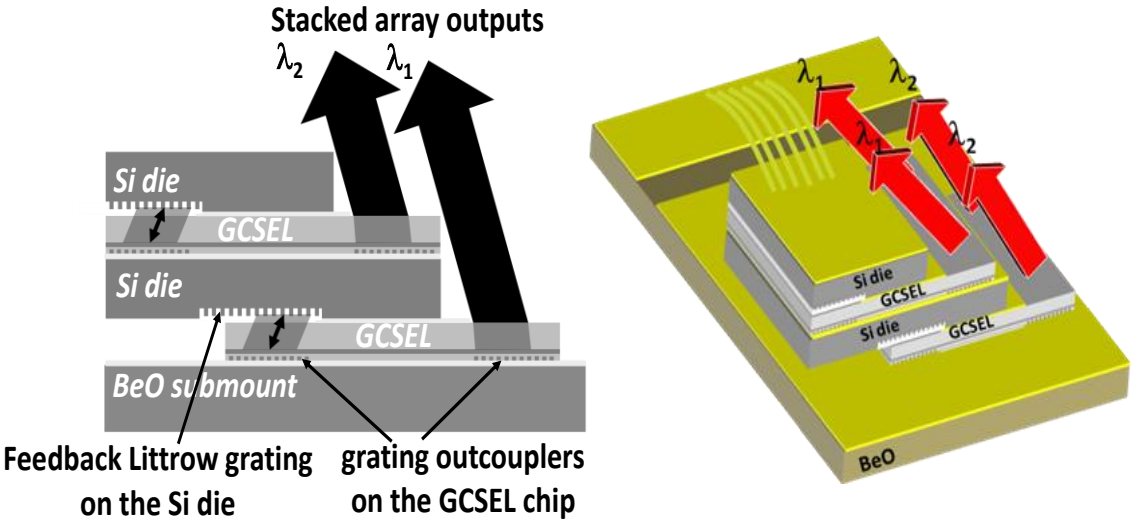

Figure 2:7 Schematics of 2-D vertically stacked multi-wavelength DGECSEL device

2.8 Conclusion

The scope of this dissertation is to design a compact broad area GCSEL based external cavity lasers and laser arrays. External gratings were fabricated on Si wafers and gratings on Si dies were flip-chip bonded on to the GCSEL devices to form this compact cavity to stabilize the wavelength of the GCSEL devices and arrays in 1-D and 2-D configurations. The performances of these devices were experimentally tested. The second leg of the research was to investigate the possibility of these broad area devices as

a fundamental source for blue light generation through QPM-SHG. In this part of the research SHG conversion efficiencies of DGECSEL configuration and previously developed GCSEL-DGR configuration is explored.

CHAPTER 3: MODELING AND DESIGN

Numerical modeling of optical components is essential to optimize the design before its fabrication. In this work, the external dispersive reflective element is modeled to maximize its reflectivity back into the gain medium. The GCSEL grating out-coupler parameters were kept constant, since these parameters were optimized previously by Vassie et. al. [40] and O'Daniel et. al.[18] at Micro-Photonics Laboratory. The design of the multi-channel nonlinear crystal and the multi-level diffractive micro-optics is also discussed in this chapter.

3.1 Design and modeling of external dispersive feedback element for GCSEL

As stated previously, a grating structure operating under Littrow condition is chosen as the wavelength stabilization element. The parameters that are important in the design of this element are grating period, grating fill factor or duty cycle, grating depth, and the high reflection coating.

The emission wavelength of the DGECSEL cavity is calculated using Eq. 1.18. Rewriting this equation in Eq. 3.1 and remembering Λ_{out}, Λ_{fb}, n_{eff}, λ_{sw}, are period of the GCSEL out-coupler grating, external Littrow grating period, effective index of the waveguide at the GCSEL out-coupler region, and the emission wavelength, respectively.

$$\lambda_{sw} = \frac{2\Lambda_{out}\Lambda_{fb}}{2\Lambda_{fb}-\Lambda_{out}} n_{eff} \qquad \text{Eq. 3.1}$$

3.1.1 GCSEL out-coupler grating design

Out-coupler grating design is important for the efficient DGECSEL operation. Vassie et. al. have researched the design of the GCSEL out-coupler with an improved out-coupling efficiency from the n-substrate of the device [39]. Numerically calculated effective refractive index of the waveguide at the grating out-coupler region is ~3.24. The period of the grating coupler must be chosen to satisfy the following two requirements: maximize the coupling efficiency into one order and to decrease the effective reflectivity. The period of the grating coupler must then be chosen so that only one order of diffraction is allowed in the substrate. This condition is met by the following condition [40] :

$$\Lambda_{out} < \frac{2\lambda}{n_s + n_{eff}} \qquad \text{Eq. 3.2}$$

where n_s is the refractive index of the substrate, and it's 3.54 at 980 nm for GaAs. This equation puts out Λ_{out} < 286 nm. Hagberg et. al. that indicated larger slope efficiencies are obtained for negative detuning with respect to the second order Bragg resonance at 290nm by suppressing the second diffracted order in the substrate [40]. The value is optimized to 270 nm with experimentally measuring the slope efficiencies of the fabricated devices with different out-coupler grating periods.

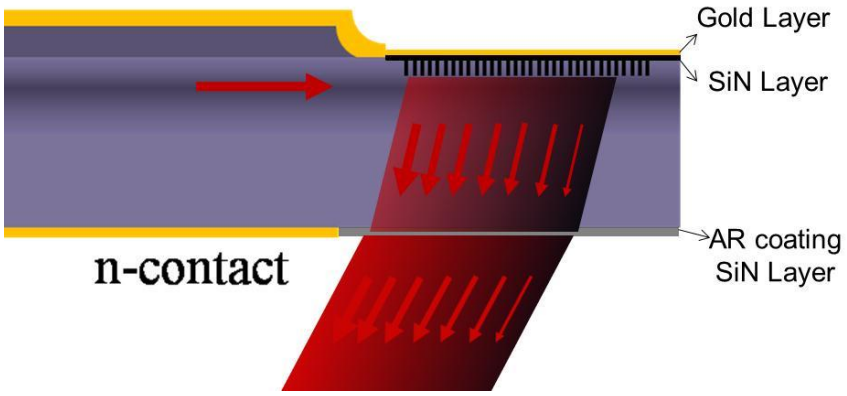

Figure 3:1single side of the GCSEL device

These out-coupler gratings that are detuned from the 2nd order Bragg condition offer a very low reflectivity, which is essential to the stable operation of the DGECSEL device. Using coupled mode theory, the in-plane power reflection coefficient is given by [41]

$$R = \frac{\kappa^2 sinh^2(\alpha L)}{\alpha^2 \cosh^2(\alpha L) + \delta \sinh^2(\alpha L)}$$

where κ, α, L, δ are grating coupling coefficient, attenuation coefficient, grating length, and detuning coefficient, respectively. The effective reflectivity of the 50% duty cycle, 270 nm period grating with L = 100 μm is calculated to be ~ 10^{-4} at around 977 nm emission wavelength[38]. The directionality of the out-coupler gratings are improved by a dielectric-gold over coating on top of the grating structure [38].

3.1.2 External Littrow Grating Design

In order to optimize the external Littrow grating parameters, 2-D finite difference frequency domain (FDFD) technique is utilized. The design parameters are grating period, grating duty cycle, grating depth, high reflection coating thickness, and the incidence angle of light.

The grating period is calculated using Eq. 3.1, the grating duty cycle largely depends on the fabrication process. Therefore the duty cycle of the gratings were set after fabrication of the grating structures, and is found to be ~ 25%. The angle of incidence of light on the external grating depends on the effective index of the out-coupler grating region, and the wavelength of operation. This value is calculated using the grating equation and the Snell's law between the GaAs-air interface. The angle of the light from the n-side output facet of the GCSEL device is 20-22 degrees for an emission wavelength around 970 nm-980 nm.

Figure 3.1 shows the design structure used in the FDFD simulation of the reflected power from the Littrow grating. The boundary conditions have a tremendous affect in the accuracy of the numerical simulations. The design space is limited with the memory of the computing tool. For periodic structures such as gratings, so called periodic boundary conditions can be employed to minimize the use of memory without sacrificing the accuracy of the numerical output. As can be seen in Figure 3.1 only one period of the grating is sufficient to define the structure. The grating substrate is silicon with an index of 3.451, the complex refractive index of the gold coating layer is 0.21-i6.47. The duty cycle of the grating is chose as 25% The curves on figure 3.1 shows the reflected power for the 0^{th} order and the 1^{st} order reflected light as a function of the grating depth. The optimum grating depth for a 25% duty cycle grating with a etch depth between 1 μm and 1.5 μm is calculated to be ~ 1.22 μm.

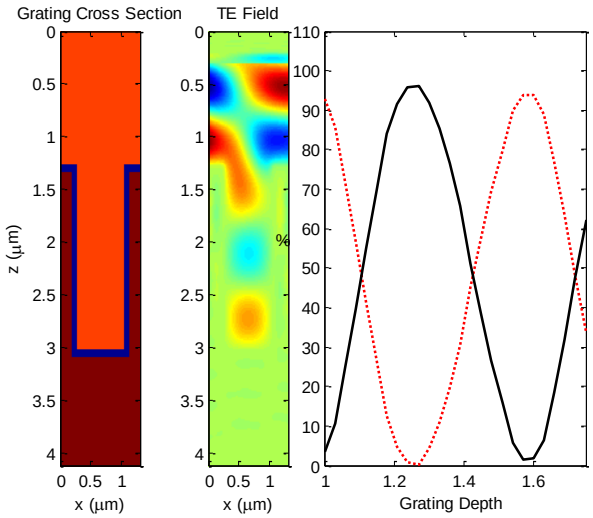

Figure 3:2 Grating designed used in the FDFD analysis for an incident TE-polarized field and the corresponding reflected power for the 0th order and -1st order as a function of grating depth

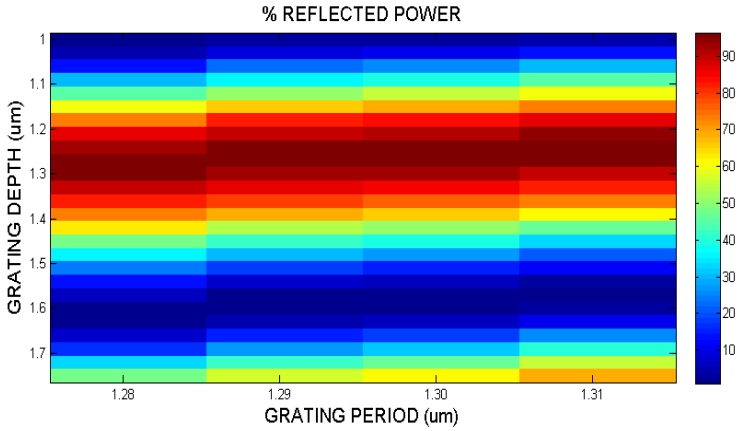

Figure 3:3 The % reflected power plot as a function of grating depth and grating period

3.2 Nonlinear crystal design for second harmonic generation

A multi-channel periodically poled nonlinear crystal is designed for the 1-D GCSEL-DGR and DGECSEL array. A 5% Mg:O doped PPLN crystal is fabricated by HC Photonics. Each channel in the crystal have a period that will match to the

fundamental input source wavelength for efficient QPM based SHG. The fabrication of periodically poled crystals are explained in Appendix II, at the end of this dissertation.

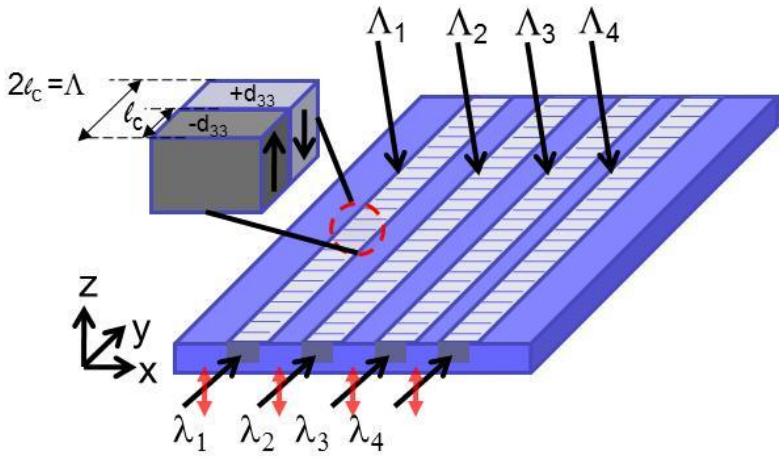

Figure 3:4 Schematics of a multi-channel nonlinear crystal for QPM type SHG

The refractive index of the crystal over the fundamental and second harmonic frequency and over temperature is essential to calculate the necessary poling period. The dependence of the refractive index of 5% MgO doped PPLN crystal over temperature and wavelength is calculated using Sellmeir equation below [42]. The Sellmeir coefficients are given in table 3.1.

$$n^2 - 1 = A\frac{\lambda^2}{(\lambda^2 - B)} + C\frac{\lambda^2}{(\lambda^2 - D)} + E\frac{\lambda^2}{(\lambda^2 - F)}$$

Table 0-1Sellmeier Coeffcieints for Congrently Grown LiNbO3 doped with 5-mol % MgO

coefficient	ne	No
A	2.4272	2.2454
B	0.01478	0.01242
C	1.4617	1.3005
D	0.05612	0.05313
E	9.6536	6.8972
F	371.216	331.33

The calculated refractive index for 5% MgO doped PPLN at 30°C as a function of wavelength is shown in Figure 3.5

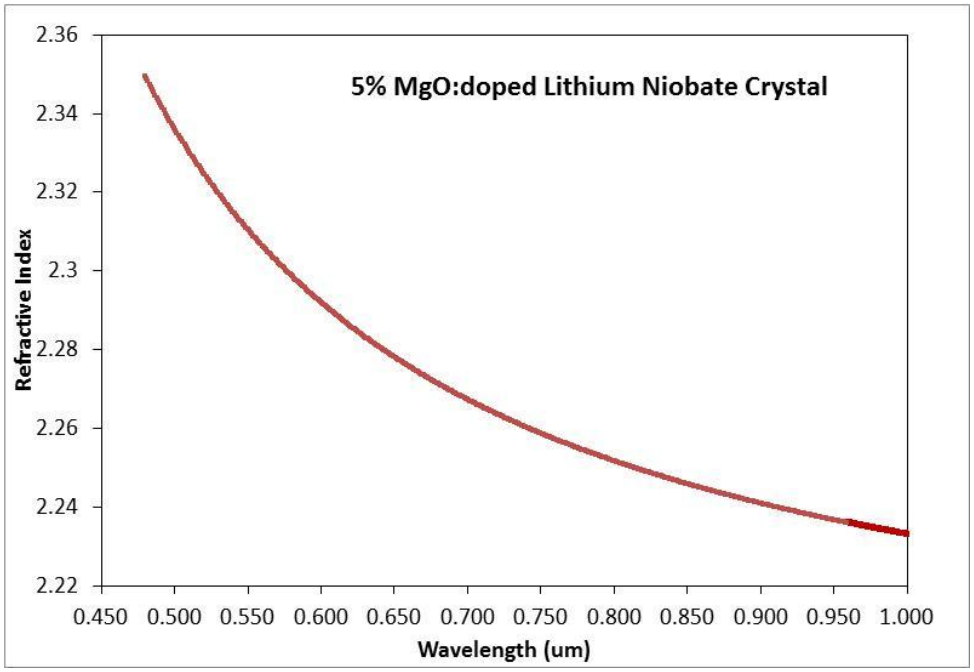

Figure 3:5 Refractive index vs. wavelength for 5% MgO:doped Lithium Niobate Crystal

The poling period for each channel is determined by using the calculating refractive indices of the crystal for each fundamental input light. In terms of the wavelength separation between the neighboring emitters ~0.08 nm is the target. Thus, the crystal periods are calculated according to this wavelength separation. The poling period is calculated using Equation 3.5

$$\Lambda = \frac{\lambda^{(\omega)}}{2(n_{\omega} - n_{2\omega})} \qquad \text{Eqn. 3.5}$$

Figure 3.6 shows an example of the optimum fundamental wavelength variation for different channel periods as a function of temperature.

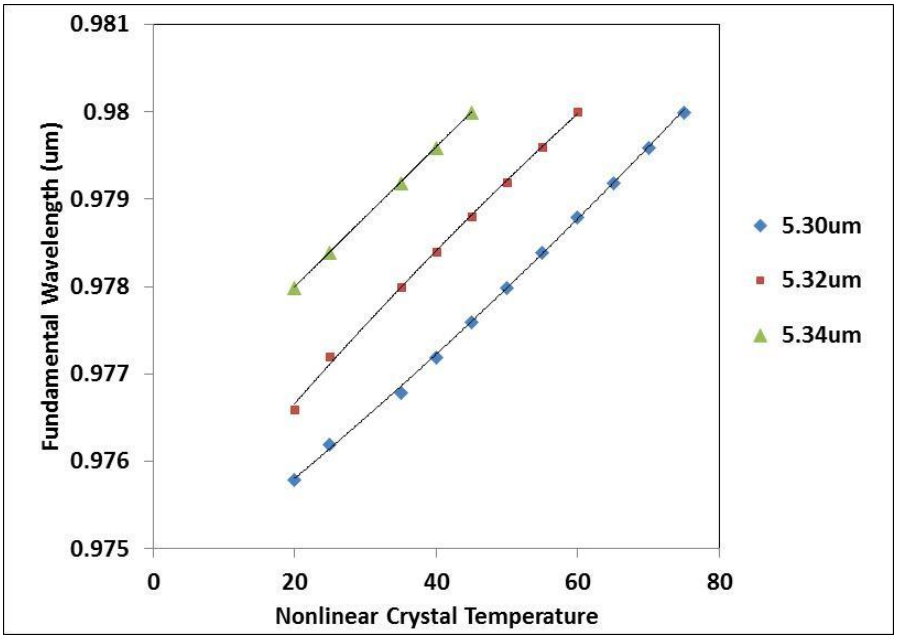

Figure 3:6 The dependence of the optimum fundamental wavelength for different channel periods as a function of temperature of the crystal

3.3 Beam shaping diffractive micro-optics design

One of the goals of the research on the blue light generation is to miniaturize the second harmonic generation setup. Also focusing an array of laser light into the individual channels of the nonlinear crystal will be quite challenging with bulk optical elements. There are very few techniques available for the fabrication of scaled down versions of these refractive lenses. Possible alternative for a scaled down version of an optical elements is micro diffractive optical elements. These diffractive optical elements change the incoming wave-field by diffraction. Diffractive optical elements can have either continuous or multilevel microreliefs.

Two different diffractive optical elements were fabricated for focusing the GCSEL-DGR array emission into the individual channels of the nonlinear crystal: A plano-convex lens with a spherical sag, and a cylindrical lens is converted into its diffractive equivalent. The GCSEL lasers have a high divergence in one plane (xz-plane) and a very low divergence in the perpendicular plane (xy-plane). The full width at half max of the the slow divergence and fast divergence angles are measured to be ~ 1.4° X 10°. One of the possible ways to focus this elliptical beam is to collimate the both axis using a two cylindrical lenses in both directions and another spherical lens to focus into a single spot. For the GCSEL laser a single cylindrical lens were used to collimate the light highly divergent axis, the second axis divergence is very small so another cylindrical lens was not necessary. The schematic of the laser and diffractive optics is shown in Figure 3.7. A diffractive cylindrical lens with a back focal length of 6-mm was needed for collimating the highly diverging axis, and a diffractive spherical lens with a diameter of 400um with a focal spot of 10 mm is fabricated to focus the laser beam. The GCSEL output is highly multi-moded. Therefore the focused spot is not a pure fundamental Gaussian beam. This decreases the overall performance of the lens system.

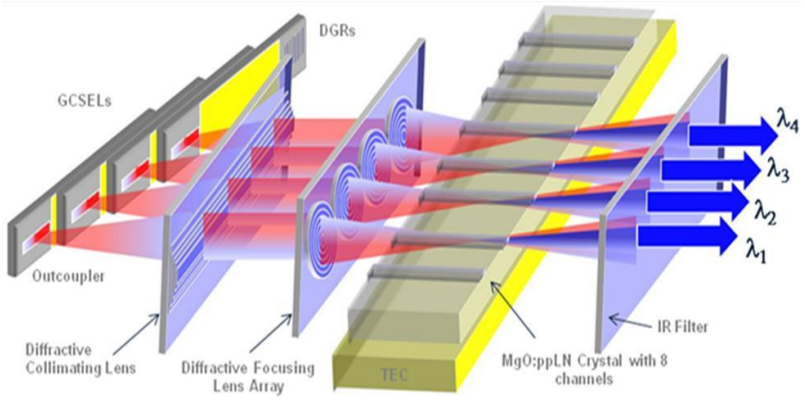

Figure 3:7The schmeatic of the GCSEL arrray and the diffractive lenses

The transmisstance of a refractive lens with focal length *f* is given by [43]

$$t(x,y) = e^{i\frac{k(x^2+y^2)}{2f}}$$

this phase function modifies the incoming phase of the wave. Figure 3.8 shows the phase function of the 400um diameter lens with a spherical phase function. This refractive lens can be broken down as integral multiple of 2π in phase. Figure 3.9 shows the 2π-phase depth diffractive equivalent of this lens. The structure is an analog structure, because the surface relief is continuous and for each zone as shown in Figure 3.10. The zone period decreases as we go out from the center of the lens. The radius of the p^{th} zone of the diffractive phase elemens is $r_p = (2p\lambda f)^{1/2}$ and the sag is $z = \lambda / [n(\lambda)-1]$ [44]. From the last equation we can easily see the wavelength dependence of the diffractive lenses. Therefore the diffractive lenses efficiency decreases at wavelengths far from the design wavelength.

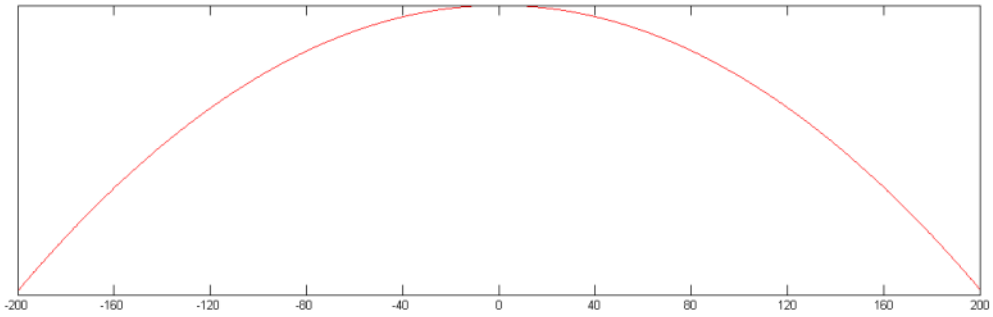

Figure 0-8Phase profile of the 400um spherical lens with 10 mm focal length

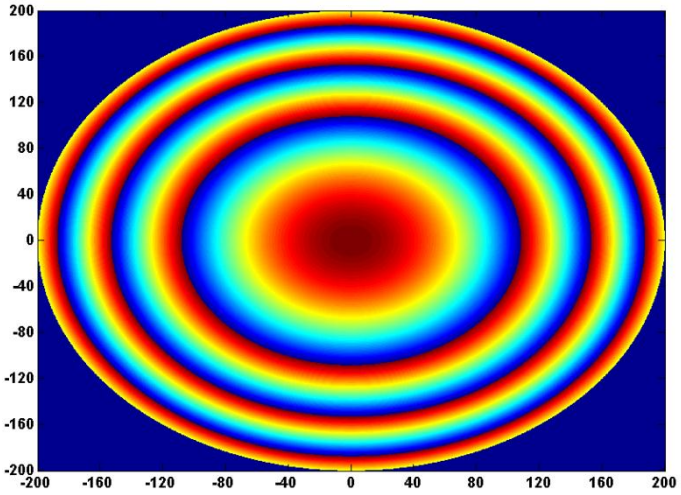

Figure 3:9 2π-phase depth analog diffractive equivalent of the 400 um lens.

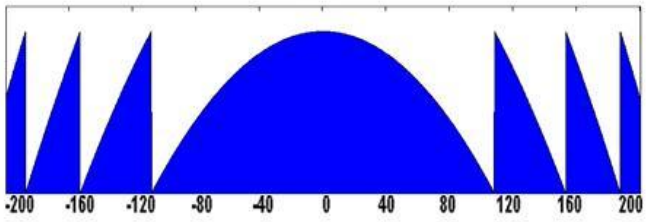

Figure 3:10Cross section of the analog diffractive lens

The quantization of these analog diffractive lenses into their multi-level equivalents eases the fabrication of these optical elements. Amplitude masking can be employed to fabricate these multi-level diffractive optical elements. This technique is explained in the next chapter.

The design of the multi-level equivalent of the analog diffractive elements starts with quantizing the zone periods of the analog diffractive into subperiods. These subperiods or levels can be represented by a rect function [REF] centered at $x = [L/N*(l+0.5)]$, where L is the zone periods. The phase shift introduced by each subperiod is

$$2\pi\emptyset_l = \frac{l\emptyset_0}{N}2\pi$$

where $\emptyset_0$ is the largest phase shift introduced by all the subperiods. The far field amplitude of the p[th] diffracted order can be calculated as [45]

$$A_p = e^{-i(\frac{\pi p}{N})} \frac{\sin(\frac{p\pi}{N})}{\frac{p\pi}{N}} \frac{1}{N} \sum_{l=0}^{N-1} e^{-i(\pi(p-\emptyset_0)l)/N}$$

and the diffraction efficiency for the p[th] order is

$$\eta_p^N(\emptyset_0 \to 1) = \left[\frac{\sin(\frac{p\pi}{N})}{\frac{p\pi}{N}} \right]^2$$

The diffraction efficiency of the structure increases the number of levels are increased. Figure 3.11 shows the diffraction efficacy of a multi-level diffractive optical element as a function of the number of levels.

An 8-phase level structure achieves ~ 0.95 percent diffraction efficiency; the residual 5 percent of the light is diffracted into higher orders or scatters. This is a tolerable amount of scatter for our optical system. We can increase the diffraction efficiency to 99 percent by fabricating a 16-phase level structure, although the diffraction efficiency is increased the fabrication becomes more involved and 8-level structure is relatively efficient for our purposes. The analog diffractive and its 8-level equivalent is shown in Figure 3.12. The cylindrical lens is designed in a similar manner.

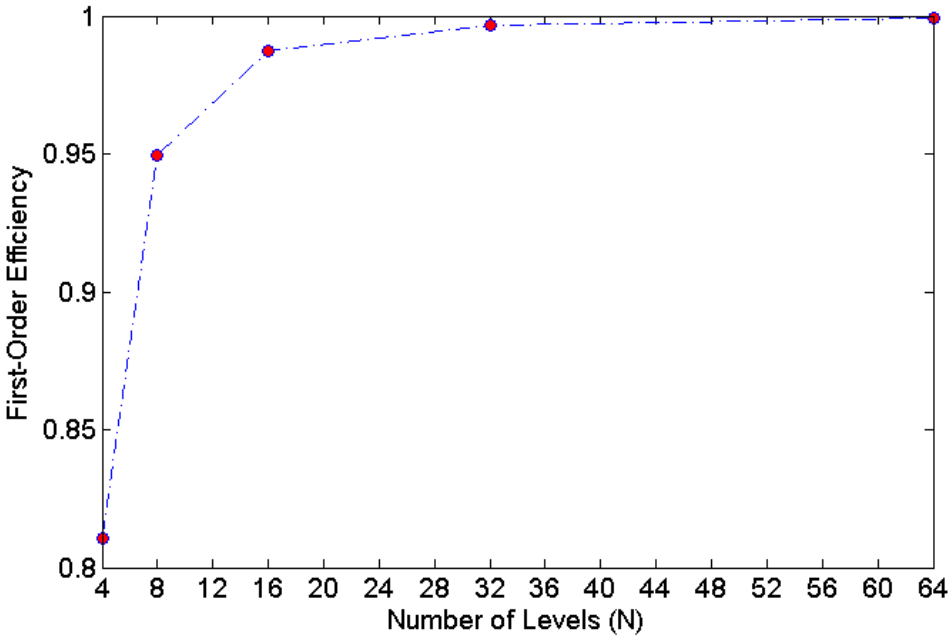

Figure 3:11 Diffraction efficiency vs. number of levels on a diffractive optics structure

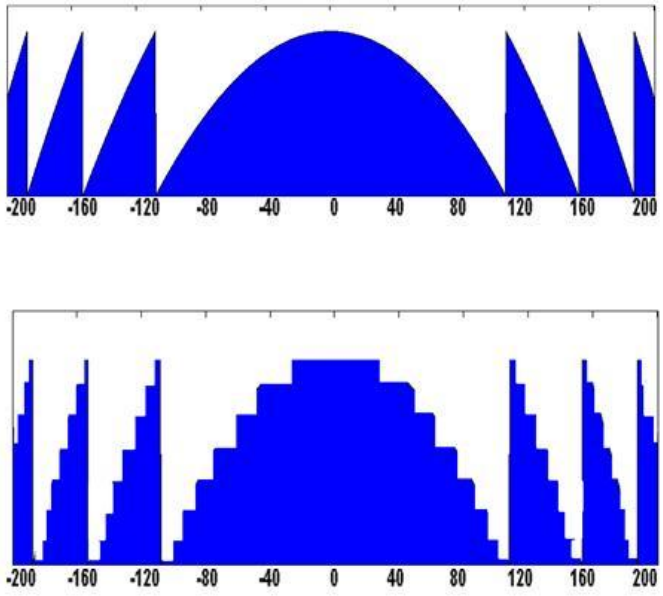

Figure 3:12The 8-level equivalent of the analog diffractive optics

2.9 Conclusion

Design and modeling of the devices fabricated in this work is presented. The design of the external gratings is optimized using FDFD numerical algorithm. The phase profile of the beam shaping micro-optics is converted to 8-level diffractive optical equivalent my using a Matlab script.

CHAPTER 4: FABRICATION

In this part of the thesis, the fabrication steps are explained. Firstly, we will start with the GCSEL device fabrication. Next, the external dispersive feedback mirror fabrication will be explained. Thirdly, the fabrication of the diffractive optical elements on fused silica is covered. The integration of the external gratings onto the GCSEL devices is also explained briefly. Qualitative characteristics of the fabricated external gratings, diffractive optical lenses are also explained in this chapter, since characterization of these elements is crucial to reach the optimum performance.

4.1 GCSEL fabrication

The GCSEL fabrication starts with a ~1x1 (inch x inch) epi die. The epi layers were previously explained in chapter 1. The substrate is thinned down to ~150um. Depending on the die, some die have already p-contacts. Figure 4.1 shows the unfinished and finished GCSEL device for ease of understanding of the process steps that will be explained next.

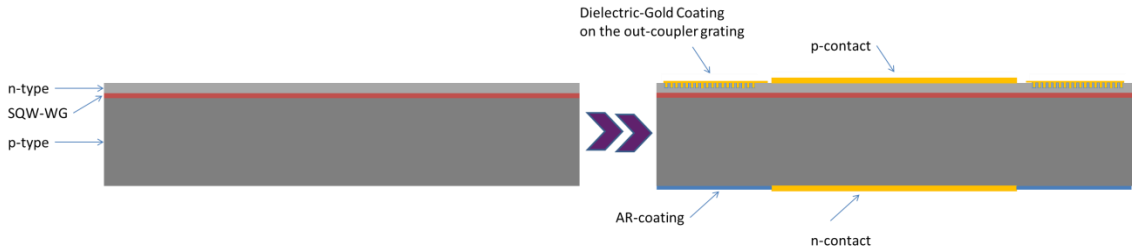

Figure 4:1 Starting epi dice (on the left) and final GCSEL device (on the right) cross-sectional view.

The detailed fabrication steps for the GCSEL device fabrication is as follows (the order of processing is not necessarily the order during fabrication of these devices, in terms of the order of the contact fabrication steps) :

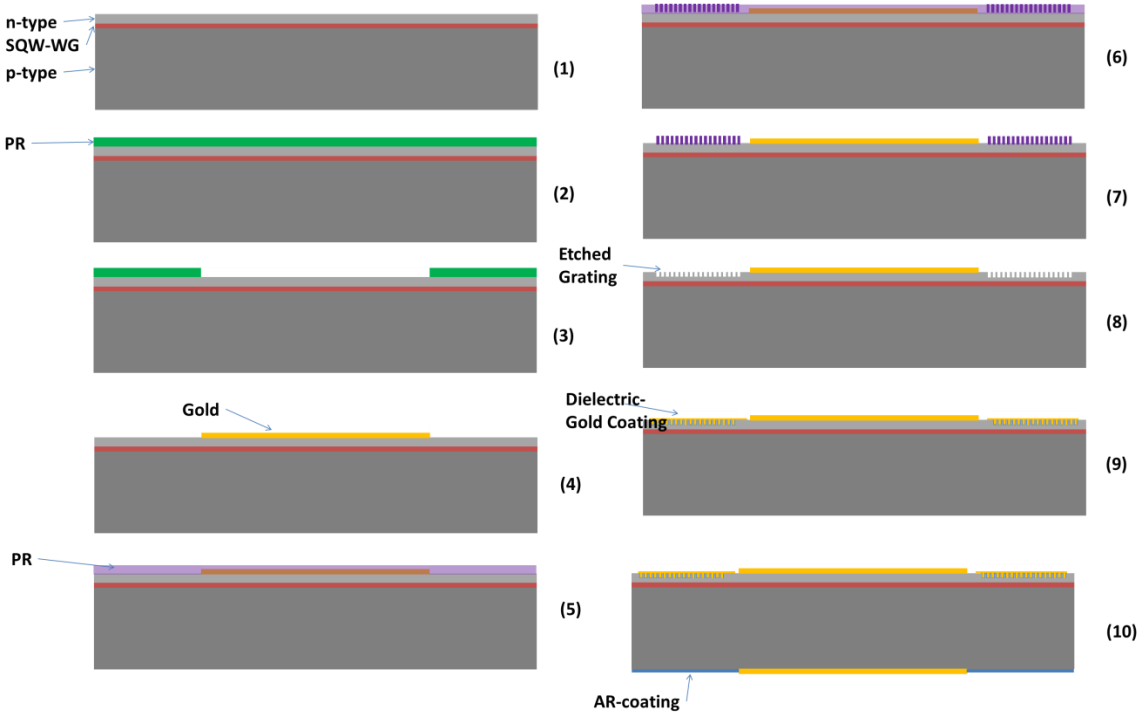

Figure 4:2 Schematics of GCSEL device fabrication steps

(1) III-V GaAs epi die, (2) Coat with photoresist (PR) on the p-side, (3) Contact exposure for p-side contact opening ,(4) E-beam evaporated Au p-side contact after lift-off process, (5) ZAP resist spin on the p-side, (6) Grating structure written on the E-beam in the ZAP resist, (7) Developed resist with grating structure after e-beam exposure, (8) Grating structure etched into the p-side all the way to the etch-stop layer, (9) Dielectric (SiN) –Au coating for increased directionality of the diffracted beam into the substrate,

and (10) Final structure after n-side contact fabrication (same steps as 3&4) and SiN anti-reflection (AR) coating on the n-facets. The detailed explanation of the process steps can be found in the doctoral dissertation's of Laurent Vaisse [39] a former member of the Microphotonics Laboratory.

4.2 External dispersive grating fabrication

The external grating structure is fabricated on the silicon substrate using projection lithography (SEE APPENDIX for detailed explanation of the operating principle of the projection lithography). The GCA g-line tool is 5X projection tool, meaning a structure on the mask will be imaged on the wafer five times smaller. This reduces the errors coming from the mask itself and, enables the fabrication of the smaller structures. There are other advantages of this system, one being the use of the wafer stage movement to further increase the resolution of the stepper. The accuracy of the GCA tool's wafer carrier stage is 50 nm. We used so called "double exposure" technique to increase the resolution of the system.

Double exposure technique is useful for fabrication of periodic structures that are close to the limit of the stepper tool. The number of exposures can be increased for different structures; one example is the fabrication of guided mode resonance filters [46]. In the case of double exposure, the grating period on the mask is doubled. For example: If we want to pattern 1 um period gratings on the wafer, the period of the grating patterns on the single exposure mask is 5 um due to the 5X projection of the tool ; but for double exposure mask this period is 10um. During exposure, the wafer is exposed twice, and between the exposures the wafer carrier stage is moved 1um in the grating vector

direction, thus making a 1 um period grating pattern at the end of the exposures. Schematics of the double exposure technique is shown in Figure 4.3

The choice of the substrate for external gratings was Silicon (Si). The gratings can be fabricated on any choice of substrate with applicable processing methods. The reason behind the selection of the Si as the substrate is two folds: firstly, the fabrication methods

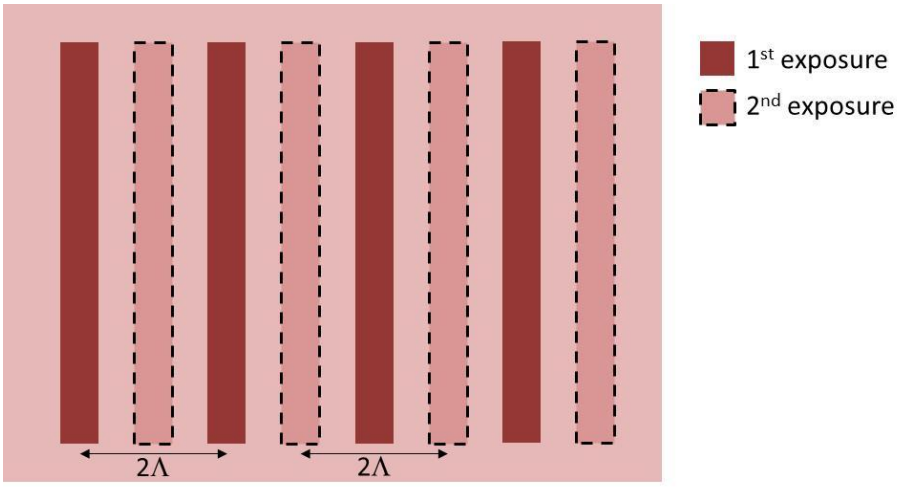

Figure 4:3 Schematics of the double exposure technique applied on the grating fabrication

are matured due to the CMOS processes developed for Si, and lastly the ease of integration of the Si die onto the GCSEL laser using flip-chip bonding. The flip chip bonding simplifies the alignment of the grating during integration on the laser.

There are two main paths to transfer the exposed grating pattern into the Si substrate: wet etching and dry etching. We used dry etching technique due to the advantages over the wet etching technique, which will be explained in this section. For completeness, we will go over the wet etching of Si as well.

During wet etching the material is dissolved when immersed in a chemical solution. It is a simpler approach compared to dry etching; unfortunately, there are disadvantages since usually a mask is desired to selectively etch the material. The mask should not dissolve or at least etch much slower than the material to be patterned. Secondly, single crystal materials such as Si exhibit anisotropic etching in certain chemicals. The difference between anisotropic and isotropic etching is the different etch rates in different directions in the material. One classic example of this is the <111> crystal plane sidewalls that appear when etching a hole in a <100> silicon wafer in a chemical such as potassium hydroxide. This results in a pyramid shaped hole instead of a hole with rounded sidewalls with an isotropic etchant. The principle of anisotropic and isotropic wet etching is illustrated in the figure 4.4.

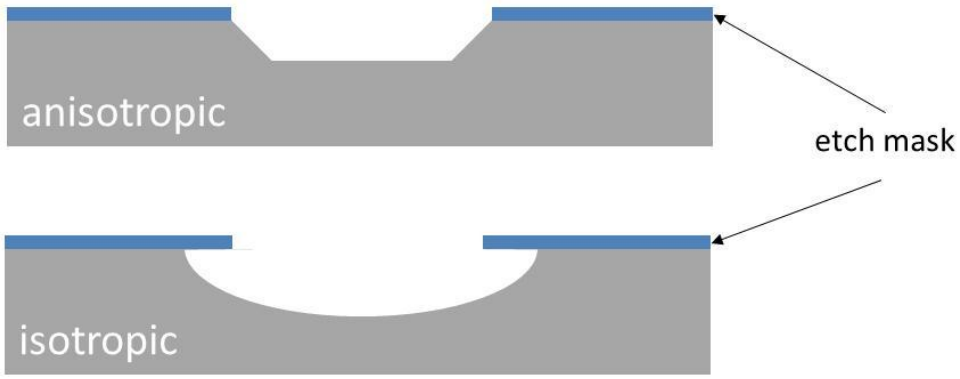

Figure 4:4 Illustration of the anisotropic and isotropic wet etching

There are mainly three separate types of dry etching technology: reactive ion etching (RIE), sputter etching, and vapor phase etching [47].

In RIE, the substrate is placed inside a reactor chamber in which several gases are introduced. Plasma is struck in the gas mixture using an RF power source, breaking the

gas molecules into ions. The ions are accelerated towards, and react with the material being etched. This part is the chemical part of reactive ion etching. There is also a physical part. If the striking ions have high enough energy, they can knock atoms out of the material to be etched without a chemical reaction. Balancing the chemical and physical etching in dry etch process is a complicated task. By changing the balance it is possible to influence the anisotropy of the etching, since the chemical part is isotropic and the physical part highly anisotropic the combination can form sidewalls that have shapes from rounded to vertical. A schematic of a typical reactive ion etching system is shown in the figure 4.5 below [REF].

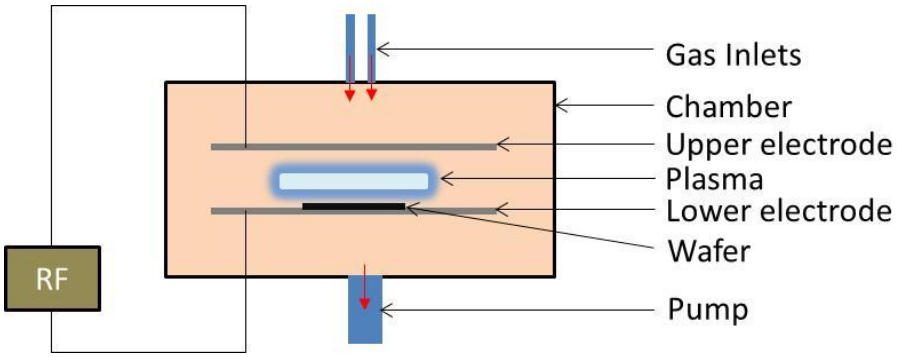

Figure 4:5 Schematics of a typical RIE system

Another technique which is very similar to RIE is deep RIE (DRIE). In this process, etch depths of hundreds of microns can be achieved with almost vertical sidewalls. This technology is based on the so-called "Bosch process", named after the German company Robert Bosch which filed the original patent [48], where two different gas compositions are alternated in the reactor. The first gas composition creates a polymer on the surface of the substrate, and the second gas composition etches the substrate. The polymer is immediately sputtered away by the physical part of the etching,

but only on the horizontal surfaces and not the sidewalls. Since the polymer only dissolves very slowly in the chemical part of the etching, it builds up on the sidewalls and protects them from etching. As a result, etching aspect ratios of 50 to 1 can be achieved. The process can easily be used to etch completely through a silicon substrate, and etch rates are 3-4 times higher than wet etching [49].

Another technique known as sputter etching is essentially RIE without reactive ions. The substrate is subjected to the ion bombardment instead of the material target used in sputter deposition.

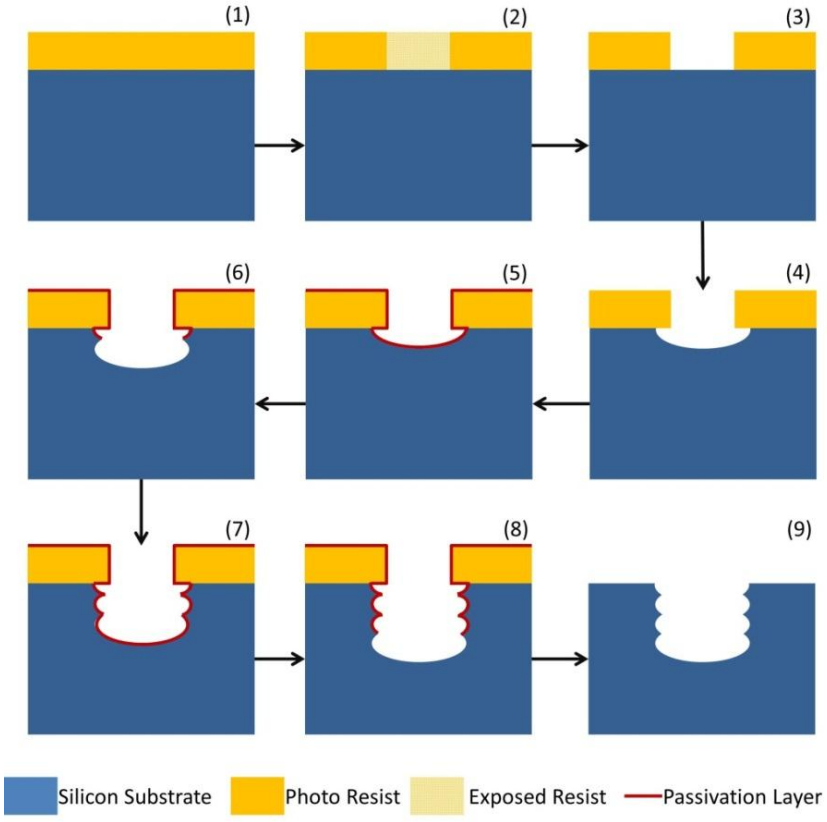

Figure 4:6 Schematics of the steps of external grating element fabrication using Bosch process

As stated previously the choice of etching technique for the gratings on silicon substrate is dry etching. The reasons behind this choice were as follows: (1) no

dependence on the wafer crystal orientation, (2) anisotropic etching, (3) speed of processing, and (4) selectivity of the etching process. We used a STS DRIE tool and employed the "Bosch" process. This method enabled us to get close to straight grating walls. Although we still see the characteristics scalloping effect on the sidewalls due to the nature of the Bosch process. We used a Shipley-1805 positive photoresist during the fabrication; the thickness of the PR on the Si substrate was ~500nm. Figure 4.6 shows the steps of Bosch process dry etching during the fabrication of the grating structures.

Figure 4.7 shows examples of scanning electron microscope images of the fabricated gratings. The depth of the gratings was adjusted by changing the cycling times of the Bosch process. The duty cycle of the gratings was around ~ 0.2-0.3 % which was mainly due to the exposure dose, and development time of the exposed resist after post-exposure baking.

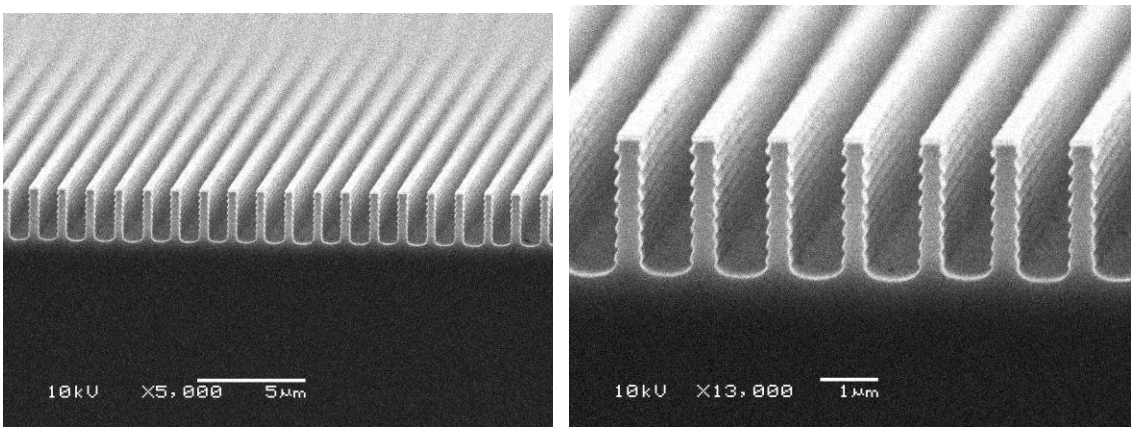

Figure 4:7 SEM images of fabricated external Si gratings

The etched gratings were than cleaned using a so called piranha solution, which is an acidic mixture of concentrated sulfuric acid (H2SO4) with hydrogen peroxide (H2O2). The processed wafer is immersed in this acidic mixture until all the organic molecules are removed from the Si surface.

The Si Littrow gratings without any coating on the top have a relatively low reflectivity. The reflectivity of the gratings were enhanced by coating the gratings with a material with high reflection ~ 980-nm. The material of choice for the coating is gold since it has a broad reflectivity spectrum and it provides more than 95% reflectivity around the wavelength of operation of the laser.

The high reflectivity thin metal film is deposited using DC magnetron sputtering deposition. For the normal DC sputtering, target (source) and substrate are placed on two parallel electrodes (diode) and placed inside a chamber filled with inert gas (Ar). The DC voltage (~kV) is applied to the diode, and free electrons in the chamber are accelerated by the e-field. These energetic free electrons inelastically collide with Ar atoms and plasma is formed with discharged gas. Atoms locked out from the target transport to the substrate.

The adhesion of the gold thin film layer on the Si substrate depends strongly on the cleanliness of the substrate. In order to obtain a good adhesion quality, the samples are immediately carried into the sputter chamber after the PIRANHA cleaning. The adhesion of gold onto silicon substrate is enhanced by depositing a very thin layer ~15-20 nm of chromium layer. Total thickness of the deposited gold layer is ~ 100nm. Figure 4.8 shows a scanning electron microscopy image of Cr/Au thin metal layer deposited on the top and sidewalls of the gratings. The thickness of the metal coating is slightly different than the top metal layer thickness, due to the geometry of the gratings and the coating method.

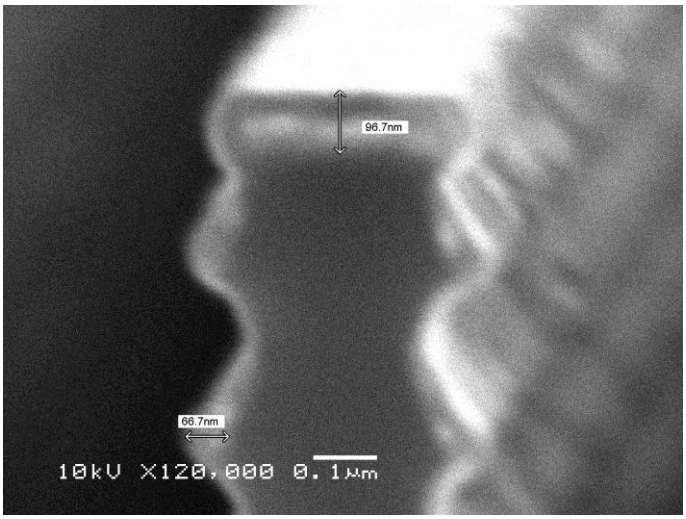

Figure 4:8 SEM image showing Cr/Au thin metal layer deposited on the top and sidewalls of the gratings

In this section we will also go over the preparation of the silicon die that were used during the 2D vertically stacked laser. Since the silicon substrate is also going to be a spacer element in between the GCSEL die in the vertical-stacking configuration, silicon substrates with very low resistivity is selected in order for good current conductivity. The silicon wafer were first treated in a buffered oxide etchant solution to remove the native oxide layer. The wafer were then put into the e-beam evaporator for depositing Al/Ti/Pt/Au only on the single side of the wafer. Since the silicon die were used in series electrical connection with the laser diode chips, Ohmic contacts on both sides of high-doped silicon wafer were fabricated to reduce a voltage drop through the spacers. The contacts were made with Aluminum deposition and rapid thermal annealing at high temperature in a nitrogen environment. The voltage-current characteristics measured through the silicon die with metallization on both sides demonstrated an Ohmic behavior with a total resistance of ~0.1 Ω. This resistance value is comparable with the series resistance of the laser diode bar. Fig. 4.8 shows the I-V characteristics of

the Si spacers after rapid thermal annealing (RTA) at different temperatures and Fig. 4.9 shows the change of resistivity of Si spacers by applied RTA temperatures.

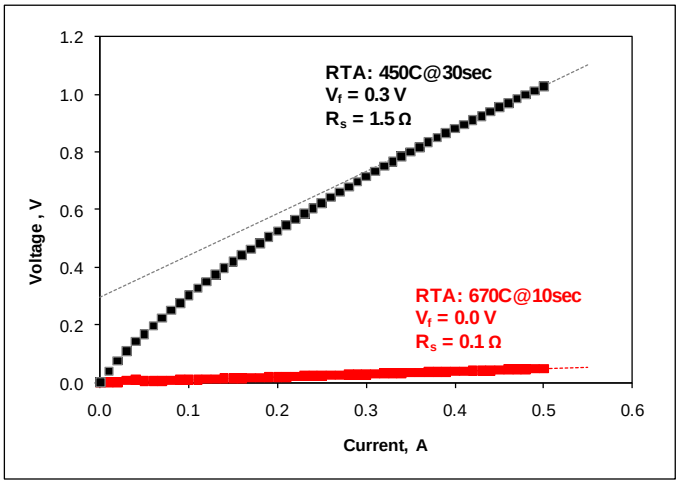

Figure 4:9 I-V characteristics of the Si spacer after RTA for different temperatures

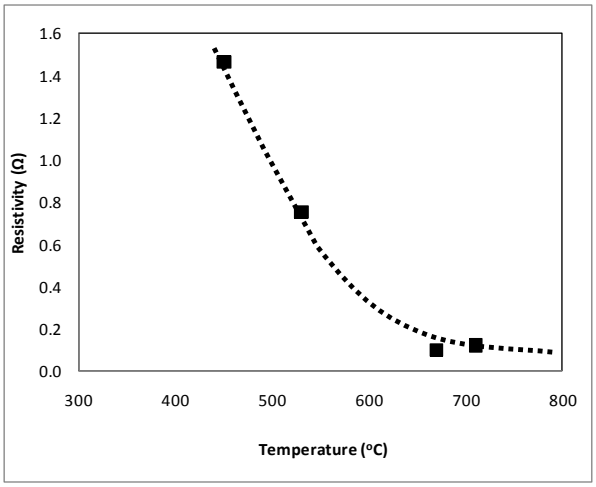

Figure 4:10 Si-die Resistivity vs. RTA Temperature.

4.3 Diffractive micro-optics fabrication using additive lithography technique

The micro-optics used to focus the beam into the nonlinear crystal is fabricated using lithography on a fused silica substrate. The lens system consists of a plano-convex lens and cylindrical convex lens. The multi-level diffractive lens equivalents of these

lenses were designed as explained in chapter 3. Additive lithography technique is used for the fabrication of these diffractive micro-optical lenses.

Additive lithography is one of the many methods for fabricating multi-level diffractive and refractive micro-optics [50,51]. This optical lithography technique is mainly based on the 2^N patterning technique which was developed at MIT Lincoln Laboratories for fabrication of multi-level diffractive optical elements [52]. Additive lithography technique uses the same number of amplitude masks during fabrication but it does not need multiple developing and etching steps compared to the 2^N patterning etch technique. Exposure dose control is employed with multiple binary mask patterns designed for multilevel (diffractive) optics. This technique is increases the throughput and decreases the cost of fabrication compared to other fabrication techniques.

Fabrication of multilevel structures on the photoresist is achieved by partial exposure of the photoresist. For eight-level structure, set of three amplitude mask patterns are needed for additive lithography technique. These mask patterns are used to pattern the photoresist, by employing exposure dose control for each mask. It is necessary to have the contrast curve of the photoresist being used for additive lithography. We have used SPR220-7 positive photoresist for the fabrication of the diffractive optics. Figure 4.11 shows the fraction of the photoresist developed after exposure with respect to the exposure time for SPR220 photoresist on fused silica substrate.

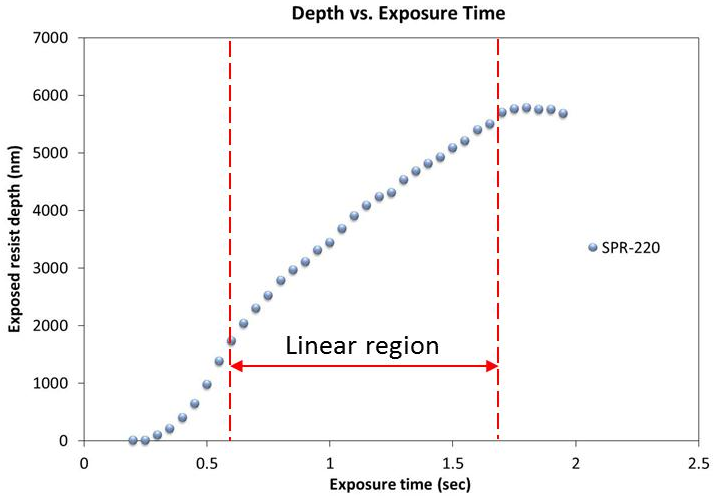

Figure 4:11 Contrast curve of SPR-220 on fused silica substrate (exposure at G-line 436nm)

There is mainly three regions in this curve: (1) a slow response region below threshold energy, (2) a fast rising region, and (3) saturation region, where the photoresist is completely bleached.

The second region is used for additive lithography. The SPR-220 is a thick photoresist, and due to absorption and resulting change in the propagation characteristics for the bulk medium cause the response to be nonlinear. This is the reason behind the second region being not perfectly linear for SPR-220. Thinner resists have a linear dependence in the second region of the exposure dose curve. Due the thickness of the designed lenses, and the selectivity of the etch process SPR-220 is used for the diffractive micro optics fabricated for this work. The projection lithography (stepper) is employed for the fabrication of the diffractive optics using additive lithography. In GCA-6300 g-line (436nm) stepper the exposure times are controlled by the shutter in the stepper tool (see Appendix). The advantage of the stepper tool over the contact lithography tool is the automatic alignment of the masks for each exposure. Also for stepper, all the masking

patterns can be laid out on a single mask and the apertures of are programmed to open to expose the each pattern on the mask.

Bias exposure is used to reach to the linear region of the photoresist response curve. The maximum height of each level and the possible number of levels are determined from the range of the linearity. The linearity is strongly dependent on the exposure energy and on process parameters such as soft-bake time and temperature, all of which need to be optimized for the resist and the substrate used in the process [53].

We exposed the wafer with each mask, doubling the number of levels at each exposure, similar to the standard 2N processing for binary diffractive optics. After the third exposure, eight levels were created, with depths that depended on the exposure time. This process is illustrated in Fig. 4.12.

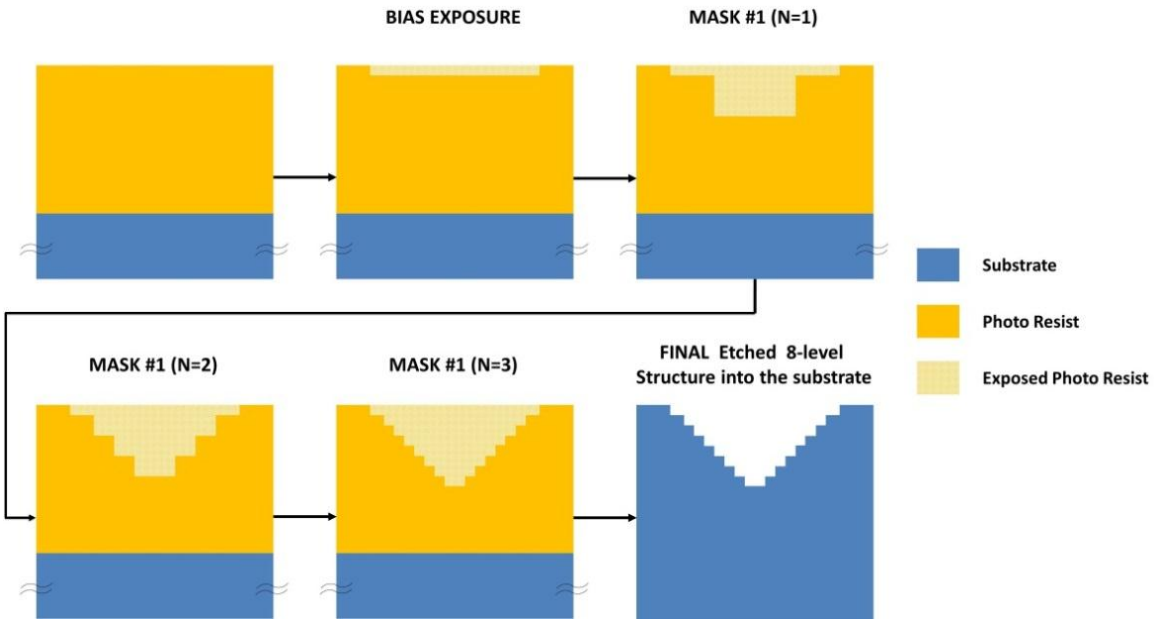

Figure 4:12 Additive lithography process using entire domain masking

A Matlab code was used to create the phase function of the lens and to convert this phase function into three different amplitude masks for 8-level diffractive optical element. The generated mask patterns are shown in Figure 4.13. For the aspheric lenses only first quadrant is shown (the mask has circular symmetry) and half section of the masks for cylindrical lenses are shown. Once the mask was complete, the process of fabricating the multilevel DOE required coating a substrate with resist and exposing the resist for biasing on a GCA stepper. Next, all three mask levels were exposed successively. Finally, the resist was developed.

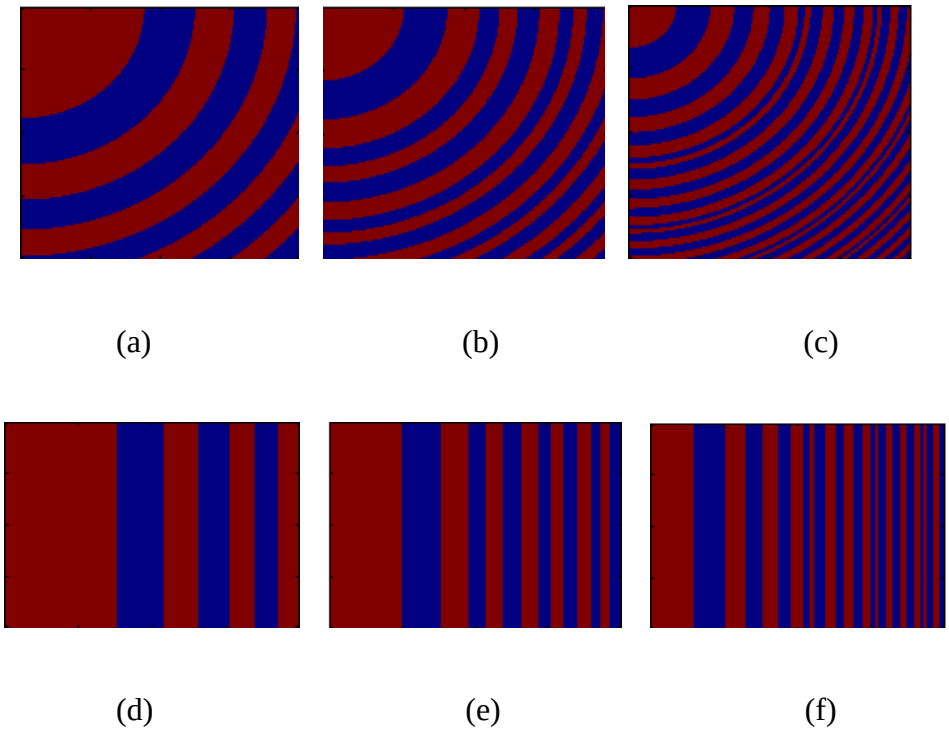

Figure 4:13 Images showing the mask files used in 8-level diffractive lenses.

The exposure times for each pattern are obtained by choice of each level height. If the height of each level needs to be h, then the depth needed for an eight-level DOE is 4h

after exposure of the first pattern, 2h for the second pattern, and h for the last pattern [49]. SPR220 resist does not have a perfectly linear region, therefore the exposure times are adjusted during fabrication to achieve equal level heights. The initial exposure times were calculated by fitting a linear function to the fabrication region. The bias (threshold) exposure time is t^{th} the depth of exposed resist for a bias exposure is h^{th}. If the exposure time for a depth of 4h+h is't' then for 4h depth the exposure time is t- t^{th} , for the first mask. The second mask is for creating 2h height in the resist. half of the exposure time of the first mask exposure time. The third mask is for the level heights of h, and the exposure time is the quarter of the time of the first mask exposure time. The proper bias exposure is crucial to achieving the desired level heights. It has been experimentally determined that slight exposure optimizations are required in this region.

The designed diffractive lenses have ~610 nm level heights. The substrate for the diffractive optical elements is fused-silica. Unaxis Versaline Inductively-Coupled Plasma (ICP) oxide etcher is used to etch the developed resist pattern into the substrate with ~ 1: 1.1 etch selectivity between the photoresist and the substrate. The developed resist heights were ~ 550nm, with the etch selectivity, the fabricated level heights were ~ 600 nm, which corresponds to a 4-π phase structure at 975 nm .Figure 4.14 shows the Zygo interferometer characterization of the diffractive optical lens array on the resist after development of the exposed resist.

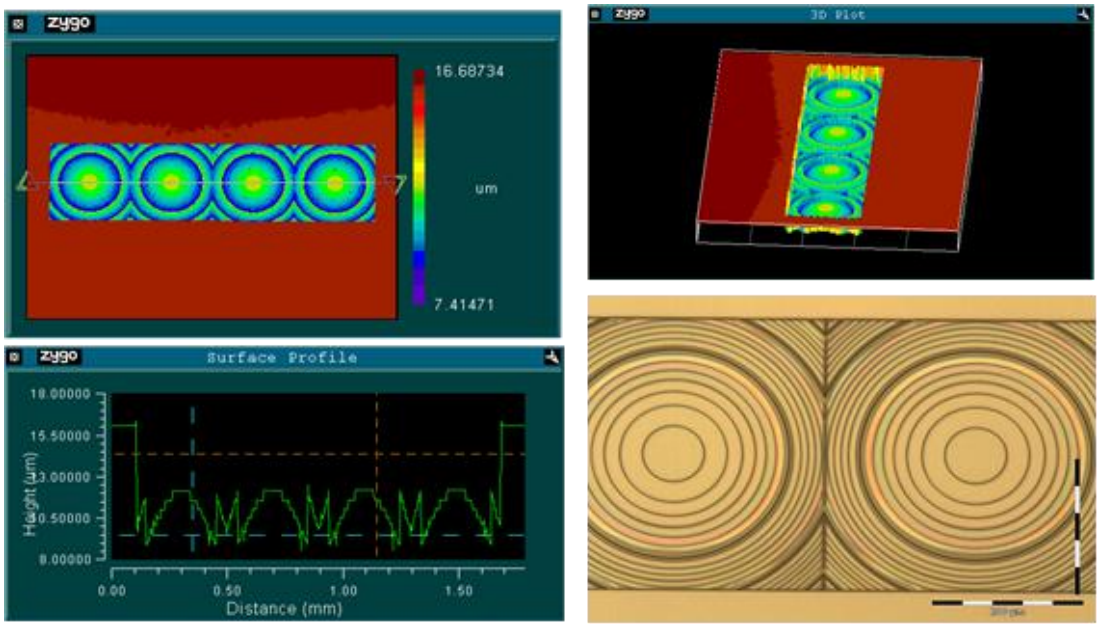

Figure 4:14 4X1 ,400um diameter lens array (a) The top view of the lens array taken by Zygo, (b) The cross section profile of the lens array, (c) 3D Plot of the lens array (d) microscope image of a part of the focusing lens array.

4.5 Conclusion

The fabrication processes for the GCSEL laser device, external Littrow grating, integration of the gratings on the GCSEL devices, and the diffractive optical elements were summarized in this chapter. Qualitative characteristics of the fabricated external gratings, diffractive optical lenses are also explained.

CHAPTER 5: EXPERIMENTAL RESULTS

In this chapter, the performance of the fabricated devices was tested. The laser device performance measurements were done under pulse pumping conditions. The devices were flip-chip bonded p-side down on aluminum nitride submounts. The submounts are then mounted on a thermo-electric cooler (TEC) with water cooled heat sink unit. The spectral characteristics of the devices were captured using an optical spectrum analyzer (OSA). Other measurements such as focal spot size of the fundamental beam after the beam shaping optical elements are also measured. The specifics of these measurements will be explained as the data is explained.

As mentioned in the research overview the first research effort was the performance of the dual grating external cavity surface emitting laser (DGECSEL). Second the performance of the DGECSEL devices as a fundamental source for blue light generation through second harmonic nonlinear conversion. Third effort was use of GCSEL-DGR based monolithic lasers for blue light generation. Fourth goal was amplifying the GCSEL-DGR using a grating –coupled semiconductor optical amplifier in MOPA configuration and application this source for blue light generation. The fifth effort was the demonstration of the multi-wavelength blue light source based on GCSEL-DGR devices. In this step GCSEL-DGR with different emission wavelengths were stacked vertically and the light output from individual emitters were focused into the nonlinear crystal using custom designed and fabricated micro optics beam shaper.

The sixth effort was testing the performance of the multi-wavelength 1-D DGECSEL array and blue light generation using this array. The seventh and the last effort was testing the efficacy of the DGECSEL concept by fabricating a 2-D vertically stacked multi-wavelength device. The results of all these work is covered in the following pages of this chapter

The light-current characteristics of the devices are measured by taking the average optical power using different types of detectors depending on the power level. For QCW 500-ns pumping ,an Ophir 20C-SH thermal detector and an Ophir photodiode sensor PD-IR. For 30-ns pulse pumping the average fundamental optical power is measured using PD-IR and the average power of the second harmonic optical power is measured using an Ophir photodiode sensor PD-UV.

At QCW pumping, the peak current is delivered by a Directed Energy PCX-7410 current driver. At this pulse pumping conditions, the peak power is calculated using the average power. For 500-ns pumping the pulse width of the electrical pulse and optical pulse are assumed to be same; this is true for electrical pulse widths longer than carrier lifetime. At 30-ns pumping, the pulse shape is not rectangular. Figure 5.1 shows an example of a fundamental optical pulse e that is measured by a high-speed detector. The pulse width is calculated by the area under the pulse divided by the peak value of the pulse amplitude; this gives us the effective pulse width information. This is critical in terms of accurate calculation of the fundamental peak power. The laser devices both GCSEL/DGR and DGECSEL were used in blue light generation through nonlinear second harmonic frequency conversion. The fundamental light sources were pulsed at 30-ns , the high peak power for the second harmonic blue light is also calculated by finding

the effective second harmonic light pulse width. The peak power is calculated from the average power using

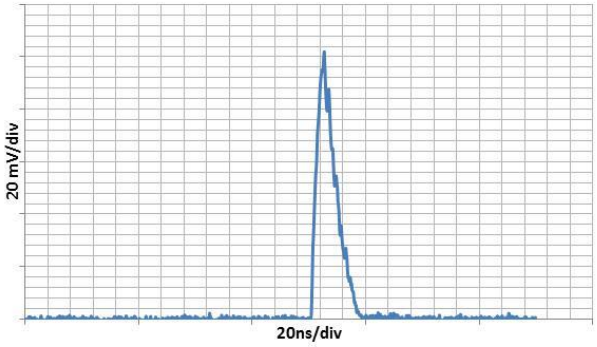

Figure 5:1 fundamental optical pulse shape

$$P_p = \frac{P_{avg}}{\tau_{eff}.f}$$

where P_p,P_{avg}, τ_{eff}, and f are peak power, average power, effective pulse width and pulse frequency, respectively. From the measured L-I curve the threshold current is calculated from the slope of the lasing curve and its cross-point from the current axis. This slope is also known as characteristic slope and has units W/A.

Another fundamental measurement for characterization of laser devices is the spectral output. The spectral content of the fabricated lasers were measured using an HP86142B OSA with a 0.06 nm spectral resolution. A multi-mode fiber is used to couple the light from the laser device into the OSA. The facet of the multi-mode fiber is aligned such that the light output from the devices has a normal incidence. The spectral information of the second harmonic blue light was measured using an Avantes Avaspec2048-UV fiber coupled spectrometer.

The near-field of the laser devices, and the focused spot-size of the lasers after the beam shaping optics is measured using a CCD camera and processed using Spiricon software. The near-field measurements are taken by aligning the laser light output such that the incidence is normal on the camera. Depending on the intensity of the light neutral density filters were used to eliminate the saturation of the CCD array. The focused spot size is measured by imaging a screen with scale markings along the beam propagation direction. Several points before and after the focal spot is measured to calculate the spot size.

5.1 Single Wavelength DGECSEL device

The performance of a GCSEL device with 2 mm active cavity length and 200μm stripe width (see Figure 5.2) is tested first without any external feedback element. The device is tested at 500-ns QCW at 20 °C. The LI-curve for the GCSEL device is shown in figure 5.3. The threshold current for the GCSEL device is ~500 mA. The specific GCSEL device has a slope efficiency of ~0.87 W/A.

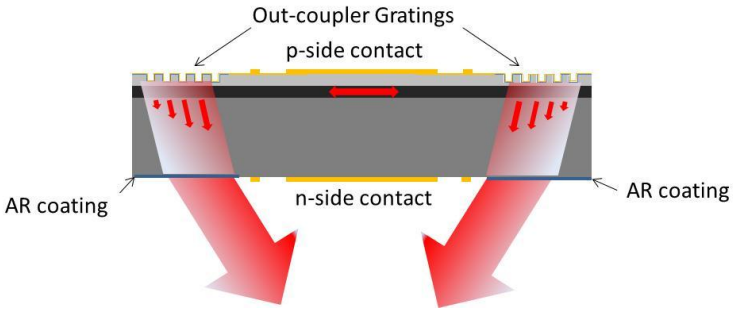

Figure 5:2 Schmetics of a GCSEL device

Next the external grating is positioned parallel to GCSEL device (see Figure 5.4). The grating is positioned in front of one of the emission facet of the GCSEL device. The grating is hold by a 5-axis stage during the positioning: 3-axis for x-y-z axis, one axis for

the pitch and the other for the yaw. After the grating is positioned parallel to the facet of the GCSEL, the distance between the grating and the GCSEL is adjusted for the maximum output from the other output facet of the GCSEL device This distances < 0.5 mm. Figure 5.3 shows the LI curve for the external cavity GCSEL device. The device has a ~ 610 mA threshold and has slope efficiency is ~ 0.8 W/A. This value is very close to the slope efficiency of the GCSEL device from both outputs. The decrease is mainly due to the external grating efficiency and the coupling losses of the reflected light back into the active medium. The device performance from a similar type of device with DGR configuration has slope efficiency slightly better than the DGECSEL configuration.

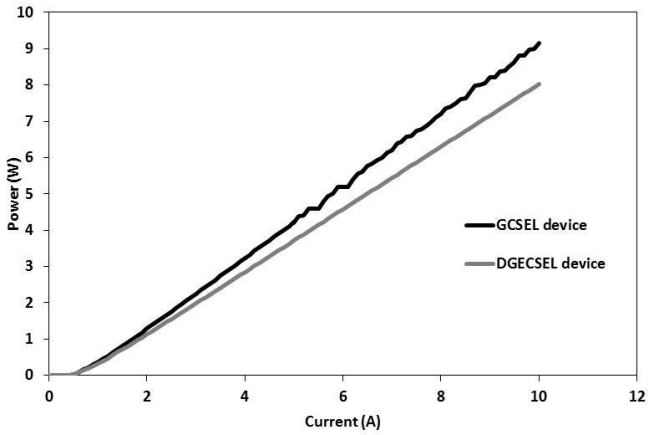

Figure 5:3 Comparison of GCSEL total power and a DGECSEL type device under 500-ns pumping

The change of the total output power as a function of the distance between the external grating and the GCSEL facet is measured. The external cavity had an optimum performance when the external grating and the facet separation was less than 0.5mm. The LI curve of this external cavity for separation lengths of 1mm, 1.5mm and 2 mm is also measured to understand the performance loss. Figure 5.4 shows the LI curves for the

external cavity GCSEL device for different distance between the GCSEL facet and the external grating.

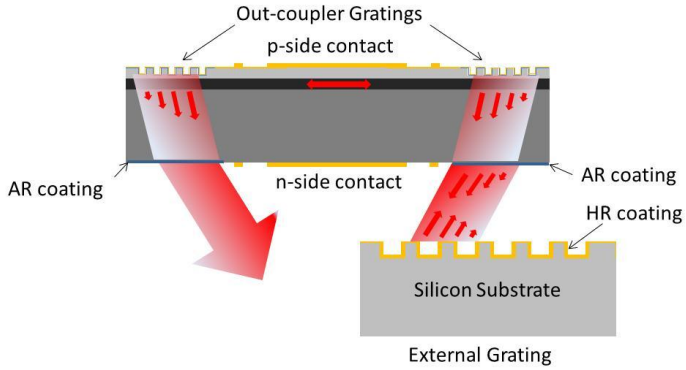

Figure 5:4 Schematic of a DGECSEL type device

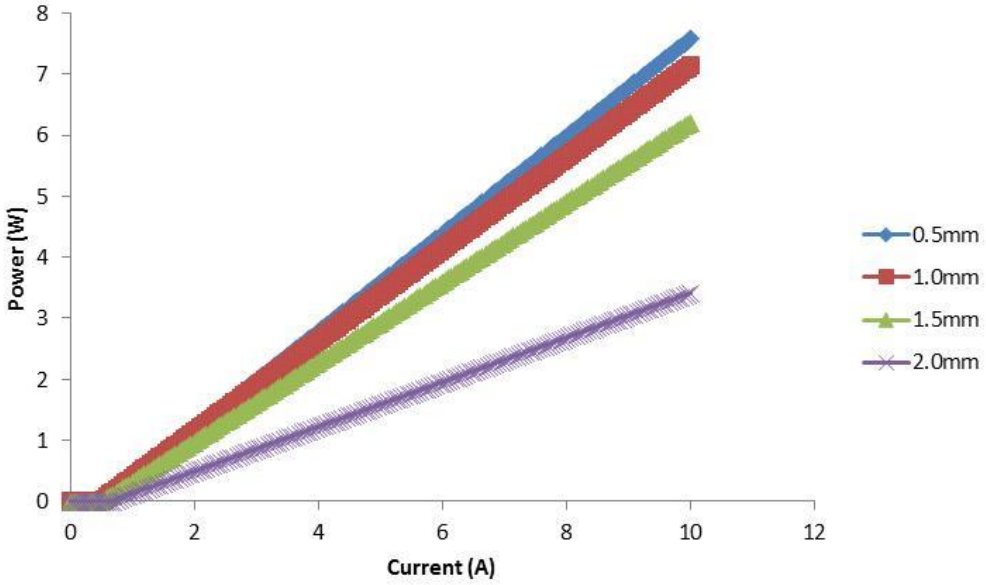

Figure 5:5 LI curves for a DGECSEL device with varied external grating distance to GCSEL device

The slope efficiency of the external cavity stabilized GCSEL drops with increasing the separation between the external grating and the GCSEL device. The cavity efficiency is severely affected for separations larger than 1.5 mm. This drop in the slope efficiency is mainly due to the limited size of the grating and the retro coupling loss back into the active medium. Figure 5.5 shows the slope efficiency decrease as the grating distance is varied.

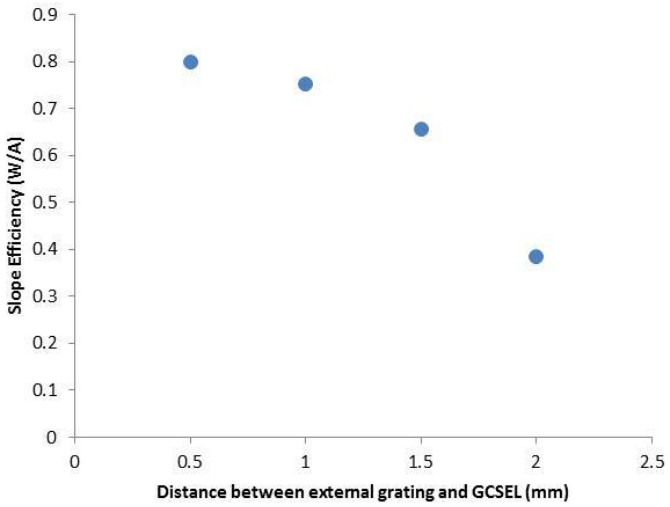

Figure 5:6 Slope efficiency of a DGCSEL device as function of external grating distance

The spectrum of this external cavity is also measured. The spectral linewidth at I = 20xIth was ~ 0.3nm at FWHM. The side mode suppression ratio was around ~39 dB. Figure 5.6 shows the emission spectra and the inset shows the linewidth of the emission at FWHM.

The near field (zoomed in) images from both GCSEL output facets are also taken to ensure the uniform emission profile. Figure 5.7 shows the near field images of the facets. As seen from these images both facets have very similar intensity distribution.

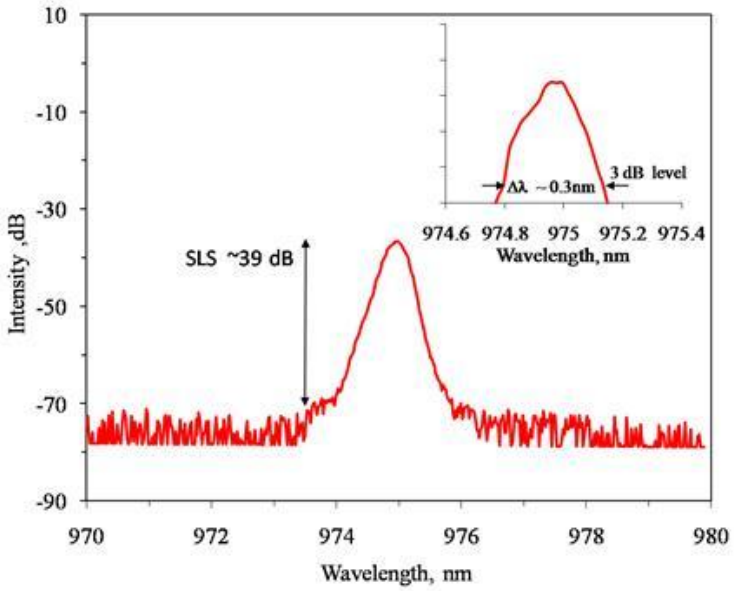

Figure 5:7Spectrum of the DGCSEL device

The ideal grating and the fabricated grating have a structural difference due to the fabrication process. The effect of BOSCH process' characteristic sidewall scalloping on the grating reflectivity strength is also explored. For this purpose, the scanning electron microscope images of the cross section of the fabricated gratings were transferred into a refractive index matrix using an image processing script written in Matlab, shown in Figure 5.8.

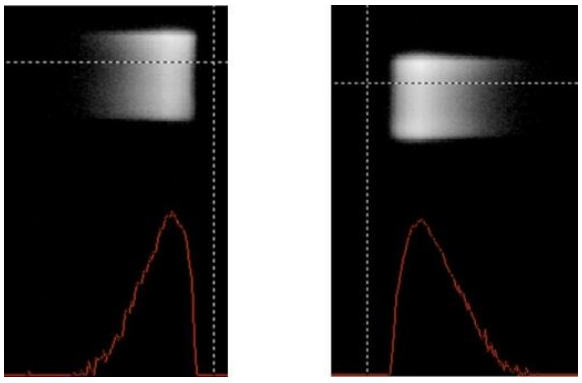

Figure 5:8 Field intensity at both facets of the GCSEL device

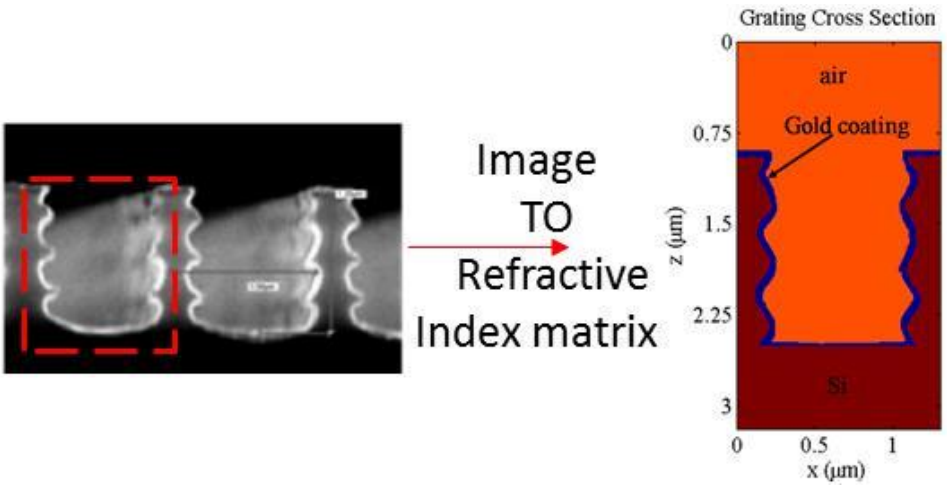

Figure 5:9 Converting the SEM image of the external grating to refractive index matrix in Matlab for FDFD simulation

The grating reflected power is calculated in FDFD at different steps by filling the air between the grating teeth all the way to the grating top surface. Figure 5.9 shows the comparison of the ideal grating and the fabricated grating calculated reflection efficiency as a function of the grating depth. As can be seen from the plot, the scalloping does reduce the total reflected power by ~ 10%. Still this does not severely affect the overall device performance.

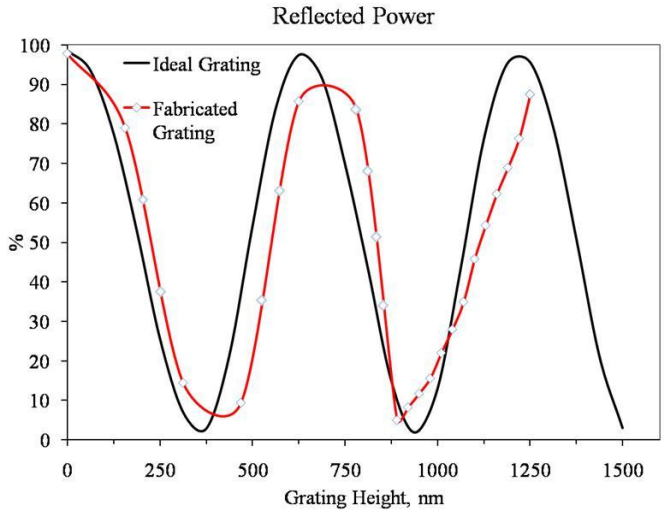

Figure 5:10 Comparison of the ideal grating efficiency vs. fabricated grating with scallops

5.2 Blue light source based on single wavelength DGECSEL

The DGECSEL concept is applied to generate a blue light via QPM based SHG. The same GCSEL device described in section 5.1 is used for the experiments. The aim this experiment is to achieve maximum nonlinear conversion efficiency and high peak power blue light.

For this purpose the GCSEL device is driven at 30-ns electrical pulses using an OEM high current 30-ns pulse driver. 10 mm long 5% MgO:PPLN crystal is used as the nonlinear medium for the QPM-SHG. This crystal has multi-channels with different poling periods. The grating periods of 5.26um and 5.28um are chosen since at these poling periods a fundamental light source lasing around ~975 nm can be efficiently converted to its second harmonic close to the room temperature. The crystal temperature is continuously monitored and controlled to tune its temperature for reaching maximum achievable second harmonic nonlinear conversion efficiency.

The fundamental light from the DGECSEL output coupler is focused inside the crystal by cylindrical lens and objective lens pair. Figure 5.11 (a) shows the far-field image of the fundamental beam and its intensity profile. Figure 5.11 (b) shows the focused spot-size after the cylindrical and the objective lens. The focused spot size has a beam diameter of ~140μm x150 μm at FWHM.

The converted second harmonic blue light and the unused fundamental light is collimated with another lens and an IR laser line filter is used to filter out the fundamental near-IR light (see Figure 5.12).

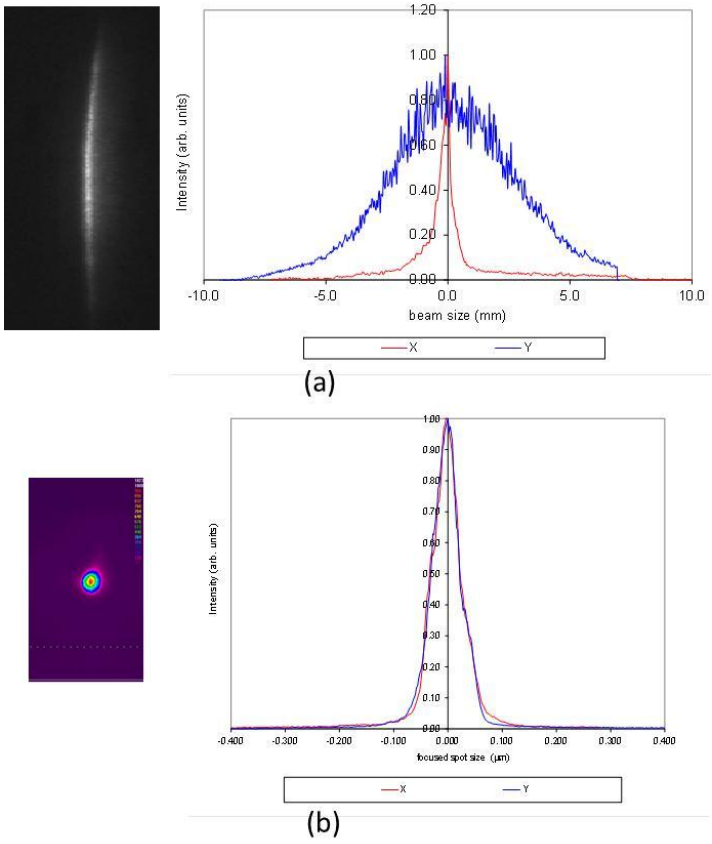

Figure 5:11 (a) Far-field intensity image and profile of the DGCESEL output , (b) focused spot image after the cylindrical and objective lens pair

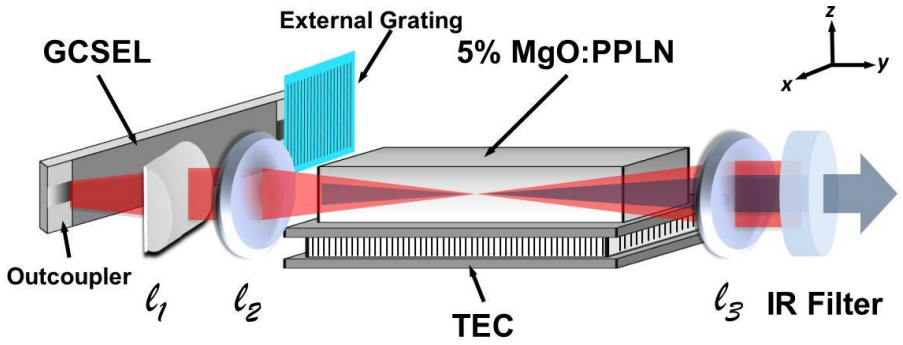

Figure 5:12 SHG setup using DGECSEL [53]

Figure 5.13 shows the SH peak power as a function of fundamental power for the DGECSEL device under 30-ns electrical pumping. The device has a maximum peak power of ~ 28 W at ~60 A peak current. The peak power is calculated from the measured from optical pulse and the average power, as explained at the beginning of this chapter.

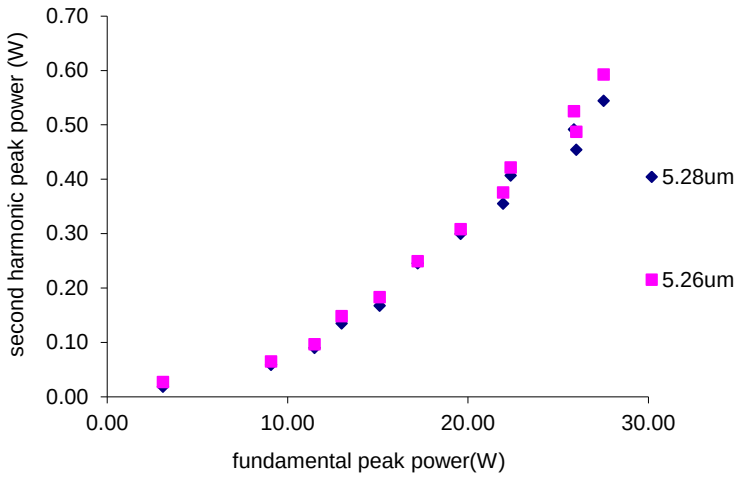

Figure 5:13Second harmonic peak power vs. fundamental peak power

Second harmonic power is measured for two different PPLN periods 5.28μm and 5.26μm. The crystal temperature is tuned to ~19.2 °C , and 29.4°C for 5.28μm and 5.26μm, respectively for maximum second harmonic conversion efficiency. The SH peak

power for both channels were around ~0.6 W which corresponds to a conversion efficiency of ~10^{-3} W^{-1} ($\eta = P_{2\omega}/P^2_{\omega}$ W^{-1}). The spectrum of the second harmonic blue light is shown in Figure 5.14. The spectral bandwidth of the blue light is ~0.21 nm at ~487.5 nm.

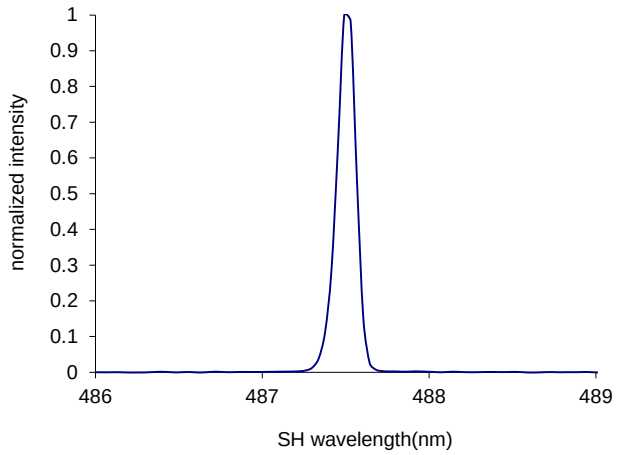

Figure 5:14 Spectrum of the second harmonic blue light

The second harmonic power as a function of the crystal temperature for the 5.28μm PPLN is also measured. The temperature bandwidth of the SH peak power is ~4.0°C at FWHM. (see figure 5.15).

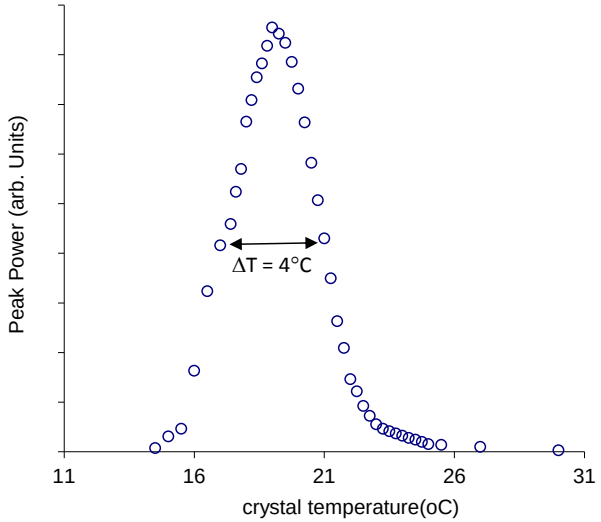

Figure 5:15 Temperature dependence of the SH peak power

5.3 Single Wavelength GCSEL-DGR based blue light source

GCSEL/DGR type monolithic laser is also applied for blue light generation via second harmonic nonlinear conversion process. The device is tested under 30-ns pumping condition, which is the same condition with the DGECSEL type device. GCSEL/DGR has a 4mm long active section with a 100-μm stripe width. A cylindrical lens was used to collimate the highly diverging axis and a high NA objective lens is used to focus the collimated beam into the crystal. During the experiments we used PPKTP and PPLN type crystals, crystal temperature is stabilized using a thermo electric cooler (TEC). The converted blue light and unused IR light is collimated using an aspherical lens and a laser line filter is utilized to filter out the IR light and pass only the blue light. A UV detector is placed after the filter to measure the blue light average power. The optical pulse is measured by focusing the blue light into a fiber optics which is connected to a high speed photo-detector which than connects to oscilloscope. Figure 5.16 shows the SHG setup.

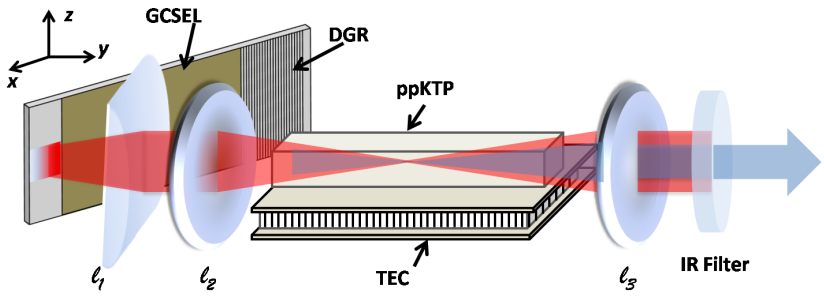

Figure 5:16 Schematic of the SHG setup with a GCSEL/DGR device[54]

The performance test of the device shown a threshold current density of 130 A cm and slopes of 0.53 W/A in continuous wave (CW), and 0.71 W/A under a 500-ns pulse pump. The IR laser diode was also tested with a commercially available pulse driver providing high peak current pulses with duration of 30 ns and repetition rate of 1 kHz. Low duty cycle pumping allowed to eliminate any thermal effects and maximize output peak power at high current. In this case, the optical peak power was determined by analyzing the temporal shape of the optical pulse measured with a high-speed detector and a scope. Light–current characteristics measured with the 30 ns driver were well matched with those obtained at low current during the performance test. The maximum achievable optical peak power from the device was over 30 W at a peak current of 100 A. The lasing at room temperature was a single line with central wavelength of 973.5 nm and full-width at half-maximum (FWHM) bandwidth of 0.3 nm (see figure 5.17-top).

The focused spot radii were measured to be 110 μm x 140 μm $1/e^2$ level in the longitudinal and lateral axes, respectively. The ppKTP crystal was fabricated by Raicol Crystals Ltd., and designed for the fundamental wavelength of 975 nm at room

temperature. The crystal's dimensions were 1 mm 2 mm 10 mm; the facets were antireflection (AR) coated for 975 nm/487 nm.

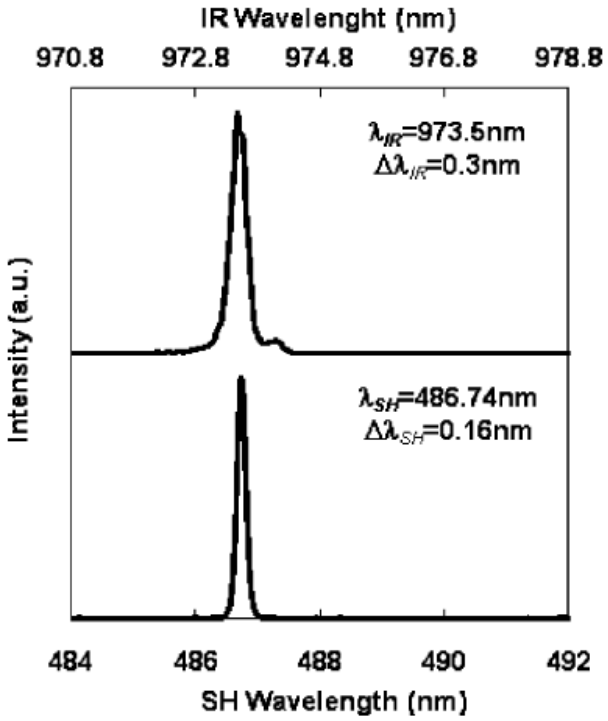

Figure 5:17 Spectra for the fundamental and second harmonic light

Figure 5-17 (bottom) presents an optical spectrum of the second harmonic light, which was a single line with FWHM bandwidth of 0.16 nm. The spectral measurement was made at the crystal temperature corresponding to the SHG maximum. The SH peak power variation as a function of the PPKTP temperature (Fig. 5-18) demonstrated the SHG maximum at 19 °C with FWHM of 5.9 °C.

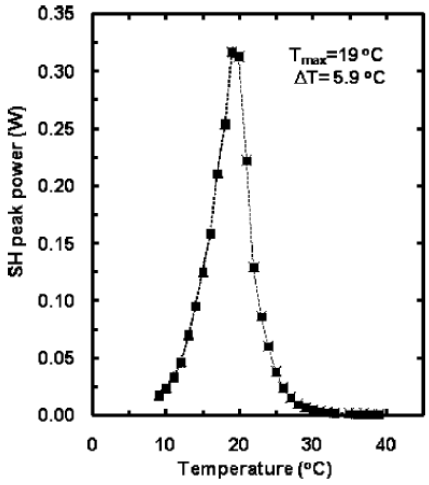

Figure 5:18 Temperature bandwidth of the SH conversion

Fig. 5-19 represents the SH peak power as a function of fundamental peak power along with the fitted quadratic curve that corresponded to the normalized conversion efficiency of 0.6×10^{-3} W^{-1}. A maximum SH peak power of 0.66 W was achieved at the pump power of 33.5 W.

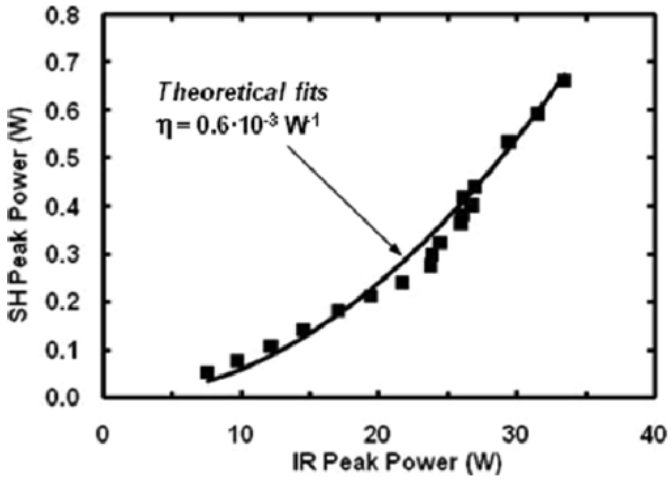

Figure 5:19 Second harmonic peak power vs. fundamental IR peak power

5.4 Single Wavelength MOPA based blue light source

The conversion efficiency of the single pass SHG from the MOPA is evaluated using the experimental setup presented in Fig.5-20. A low numerical aperture (NA) cylindrical collimating (l_1) and focusing (l_2) lenses were both applied to maximize the optical density of the IR output light inside the non-linear crystal.. We used a conventional thermoelectric cooler (TEC) for fine temperature control of the non-linear crystal. To filter the IR light a 488nm laser line filter with bandwidth of 10nm was used.

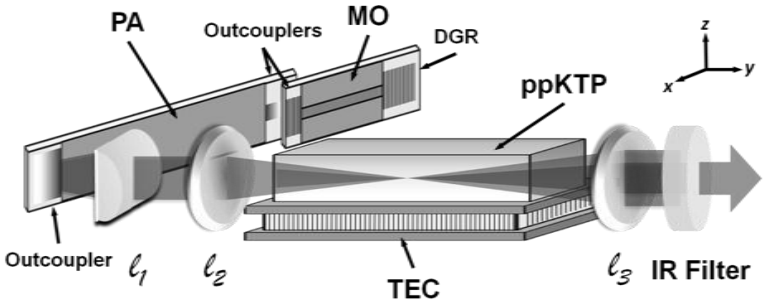

Figure 5:20 SHG setup with MOPA[55]

The broad area GCSEL/DGR single emitter consisted of a 4mm-long active section with a 100μm-wide stripe, a DGR section, and a 270nm-periodicity grating outcoupler with a high-reflection coating on the p-side. The device design description and fabrication details are described elsewhere [55]. The performance test of the device shown light-current slopes of 0.5 W/A in CW and 0.7 W/A under a 500nsec-pulse pump. The laser diode was also tested with a commercially available pulse driver providing high peak current pulses with duration of ~30nsec and repetition rate of 10 kHz. Low duty cycle pumping allowed one to eliminate any thermal effects and to maximize output peak power at high current.

The maximum achievable optical peak power from the GCSEL/DGR single emitter was 18 W at a peak current of 28 A. The single line lasing at room temperature was with central wavelength of 977.5 nm and FWHM bandwidth of 0.25 nm. For the MO, we used the same GCSEL/DGR chip as described previously. A device with a 4mm-long tapered active section and two integrated grating couplers was used as the PA. The p-side gratings of the MO output and of the PAs input were identical providing direct optical coupling between the devices. PA's input aperture was of 100 μm matching with the MO stripe and output width was 550 μm.

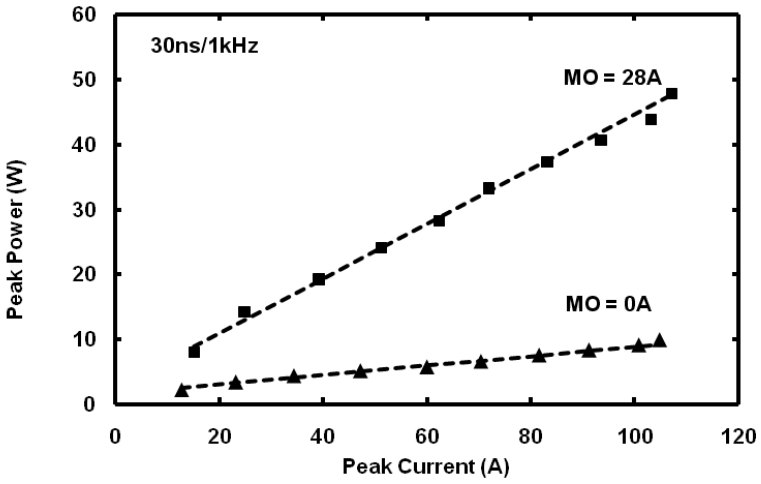

Figure 5:21MOPA characteristics: output peak power versus PA peak current under various MO pumping

The PA's grating outcoupler was fabricated with the same periodicity as the input grating. However the output grating grooves were curved matching with angle of the tapered stripe. The MO and the PA were wired to different current stand-offs to allow separate electrical pumping of the devices. For driving the MOPA components we used two similar 30nsec-pulsers from DEI but the PA driver allowed a peak current over 100

A at repetition rate of 1 kHz. Fig. 5-21 presents the MOPA output peak power versus PA peak current at different MO pumping level. The optical peak power of 45 W was obtained and it was limited by the maximum current of the pulser used for PA.

We noted from the MOPA spectrum that nearest satellite peak was raised with increasing the PA drive current. Such peak was also observed in the GCSEL/DGR spectrum but at significantly lower level. The satellite peak was spaced from main line by ~0.7 nm and it was caused by imperfection of AR coating on the MO output n-side resulted in formation of an additional Fabry–Pérot cavity in the 150μm-thick GaAs substrate. The fundamental light was focused down to a spot with radii of 140μm × 180μm.

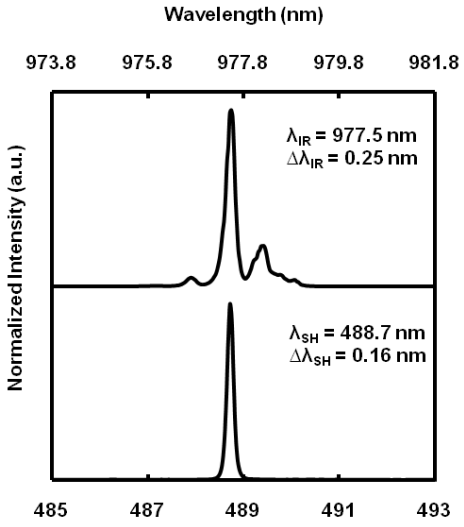

Figure 5:22 Fundamental and second harmonic light spectra

Fig. 5-22 (bottom) presents an optical spectrum of the SH light obtained from the MOPA assembly. A single line with central wavelength of 488.7 nm and FWHM

bandwidth of 0.16 nm was measured at the ppKTP crystal temperature corresponding to the SHG maximum.

In Fig. 5-23 (left), the SH peak power is depicted as a function of the ppKTP temperature demonstrating the SHG maximum at 68°C with FWHM of 14.5°C. The measured SH peak power vs. IR peak power is shown in Fig. 5-23 (right) . The maximum obtained blue power from GCSEL/DGR single emitter was 0.26 W at incident fundamental power of 32 W. The quadratic fit resulted in the normalized conversion efficiency of $\eta \approx 0.3 \cdot 10^{-3}\ W^{-1}$.

Low blue power from the MOPA was explained with an effective spectral broadening and a beam quality reducing caused by distortion of the MO seeding light while amplification in the tapered PA.

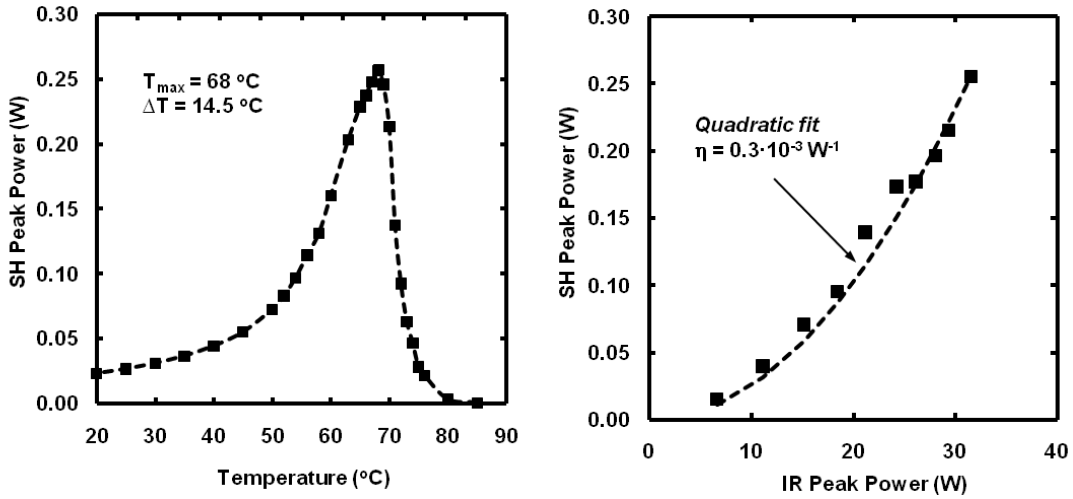

Figure 5:23 (left) Second harmonic peak power versus crystal temperature, (right) second harmonic peak power vs. fundamental IR peak power

5.5 Multi-Wavelength vertically stacked GCSEL-DGR array based blue light source

We have fabricated a 1D GCSEL/DGR array by vertically stacking the individual devices emitting at slightly different wavelengths. A multi-grating ppLN nonlinear crystal is used to convert each output fundamental signal into its second harmonic. Experimental results of frequency doubling the output of vertically stacked GCSEL/DGR devices with different emitting wavelengths. We used a multi-grating 5 % magnesium-oxide-doped periodically poled Lithium Niobate crystal as the nonlinear conversion medium. The individual emitter output is focused into each channel of the crystal by diffractive beam shaping optical element array to minimize the footprint area of the whole setup.

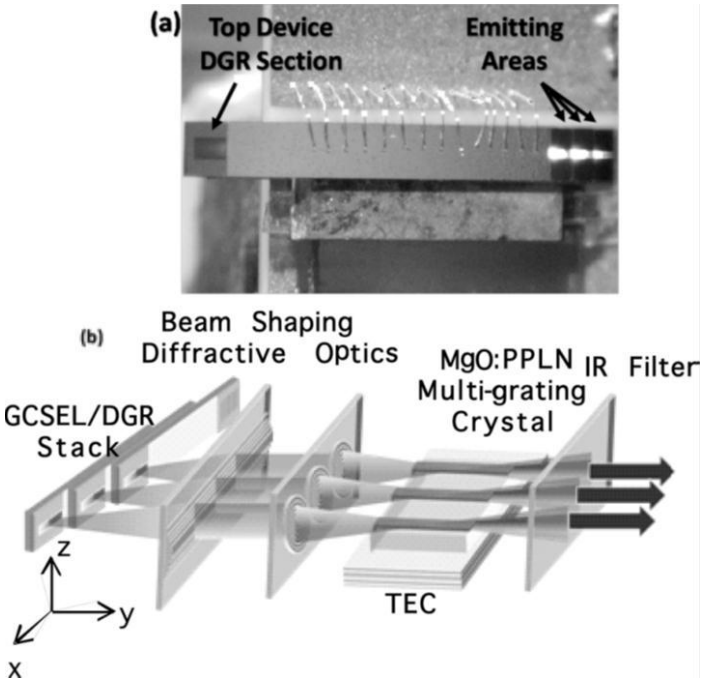

Figure 5:24 (a) 6-mm active area GCSEL/DGR stack under operation, (b) Schematics of GCSEL/DGR Laser Diode stack and SHG setup[58]

In our experiments, GCSEL/DGR single device chips that were stacked vertically. The vertical stack included three devices that were shifted in the plane of the longitudinal axis of the laser cavity in order not to block the surface emitting regions of the individual devices. The vertical GCSEL/DGR stack shown in Fig. 5-24 incorporated a 6-mm long active section with a 100-μm wide stripe, a DGR section, and a 270-nm periodicity grating out-coupler with a high-reflection coating on the p-side. The period of the n-side Littrow grating included in the DGR section of each individual GCSEL device were chosen to obtain lasing wavelengths of 976.9 nm,977.8 nm, and 978.6 nm at room temperature, these wavelengths were specified for the individual channel of the fabricated multi-grating 5% MgO:PPLN crystal.

The performance test of the vertical stack show an efficiency slope of 1.9 W/A in continuous wave, and 2.0 W/A under a 500-ns pulse pump. The vertical GCSEL/DGR stack was also tested with a pulse driver providing high peak current pulses with 30 ns pulse widths and repetition rate of 1 kHz. The light current characteristics measured with the ns pulse driver were well matched with those obtained at low current. The maximum achievable total optical peak power from the whole GCSEL/DGR stack was ~ 32.7 W at peak current of 22 A.

The lasing spectrum of the individual devices in the stack at 23.5 ^{o}C were 977.1 nm, 978.0 nm ,and 978.9 nm. The linewidth of the each individual device at full-width at half-maximum (FWHM) were 0.20 nm, 0.32 nm, and 0.26 nm respectively [Fig.5-25 (top)]. The emitting wavelength from the individual GCSEL/DGR devices needs to be within the acceptance bandwidth of the corresponding PPLN channel at an optimum crystal tempareture for an efficient SH conversion process.

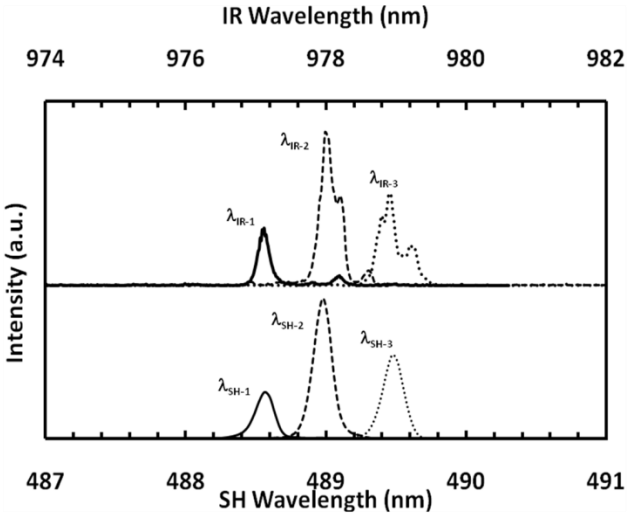

Figure 5:25 (Top) IR Spectra and (bottom) SH Spectra at 16 A pumping ns-current

The phase-matching wavelength vs. the temperature of the crystal was plotted for different poling periods in the crystal in Figure 5-26. The values for the temperature dependent refractive index were calculated from Sellmeier equations described elsewhere [43]. The emitted IR wavelengths from DGCSEL/DGR stack and the optimum IR wavelengths obtained from the calculations are relatively well matched at a specific crystal temperature.

The multi-wavelength blue light experimental setup shown in Fig.5-24b consists of vertically stacked GCSEL/DGR IR source, a cylindrical diffractive lens to collimate the output beams in the direction perpendicular to the diode-stripe and an aspheric diffractive lens array to focus the individual IR output into the matched channel inside the MgO: PPLN crystal. The cylindrical and aspheric 8-level diffractive lenses were designed using ZEMAX™ and fabricated on fused silica substrate by additive lithography as explained in the design and fabrication chapter.

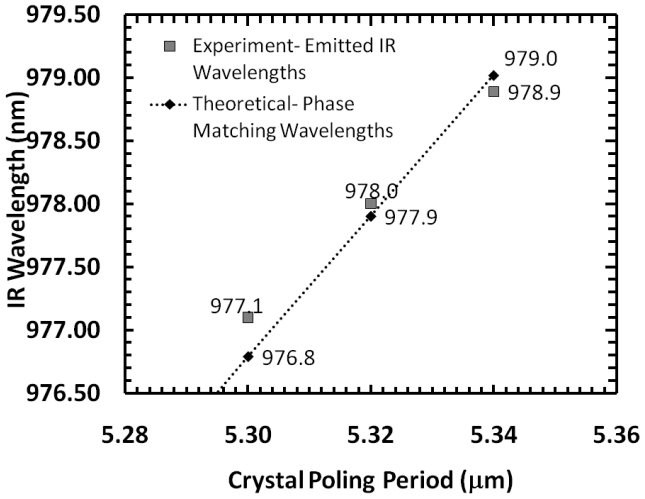

Figure 5:26 Plot showing the difference between the calculated phase matched wavelengths for the channels (5.30 um, 5. 32 um, and 5.34 um) in the crystal and emitted IR wavelengths from the GCSEL/DGR stack

The diameter of individual aspheric diffractive lens in the array is 400-μm. The period of the lens array is 400um which was determined by the GCSEL/DGR stack emitting area spacing. The focused spot diameter of a single emitter were measured to be 140 μm × 190 μm at $1/e^2$ level. The multi-grating MgO: PPLN crystal's dimensions were $0.5\times4.2\times5$ mm^3. Each channel in the crystal has a different poling period, and has a width of 300 μm. The spacing between each channel was 100 μm. The facets of the crystal were antireflection coated for 975 nm/ 487 nm. The temperature of the crystal was controlled using a thermoelectric cooler. A 488-nm laser line filter was used to filter the unconverted IR light from the blue light output. Figure 5-27 shows the collimated blue light outputs after the IR filter. The spectral intensities of the SH outputs are not equal due to the fact that the output power from the individual GCSEL devices are not equal. This variation in the intensity can also be related to the overall match of the temperature of the crystal and corresponding phase matching wavelengths for each different channel (See Fig. 5-25).

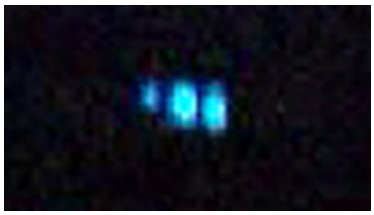

Figure 5:27 Collimated blue light outputs after the IR filter.

Each grating in the crystal were tested with a single GCSEL/DGR device to evaluate the conversion efficiencies, the individual channels all have the same conversion efficiencies. Therefore we can conclude that the variation in the intensities of the spectra of the SH wavelengths are mainly due to the different power levels emitting from the devices in the GCSEL/DGR stack.

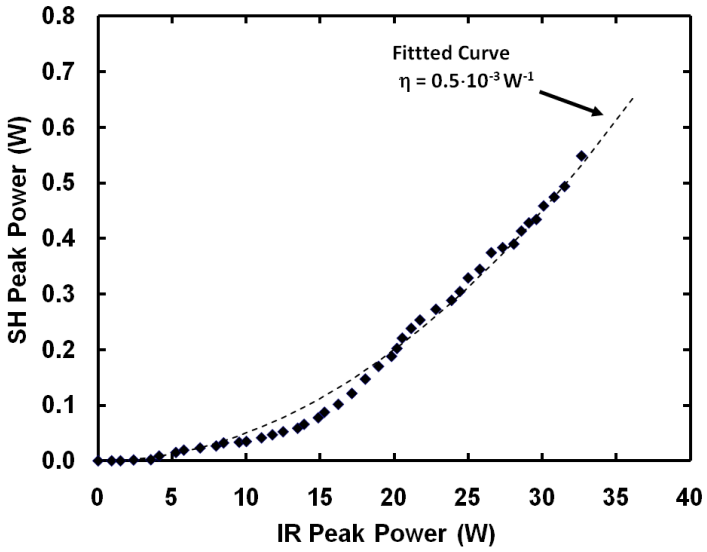

Figure 5:28 Total second harmonic peak power as a function of total fundamental peak power

Fig. 5.28 represents the total SH peak power as a function of total fundamental peak power along with the fitted quadratic curve that corresponded to the normalized conversion efficiency of 0.5×10^{-3} W^{-1}. A maximum of total SH peak power of 0.55 W

was achieved at the total pump power of 32.7 W. The GCSEL/DGR stack current pump was increased to higher levels to increase the fundamental power and as a result the SH peak power. Although SH peak power of around 1 W was obtained at fundamental power levels of 66 W, the fundamental and the second harmonic spectrum detoriate and several spectral satellite peaks appeared, which in turn resulted in the decrease of conversion efficiency.

5.6 2-D vertically stacked multi-wavelength external cavity GCSEL

In this chapter we summarized the experimental results of the multi-wavelength two-dimensional array based on vertically stacked grating coupled surface emitting laser bars. The emitters in the array were individually wavelength stabilized using external Littrow gratings fabricated on silicon-based spacers.In this integrated external cavity configuration the fabrication tolerances on the feedback grating are less stringent and the substrate material can be varied according to the desired application. Moreover, the process can easily be scaled to large arrays, with each individual emitter locked to the same wavelength or an arbitrary array of wavelengths defined by the period of the Littrow gratings for each element. The 1D GCSEL arrays are stacked in a vertical configuration with a wavelength selective element integrated into the spacer. In the current 2D-array design (see figure 5-29), the wavelength locking element used is a Littrow grating fabricated on external silicon die which is directly bonded on the GCSEL's n-side.

For experimental evaluation of the proposed concept, a 2x2 emitter array was fabricated and tested in pulse condition. For this purpose, we used bars of GCSELs. The individual GCSEL devices consisted of 2-mm long active sections with a 200-μm wide

stripe and two indentical 270nm-periodicity grating outcouplers processed on the p-side. These low reflectivity gratings make GCSELs a perfect gain media for external cavity control [56]. Figure 5-30 shows the assembed 2D array (left) and the device in operation (right).

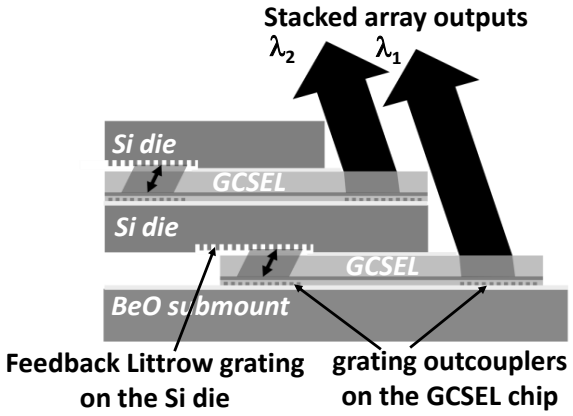

Figure 5:29 Cross-section schematic of the multi-wavelength 2D array based on vertical staking grating coupled emitter bars and Si dies with the processed Littrow gratings [57f].

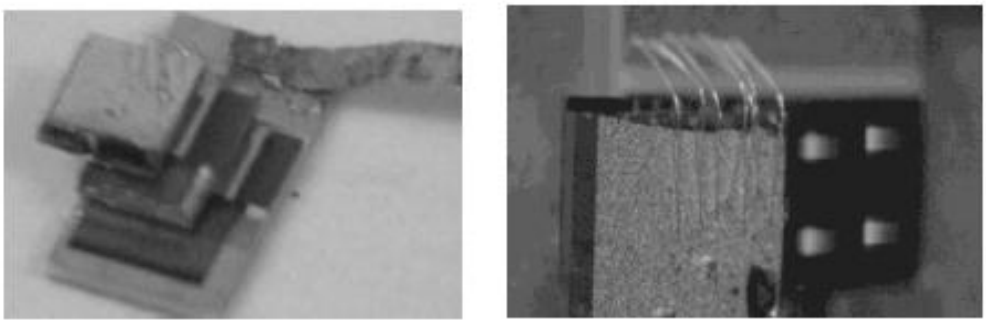

Figure 5:30 (left) Assembled 2D array device, (right) 2D Array device in operation

The periods of 1.30 µm and 1.31 µm were chosen for the gratings processed on each of the Si die that resulted in ~0.8 nm spacing between the bar's emission wavelengths for a n_{eff} value of ~3.24.

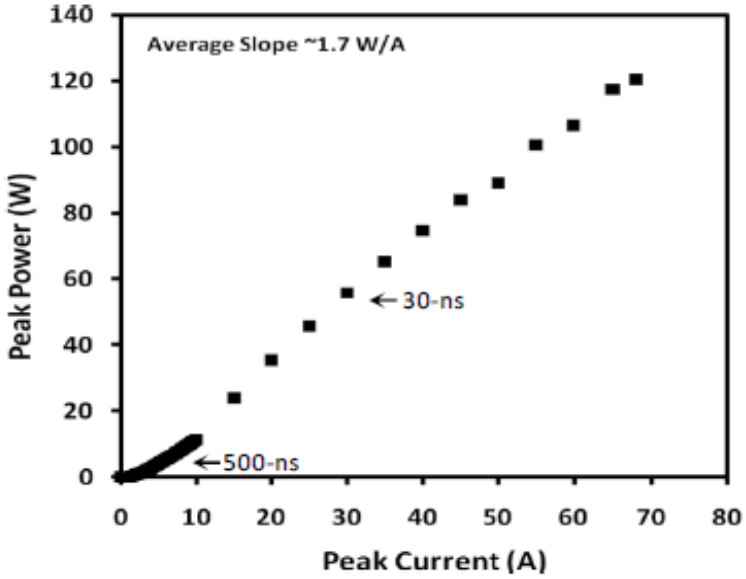

Figure 5:31 Light-current characteristics measured from (2x2) stack-array under 500-nsec (low current) and 30-nsec (high current) pumping conditions.

The completed 2D-emitter array was evaluated with a low duty cycle pulse driver to minimize thermal heating. The output optical power versus the input current was measured for all four emitters. Fig.5-31 shows the combined light-current characteristics for both 500-ns and 30-ns drivers, used for low- and high-peak current testing respectively. The measured data demonstrated a slope of 1.7 W/A which is twice that of a single wavelength locked GCSEL device.

A maximum peak power of ~120 W was observed for the 2D-emitter array at a peak current of 68 A, which was the limit of the 30-ns pulse-driver. The lasing spectral

characteristics presented in Fig. 5-32 were measured at pump currents near the peak current of 60A, corresponding to total output peak power of 110 W.

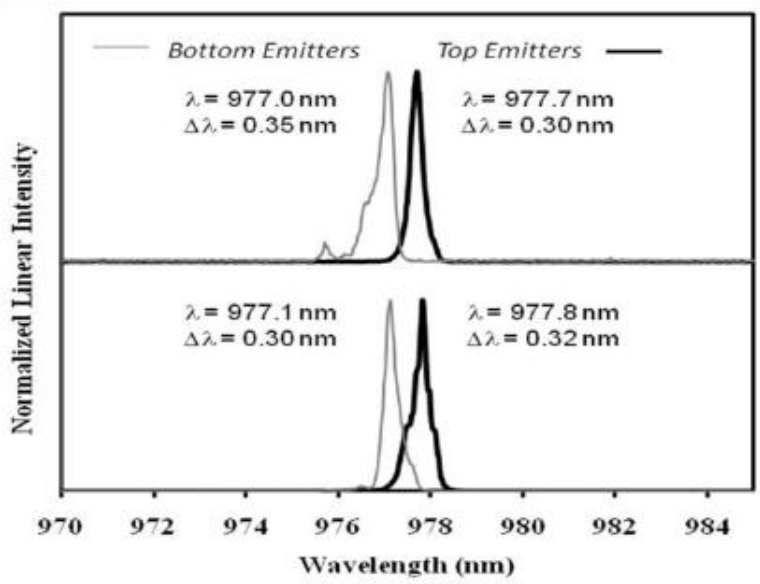

Figure 5:32 Spectrum samples from individual emitters of the (2x2) stack-array driven with 60 A peak current.

The emitted wavelengths from the emitters correlated with the expected wavelengths designed into the Littrow gratings at~ 977.0-nm for the bottom bar and 977.8-nm for top bar. The variations of the lasing lines from the individual emitters were inside the ~0.3-nm spectral bandwidth measured at full-width at half-max.

5.7 Multi-wavelength blue light source based on 1-D DGECSEL array

We have fabricated a one dimensional DGECSEL array configuration. A GCSEL bar with total of 4 devices with 2mm active lengths and 200μm stripe widths are used during this experiment. The external Littrow gratings on the silicon die are positioned relative to the GCSEL spacing and have different periods(see Figure 5.33). The external Littrow grating periods of 1.29μm, 1.30μm , 1.31μm , and 1.32μm . This corresponds to a ~0.8 nm difference in emission wavelength between the neighboring emitters.

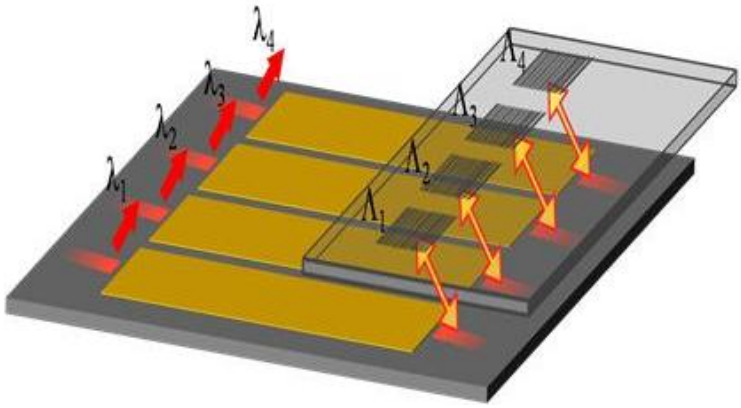

Figure 5:33 1D- Multi-wavelength DGECSEL array

The 1D-emitter array was evaluated with a low duty cycle pulse driver to minimize thermal heating. The output optical power versus the input current was measured for all four emitters. Fig.5.34 shows the combined light-current characteristics for both 500-ns and 30-ns drivers used for low- and high-peak current testing respectively. The measured data demonstrated a slope of 0.89 W/A which is comparable with GCSEL/DGR performance. A maximum peak power of ~64 W was observed for the 1D-emitter array at a peak current of 75 A, which was the limit of the 30-ns pulse-driver.

Figure 5.35 shows the spectra of the array. The emission wavelengths of 971.7 nm, 972.5 nm, 973.3 nm, and 974.0 nm were measured from the outputs of the emitters at a peak current of 50 A, at 30 ns, 1 kHz pumping condition. These values correlate with the external Littrow grating periods. The spectral bandwidths of the individual emitters were ~ 0.3 nm.

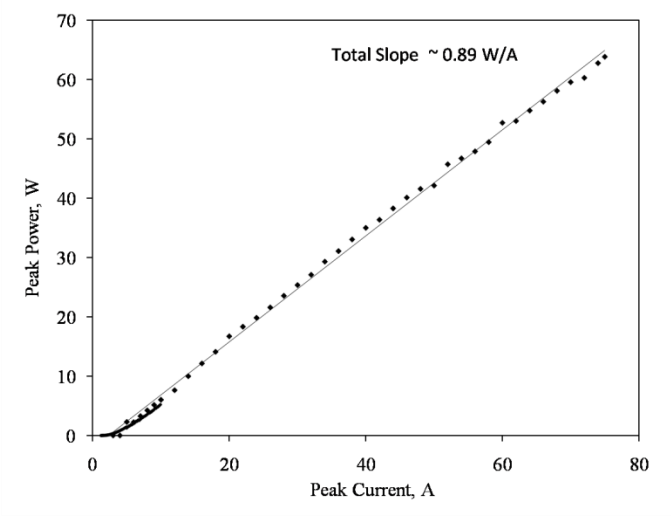

Figure 5:34 Total peak power of multi-wavelength 1-D DGECSEL array under 500ns and 30-ns pumping

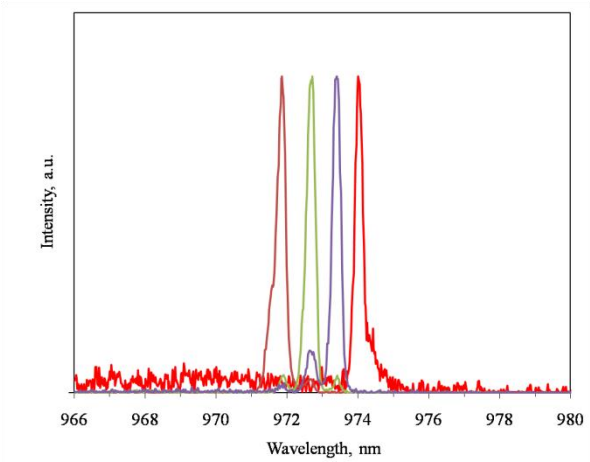

Figure 5:35 Multi-wavelength emission spectrum of external cavity GCSEL array at 30 ns, 1 kHz pulse at 50 A peak current amplitude

The 1-D DGECSEL array is also used as a fundamental source for blue light generation. Figure 5.36 shows the schematics of the experimental SHG setup. In this configuration the emission polarization direction is perpendicular to the crsytal axis, to rotate the polarization axis of the light to match with the nonlinear crystal poled axis a halfwave plate is placed after the DGECSEL array. Cylindrical bulk optics is used to

collimate each emitter. During the experiments we focused each emitter into its matching channel in 5% MgO:PPLN separately. The emitting wavelength from the individual GCSEL/DGR devices needs to be within the acceptance bandwidth of the corresponding PPLN channel at an optimum crystal tempareture for an efficient SH conversion process.

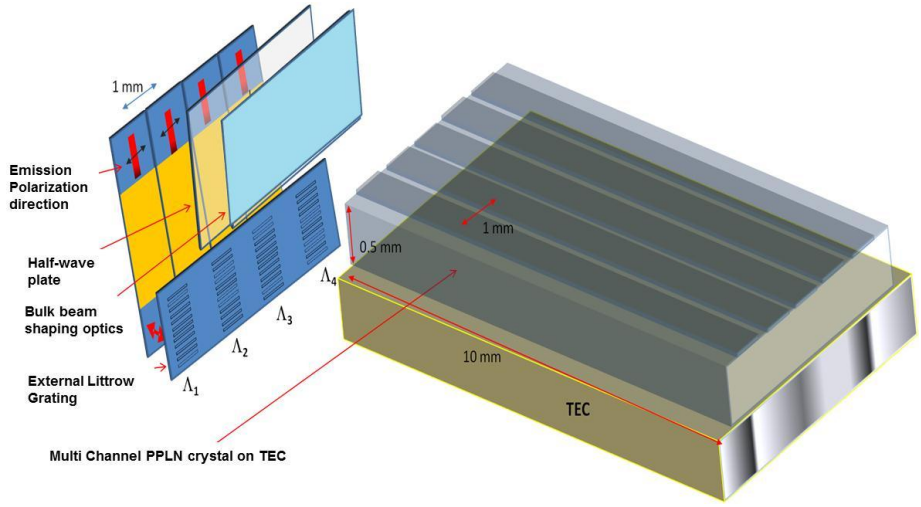

Figure 5:36 Schematics of the second harmonic generation setup using 1-D DGECSEL array and multi-channel PPLN crystal

The generated blue light and the fundamental light is separated using the same IR laser line filter which was used in the previous experimental setups.The SH spectra from each channel has bandwidth of ~ 0.15 nm at FWHM. The spectral measurements were taken at the optimum crystal temperature corresponding to maximum SH signal at the UV-power detector. Figure 5.37 shows the second harmonic spectra for each channel. The blue wavelengths are 485.86 nm, 486.23nm, 486.5, and 487.02 nm, which are half of the corresponding fundamental wavelengths, as expected.

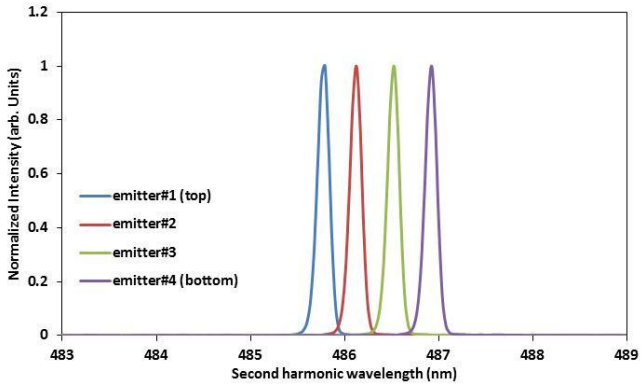

Figure 5:37 Second harmonic spectra of the 1-D Multi wavelength DGECSEL after the PPLN crystal

As stated earlier the output powers are not same from the individual emitters. Therefore the individual blue light output is measured from each channel and compared with the input fundamental peak power. Figure 5.38 shows the second harmonic peak power of a single channel vs. input fundamental peak power for that channel.

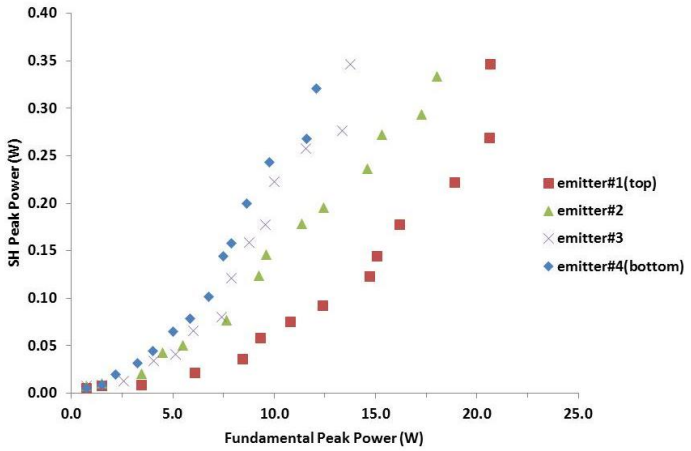

Figure 5:38 Second harmonic peak power vs fundamental peak power for each channel

Due to this fundamental peak power variation the correspond second harmonic peak power is slightly varying., This variation is smaller compared to the fundamental peak power variation, this is mainly due to the better matching of the fundamental wavelength to that channel period at a specific crystal temperature. The conversion

efficiencies are ~ 10^{-3} W^{-1} for each channel, producing ~0.3W -0.35W for each individual channel. Therefore the total generated second peak power 1.1 W. The whole system will then have a SH conversion efficiency of ~ 1010^{-3} W^{-1}.

5.8 Conclusion

We have presented the testing method used to evaluate the devices fabricated, along with the equipment used for each of the basic measurements. We then presented the results for each of the research goals undertaken.

First goal was to efficient external wavelength stabilization of the GCSEL device using an external dispersive optical element. We have used a one-dimensional grating structure operating under Littrow condition for this purpose. Single DGECSEL device yield a slope efficiency of ~ 0.8 W/A which is comparable to that of the integrated GCSEL/DGR approach. We than utilized this DGECSEL device as a fundamental source for blue light generation through SHG. The DGECSEL device was pumped at 20-ns pumping for the generation of high peak power second harmonic light. Nonlinear conversion efficiency of around ~10^{-3} W^{-1} were obtained with peak blue light power of around 0.6 W for an input power of around 32 W.

Secondly, a GCSEL/DGR type device is also fabricated and used as a fundamental source for blue light generation. This device also showed nonlinear conversion efficiency close to 10^{-3} $W^{-1,}$ with a SH peak power of around 0.66 W.

Thirdly, to increase the fundamental peak power, we have employed a master oscillator/power amplifier (MOPA) assembly. The expectation behind this experiment was to increase of the generated second harmonic peak power due to increased fundamental peak power. Although the output power is increased compared to the

corresponding applied current level, the PA output was highly multimoded and this caused the focused spot inside to crystal relatively large compared to the single laser devices. This increase spot size severely affected the conversion efficiency, and only nonlinear conversion efficiency around $2x10^{-2}$ W^{-1} is achieved.

Fourth goal was to implement the GCSEL/DGR concept into a vertically stacked 1-D multi-wavelength emitter array. This array is then used in the multi-wavelength blue light generation through SHG. We used a multigrating 5% magnesium–oxide-doped periodically poled lithium niobate (MgO : PPLN) crystal as the nonlinear conversion medium. In pulse operation, 0.6 W of multiwavelength total second-harmonic peak power was obtained. The individual emitter output is focused into each channel of the crystal by diffractive beam shaping optical element array to minimize the footprint area of the whole setup.

Another novel laser stacking approach is also investigated for fabricating 2-D GCSEL based laser. We employed our DGECSEL concept and stacked GCSEL bars with external silicon spacer with Littrow gratings on it. We demonstrated a multi-wavelength two-dimensional array based on vertically stacked grating coupled surface emitting laser bars. In pulse operation, lasing with a ~0.3nm-linewidth from each device and maximum total peak power of 120 W was achieved.

Lastly, we employed the DGECSEL concept for multi-wavelength blue light generation. 1-D multi wavelength DGECSEL array with total output peak power of 64 W was demonstrated. Each emitter is than focused into the corresponding channel of the nonlinear PPLN crystal, total of 1.1 W blue light is generated with an overall conversion efficiency of 10^{-3} W^{-1}.

CHAPTER 6: CONCLUSION

In this work we have presented a compact externally wavelength stabilized broad area GCSEL device. The wavelength of emission is stabilized with the combination of an external Littrow type grating and a grating out-coupler monolithically fabricated on the pi-side of the GCSEL device. The external Littrow grating is designed to maximize the reflected power back into the gain medium. The slope efficiencies of the fabricated external cavity GCSEL devices have comparable slope efficiencies to the monolithic GCSEL-DGR devices.

Furthermore we investigated the possibility of the external wavelength stabilization in one-dimensional and two-dimensional GCSEL array configurations. We have demonstrated the single-wavelength and multi-wavelength emission from these two configurations by changing the external Littrow grating period. The devices were operated under QCW and 30-ns pulse conditions. Total slope efficiencies of 0.89 W/A, and 1.8 W/A were experimentally demonstrated for 1-D and 2-D configurations respectively at 30 ns pumping conditions. The spectral characteristics of the devices were also measured. The individual emitters have 0.3 nm spectral linewidth at FWHM. The multi-wavelength 1-D external cavity array has four distinct emission peaks that are separated by 0.7 nm. A maximum peak power of ~64 W was observed for the 1D-emitter array at a peak current of 75 A.

The 2D array was driven to peak currents up to 68 A, limited by the 30-ns pulse-driver. Maximum peak-power of ~120W was measured from the array.Blue light sources are important in medical, undersea communication, and other areas of industrial applications as well as research. Blue light sources based on GaN are becoming more popular, but they are limited in power. Alternative approach is nonlinear conversion of near-IR sources to their second harmonic. Although solid-state lasers were used mostly, semiconductor near-IR sources are becoming quite popular with their smaller footprint area, and tenability range. We have employed our GCSEL based devices for blue light emission via second harmonic generation. We have used nonlinear crystals such as KTP, and LiNbO3 (LN) as the second harmonic conversion medium. These crystal were periodically poled for quasi-phase matched (QPM) type second harmonic generation. The advantage of the QPM over the perfect phase matching is that the polarization direction is same for all the interacting waves, the propagation direction is in one of the crystal axes, so this eliminates the spatial walk-off, and also the period of the poling can be designed for the crystal to be operated in the room temperature. We also designed a multi-channel PPLN crystal for multi-wavelength blue light emission using our arrayed GCSEL based devices.

We have demonstrated ~0.6×10^{-3} W^{-1} SHG conversion efficiency using PPKTP crystal. The maximum peak blue light power produced was 0.7 W for a fundamental peak power of 32 W. A GCSEL-DGR vertically stacked 1-D array with multi-wavelength emission is also employed as the fundamental source for blue light generation. The 1-D array has three distinct wavelengths, a beam shaping optics is designed and fabricated to collimate and focus the individual light from the emitters into the each channel of a

multi-channel of PPLN nonlinear crystal. The poling period each channel is matched for optimum conversion of the each emitter into its second harmonic. The beam shaping optics is designed as a diffractive micro-optics to reduce the footprint area of the SHG setup. 8-level diffractive cylindrical lens and a diffractive spherical lens array are fabricated.

The external Littrow grating that is integrated onto one of the GCSEL idea is a miniature external cavity. The SHG setup can be further miniaturized by fabricating a micro optical bench on a silicon wafer. The GCSEL light can be coupled into a planar waveguide which is fabricated on SOI via grating couplers. The only limitation in this setup is the nonlinear crystal length. The schematics of the proposed idea is shown in Figure 6.1

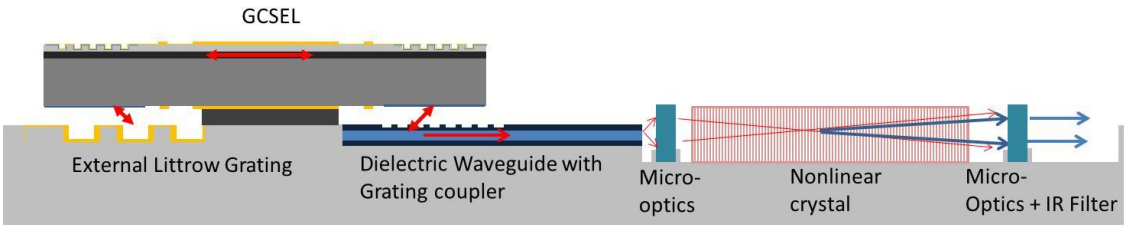

Figure 0-1Miniature SHG Setup on a silicon micro optical bench

Another possible improvement is the spectral quality of the emitted light. The external feedback grating can be modified to narrow the spectral linewidth of the emitted light from the GCSEL. The external grating can be fabricated on a substrate that is transparent at around 980 nm. Fused silica is one of the possible candidates. In this configuration two gratings are fabricated on the top side and the bottom side of the fused silica substrate. The top grating facing one of the GCSEL outputs will diffract only one

order into the silicon substrate, the bottom grating period and depth is set to operate under the TIR mode. This dual grating approach could possibly reduce the linewidth of emission. The performance of this approach needs a further theoretical and experimental investigation, which is not this part of the dissertation.

Beyond these perspectives, there are many application areas for the external cavity and monolithic semiconductor lasers. The external Littrow grating cavity can be applied to other surface emitting configurations. This external configuration offers wavelength selectivity and re-configurability, which can also be used applications such as spectral beam combining for making high power semiconductor light sources.

REFERENCES

[1] Hall, Robert N.; G. E. Fenner, J. D. Kingsley, T. J. Soltys, and R. O. Carlson "Coherent Light Emission From GaAs Junctions". Physical ReviewLetters 9 (9):366, 1962.

[2] Nathan, Marshall I.; Dumke, William P.; Burns, Gerald; Dill, Frederick H.; Lasher, Gordon ."Stimulated Emission of Radiation from GaAs p-n Junctions". Applied Physics Letters 1 (3): 62,1962

[3] Maiman, T.H. "Stimulated optical radiation in ruby".Nature 187 (4736): 493–494,1960

[4] Hayashi, I., M. B. Panish, and P. W. Foy, IEEE J. Quantum Electron. QE-5, 211, 1969

[5] Alferov, Zh. I. , V. M. Andreev, E. L. Portnoi, and M. K. Trukan, Sov. Phys. Semicond., 3, 1107, 1970.

[6] S.M. Sze, Physics of Semiconductor Devices, Ch 12, Wiley-Interscience, New York, 1981

[7] P. Bhattacharya, Semiconductor Optoelectronic Devices, Ch.1, Prentice Hall, Englewood Cliffs, NJ, 1994

[8] Larry A. Coldren, Scott W. Corzine, Diode Lasers and Photonic Integrated Circuits, Wiley Series in Microwave and Optical Engineering, Kai Chang Editor, 1995

[9] Govind P. Agrawal, Niloy K. Dutta, Semiconductor Lasers, 2nd edition, 1993

[10] Govind P. Agrawal, Longitudinal mode stabilization in semiconductor lasers with wavelength selective feedbach, J. Appl. Phys., 59, 3958, 1986

[11] Joseph T. Verdeyen, Laser Electronics,3rd Edition, Prentice Hall, 1995

[12] T. Numai, “Fundamentals of Semiconductor Lasers,” Springer Series on Optical Sciences, Dec. 2010

[13] Casey, H. C, Jr., S. Somekh, and M. ilegems, Appl. Phys. Lett., 27, 142, 1975

[14] Reinhart, F. K. R. A. Logan, and C. V. Shank, Appl. Phys. Lett, 27, 45, 1975

[15] Utaka K., K. Kobayashi, K. Kishino, and Y. Suematsu, Electron.. Lett.,16, 455, 1980

[16] Jewell, Jack L.; Lee, Y. H.; Harbison, J. P.; Scherer, A.; Florez, L. T. EEE Journal of Quantum Electronics (ISSN 0018-9197), vol. 27, June 1991, p. 1332-1346

[17] ChangHasnain, Connie J.; Harbison, J. P.; von Lehmen, Ann C.; Florez, L. T.; St offel, N. G.; Hasnain, GhulamIEEE Journal of Quantum Electronics (ISSN 0018-9197), vol. 27, June 1991, p. 1402-1409

[18] Evans, G.A. et al, Appl. Phys. Lett., 49(6), 314-315,1986

[19] Stoll, H. M. SPIE Proceedings **139**, 1978

[20] Waarts, R. Welch, D. F. et al, Electron. Lett., 26, 129,1990

[21] Hagberg M., Eriksson N., and Larsson A., "High efficiency surface emitting lasers using blazed grating outcouplers," *Applied Physics Letters*, vol. 67, pp. 3685-3687, 1995

[22] Eriksson N., Hagberg M., and Larsson A., "Highly Efficient Grating-Coupled Surface-Emitters with Single Outcoupling Elements," *IEEE Photonics Technology Letters*, vol. 7, pp. 1394-1396, 1995.

[23] Evans G. M. and Hammer J. M., *Survace Emitting Semiconductor Lasers and Arrays*, (AcademicPress,Inc.,1993)SanDiego,CA,Ch.4,5.

[24] J. K. O'Daniel, O. V. Smolski, M. G. Moharam, E. G. Johnson, "Integrated wavelength stabilization of in-plane semiconductor lasers by use of a dual-grating reflector", Opt. Lett., , Vol. 31, No. 2, p. 211-213. 2006

[25] T. Ikegami, et. al. "Frequency Stabilization of Semiconductor Laser Diodes," Artech House Optoelectronics Library, March 1995

[26] S. R. Karlsen, R. Kirk Price, M. Reynolds, A. Brown, R. Mehl, S. Patterson, and R. J. Martinsenand, "100-W, 105-μm, 0.15NA Fiber Coupled Laser Diode Module," Proc. SPIE 7198, 71980T, 2009.

[27] W. Hu, F. D. Patel, M. L. Osowski, R. M. Lammert, S. W. Oh, C. Panja, V. C. Elarde, L. Vaissie, and J. E. Ungar, "Hihg-spectral brightness pump sources for diode-pumped solid state lasers," Proc. SPIE 7198, 71981R, 2009

[28] J.F. Seurin, C. L. Ghosh, V. Kalfin, A. Miglo, G. Xu, J. D. Wynn, P. Pradhan, and L. A. D'Asaro , "High-power high-efficiency 2D VCSEL arrays," Proc. SPIE 6908, 690808, 2008.

[29] G. A. Evans, J. M. Hammer, "Surface Emitting Semiconductor Lasers and Arrays," Academic Press, 1993

[30] J. K. O'Daniel, O. V. Smolski, M. G. Moharam, E. G. Johnson, "Integrated wavelength stabilization of in-plane semiconductor lasers by use of a dual-grating reflector", Opt. Lett., , Vol. 31, No. 2, p. 211-213. 2006

[31] Y. O. Yilmaz, O. V. Smolski, V. O. Smolski, E. G. Johnson, "Multi-Wavelength Blue Light Source based on MgO: PPLN SHG using Vertically Stacked Grating Coupled Surface Emitting Lasers," IEEE Photon. Tech. Lett., accepted for publication

[32] R. Beach, W.J. Benett, B.L. Freitas, D. Mundinger, B.J. Comaskey, R.W Solarz, and M.A. Emanuel, "Modular microchannel cooled heatsinks for high average power laser diode arrays", IEEE J. of Quant. Electron., , Vol. 28, No. 4, p. 966-976, 1992

[33] L. Vaissié, O. Smolski, E. Johnson "Crossed-beam superluminescent diode", Opt. Lett., , Vol. 30, No. 13, p. 1608-1610, 2005

[34] F. Laermer and A. Schilp, Method of anisotropically etching silicon. 1996, US Patent 5,501,893

[35] Robert W. Boyd, Nonlinear Optics: Third Edition. ,Academic Press / Elsevier, Inc. Oxford, UK, 2008

[36] M. M. Fejer, G. A. Magel, D. H. Jundt, and R. L. Byer, "Quasi-phasematched second harmonic generation: Tuning and tolerances," IEEE J.Quantum Electron., vol. 28, no. 11, pp. 2631–2654, Nov. 1997

[37] R. L. Byer, "Quasi-Phasematched nonlinear interactions and devices," Journal of Nonlinear Optical Physics and Materials, Vol.6, pp.549-592, 1997

[38] W. P. Risk, T. R. Gosnell, and A.V. Nurmiko, "Compact Blue-Green Lasers," Camridge Studies in Modern Optics, 2003

[39] A. Jechow, M. Schedel, S. Stry, J. Sacher, and R. Menzel, "Highly effi-cient single-pass frequency doubling of a continuous-wave distributedfeedback laser diode using a PPLN waveguide crystal at 488 nm," Opt.Lett., vol. 32, no. 20, pp. 3035–3037, 2007.

[40] A. Jechow and R. Menzel, "Efficient blue light generation by frequencydoubling of a broad-area diode laser in a compact external cavity," Appl.Phys. B, vol. 89, no. 4, pp. 507–511, 200

[41] O. Gayer, Z. Sacks, E. Galun, and A. Arie, "Temperature and wavelength dependent refractive index equations for MgO-doped congruentand stoichiometric LiNbO ," Appl. Phys. B, vol. 91, pp. 343–348, 2005

[42] J. Goodman,"Introduction to Fourier Optics"(3rd ed,). Roberts & Co Publishers,2005

[43] D. C. O'Shea, T. J. Suleski et. al. " Diffractive Optics: Design, Fabrication, and Test." SPIE Tutorial Texts in Optical Engineering, vol. TT62, 2003

[44] R. Fischer, "Optical System Design," 2nd Edition, McGraw-Hill, 2008

[45] M. K. Poutous and et. al. : Polarization selective,graded-reflectivity resonance filter,using a space-varying guided –mode resonance structure," Opt. Express, vol.18, p. 27764, Jan. 2010

[46] M.J. Madou, "Fundamentals of Microfabrication," CRC-Press, 1st edition, 1998

[47] F. Laermer and A. Schilp, "Method of Anisotropically Etching Silicon," US Patent 5,501,893, 1996

[48] M. Elwenspoek, H. V. Jansen, "Silicon micromachining," Cambridge University Press, August 2004

[49] M. Pitchumani, H. Hockel, W. Mohammed, and E. Johnson, "Additive lithography for fabrication of diffractive optics," Appl. Opt. 41, 6176-6181 (2002).

[50] M. Pitchumani, H. Hockel, J. Brown, W.S. Mohammed, and E. G. Johnson, "Additive lithography for refractive micro-optics," Proc. SPIE 4984, 1 (2003),

[51] G. J. Swanson, ''Binary optics technology: the theory and design of multilevel diffractive optical elements,'' MIT Lincoln Laboratory Rep. 854 1MIT, Cambridge, Mass., 1989

[52] M. Pitchumani, "Additive lithography: Fabrication and intergration of micro optics," Ph.D. Dissertation, University of Central Florida, 2006

[53] Y. O.Yilmaz, O. V. Smolski, P. Srinivasan, V. O. Smolski and E. G. Johnson, "Blue light source based on spectrally stabilized external dual grating reflector coupled surface emitter array," Proc. SPIE, Vol. 7919, p.79190C, Feb. 2011

[54] O. V. Smolski, Yilmaz. Y.O., V.O. Smolski, E. G. Johnson, "Blue Light source based on a PPKTP SHG using a Grating Coupled Laser Diode," IEEE Photon. Tech. Lett., vol. 21, pp.1420-1422, 2009

[55] O. V. Smolski, Yilmaz. Y.O., V.O. Smolski, E. G. Johnson," Compact blue light sources based on grating coupled surface emitting lasers," Proc. SPIE, vol. 7193, Feb. 2009

[56] Y. O.Yilmaz, O. V. Smolski, V. O. Smolski and E. G. Johnson, "Multiwavelength Blue Light Source Based on MgO:PPLN SHG using vertically stacked grating-coupled surface emitting lasers," IEEE Photon. Tec. Lett., vol. 22, pp. 1711-1713, 2010

[57] Y. O.Yilmaz, O. V. Smolski, V. O. Smolski and E. G. Johnson, "2-D Staced External Cavity Multiwavelength Surface Emitting Laser Array," IEEE Photon. Tec. Lett., vol. 23, pp. 323-325, 2011

[58] R. Rumpf, "Design and optimization of nano-optical elements by coupling fabrication to optical behavior," Ph.D. Dissertation, University of Central Florida, 2006

[59] D. M. Sullivan, "Electromagnetic Simulation using the FDTD Method," Wiley-IEEE Press, 1st edition, July 2000

APPENDIX A: FINITE-DIFFERENCE-FREQUENCY-DOMAIN METHOD

In this section an overview of the finite-difference-frequency-domain (FDFD) numerical method that is utilized to calculate the diffraction efficiency of the external Littrow gratings is explained. A detailed of this method can be found in [58]

FDFD is a fully vectorial numerical method and obtains rigorous solution to Maxwell's equations [59]. The Maxwell equations are solved in the frequency domain; this is advantageous compared to time domain methods in calculating and resolving sharp resonances. Also material dispersion and oblique field incidence can easily be incorporated.

Maxwell Equations are solved in frequency domain and transformed into set of linear algebraic equations using finite difference methods. Finite difference methods are used in numerical modeling to fit the continuous functions into a grid. The derivatives at

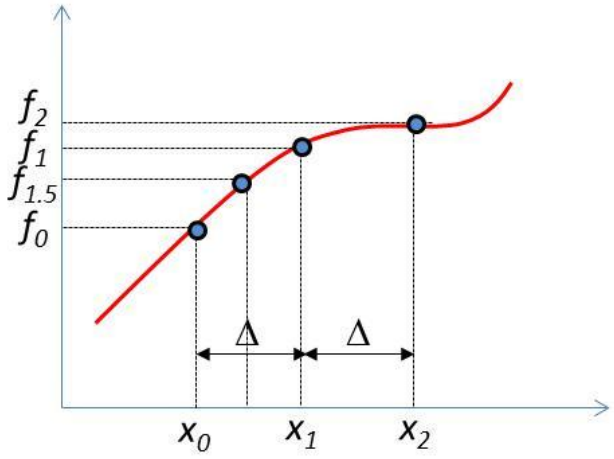

Figure 9:1 Schematics showing the finite difference approximation on a function

points are approximated by the neighboring points and the function values. The derivative at point 1 is approximated as $\frac{\partial f1}{\partial x} \cong \frac{f2-f0}{2\Delta}$ and the mid-points are approximated as $\frac{\partial f1.5}{\partial x} \cong \frac{f2-f1}{\Delta}$ (see Figure 9:1).

The electric and magnetic fields are interleaved on grid for this numerical model. The most popular and efficient grid scheme is Yee grid model. In Yee grid, all electric and magnetic field components are interleaved on a Cartesian grid. Figure 9:2 shows a 2D Yee grid.

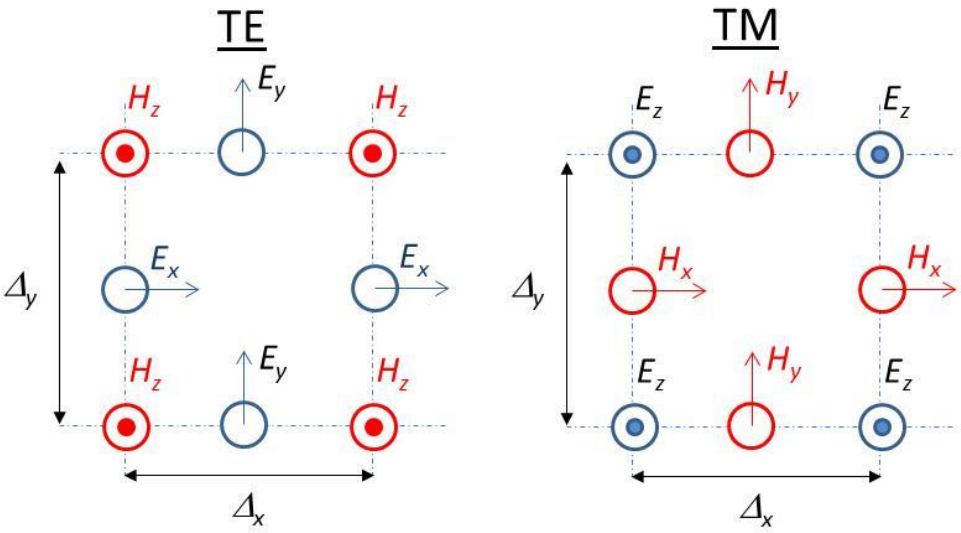

Figure 9:2 2D Yee grid for TE and TM solutions of Maxwell Equations

The incorporation of the all these parameters into numerical is shown in Figure 9:3. The finite difference approximation of the wave equation , incorporating the perfectly matched layer boundary condition, including the source, and calculating the reflected/transmitted diffracted orders are summarized in this flow chart.The source code for the FDFD algorithm was written by Dr. Raymond Rumpf, alumni of the

Microphotonics Laboratory. A detailed explanation of the can be found in his dissertation [58].

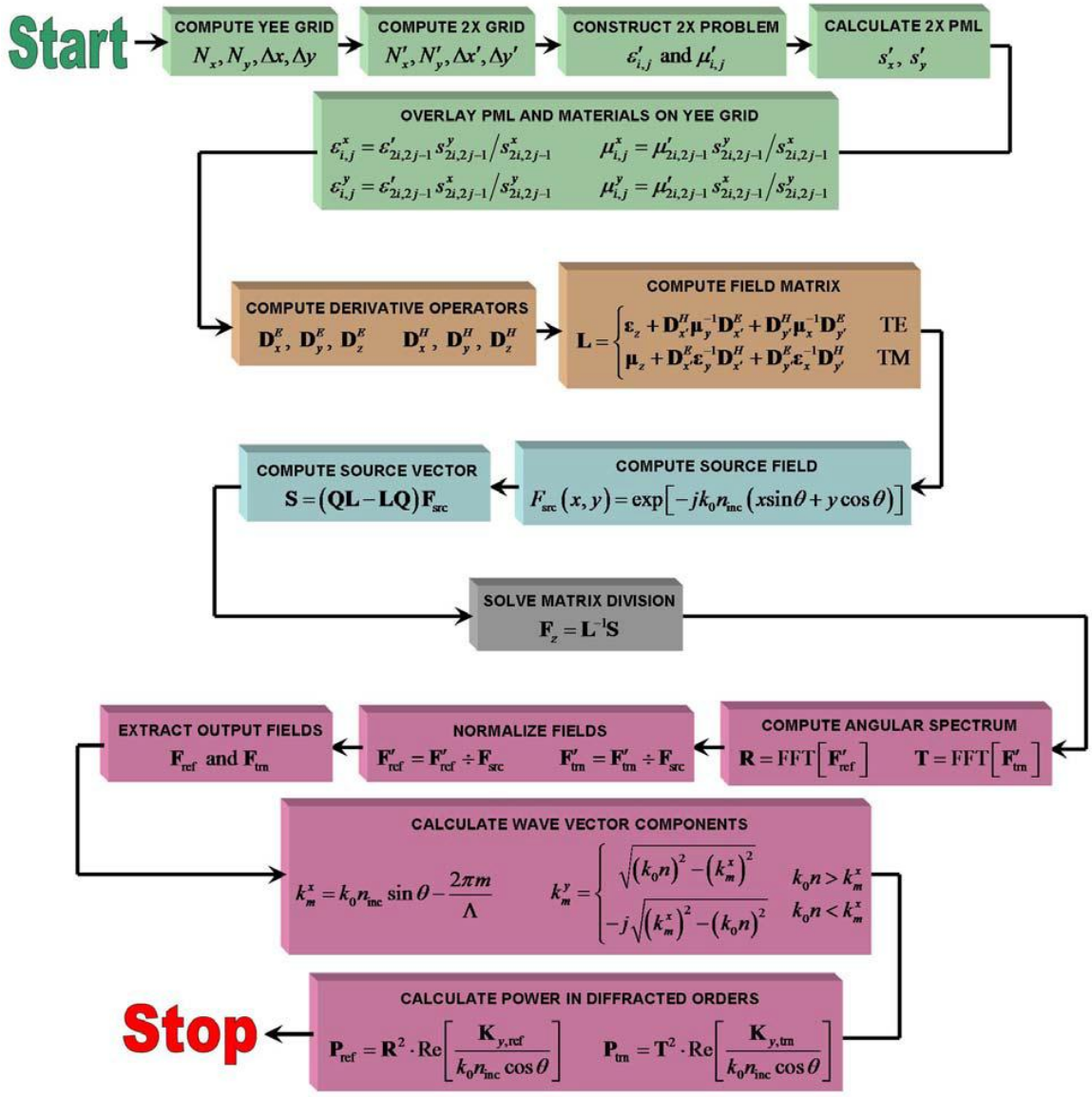

Figure 9:3 Flow chart fort he FDFD algorithm [58]

APPENDIX B: FABRICATION OF PERIODICALLY POLED NONLINEAR CRYSTALS

Second order nonlinear processes involve the mixing of three electromagnetic waves. The magnitude of the nonlinear response of the crystal is characterized by the $\chi^{(2)}$ coefficient, as explained in the introduction chapter of this dissertation. Second harmonic generation is the most common application that utilizes the $\chi^{(2)}$ properties of a nonlinear crystal.

In SHG, it is necessary for the phase relation between the input and the generated photons to be constant throughout the crystal for efficient nonlinear conversion of the fundamental photons. Traditional phase matching requires that the input and the generated photon is propagated through the crystal in a direction where they experience the same refractive index. This method has some limitations [32], to overcome these limitations an alternative and popular method is the quasi-phase matched method, the details of this technique is explained in the first chapter. For QPM, the nonlinear crystal polarization needs to be inverted periodically (see Figure 10:1)

Nonlinear crystals are ferroelectric crystals. Ferroelectric crystals' each unit cell has a small electric dipole moment. The orientation of the electric dipole in a unit cell depends on the positions of the ions in that unit cell. An intense electric field has the ability to invert the direction of the dipole moment of the unit cell. This electric field is usually very high (~ 10^5 V/cm). The intense electric field is applied only for a few milliseconds. After this the inverted sections of the crystals are permanently imprinted on thecrystalstructure.

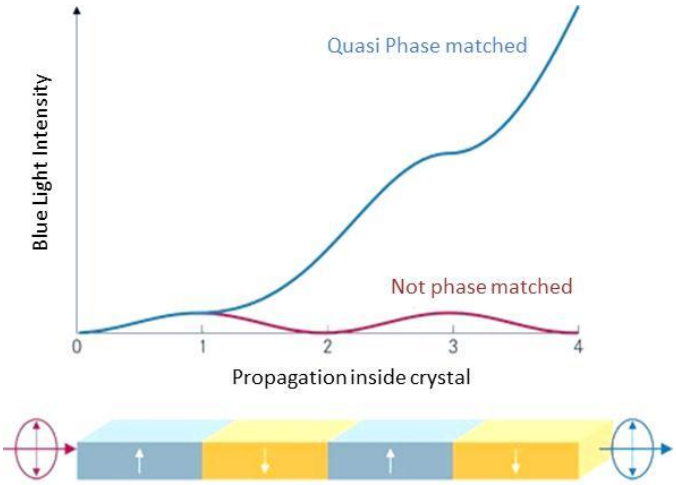

Figure 10:1 The converted intensity along the propagation direction of the periodically poled crsytal.

QPM requires this inversion to be periodic through the propagation direction of the nonlinear crystal. The periodic poling on the nonlinear crystal is produced by depositing electrodes on the crystal.

Figure 10.2 shows the steps of periodic poling of a nonlinear crystal. After photoresist is spun on the ferroelectric crystal wafer (or piece of the wafer), UV light is applied to transfer the mask pattern into the photoresist. Next step is to develop the photoresist, after this step appropriate metal layer is deposited on both surfaces of the crystal. A high voltage is applied between the electrodes to invert the polarization. The areas below the photoresist patterns are not affected, since the photoresist acts as an insulating barrier. After high voltage is application the metal layers and the photoresist is removed. During this inversion process the design of the electrodes and the control of the applied high voltage is extremely input to for the desired shape of the poled region for

optimum performance of the crystal. The imperfections in the poling process severely affect the efficiency of the nonlinear conversion process.

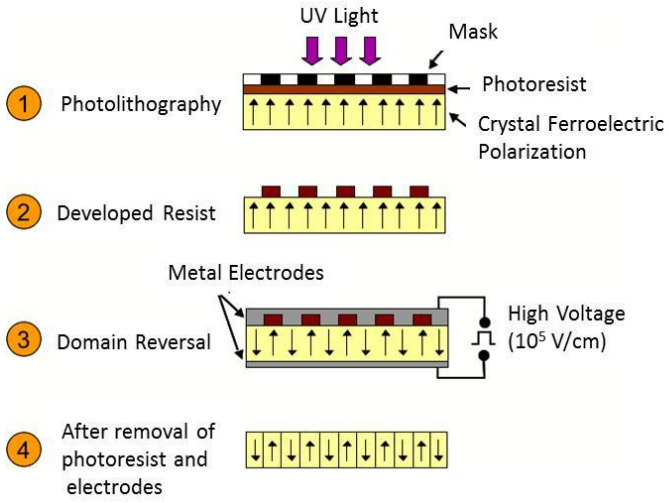

Figure 10:2 Steps of the periodic poling of a ferroe electric nonlinear crystal

APPENDIX C: PROJECTION LITHOGRAPHY

The projection lithography tool is the fundamental tool used in the CMOS technology for mass producing integrated circuits. This technology is also widely used for making micro and nano optical structures on different substrate materials.

In projection printing a mask pattern is imaged onto a photoresist coated wafer. The mask and the wafer do not contact, compared to contact lithography, thus keeping the process clean with no wafer or mask damage. The resolution of the stepper technology increased with need of increasing number of IC inside a small size. The early steppers have resolutions around 0.8μm-1μm, now this number is ~40nm and even smaller. The resolution (or the smallest feature size) of a stepper is mainly determined by the wavelength of the source, the coherence of the source, NA of the optical system. There are other factors that determine the resolution of a stepper system, but the listed ones can be considered as the most critical parameters. In general the resolution of the projection system is $R = k_1\lambda/NA$, and depth of focus is $DOF = k_2\lambda/NA^2$, where k1 and k2 are the characteristic constants of the specific lithographic process which depend on the photoresist, process parameters, type of the mask, the pattern on the mask, aberration of the optical system, the coherence and etc.

The projection system consists of an illumination system, a lithographic imaging lens assembly, a mask (reticle) alignment system, and a very precise wafer positioning system (see Figure 11:1). Usually a reduction factor of 4X, 5X, and 10X is used to reduce the image of the mask onto the substrate. This reduction has several advantages such as easier and cheaper mask fabrication due to the increased mask features, and more error

forgiving on mask imperfections, since the imperfection is also reduced at the image plane.

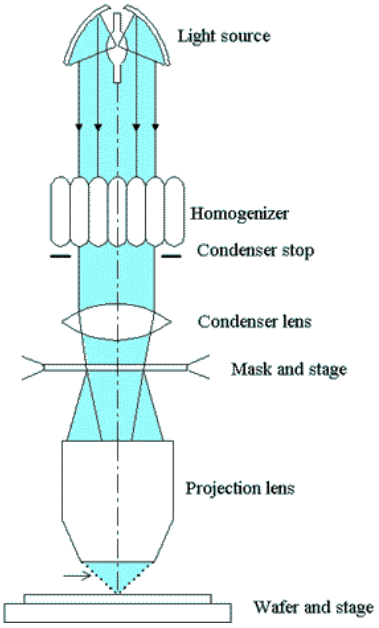

Figure 11:1 Basic components of a projection lithography (stepper) system

Another important part of the stepper system is the wafer positioning stage. The accuracy of these stages is usually ~50nm or less. There is additional control features called reticle management system (RMS) windows on the mask to ensure the repeatability and the alignment accuracy. The wafer is shifted after each exposure to the next die position and the exposure can be performed again.

Figure shows the stepper system used during this dissertation to make micro optical structures. The system is a GCA 6300-C G-line stepper. The light from the source assembly is filtered to transmit only the G-line (436nm) and then homogenized and collimated to cover an area larger than 100mm X 100mm. The GCA has four blades before the mask (reticle) which allows the user to select the regions to exposure.

Figure 11:2 GCA6300-C G-line (436nm) stepper control unit and the stepper system.

This allows placing multiple patterns on the same reticle and each pattern can be separately exposed with different exposure times. This feature is extremely useful during additive lithography. The NA of this system is ~0.35 and the resolution is 0.8-1.1 um.